THEORETICAL DESCRIPTION OF ELECTRONIC EXCITATIONS IN EXTENDED SYSTEMS: BEYOND THE STATIC MATERIAL MODEL

Alex Domingo Toro

Dipòsit Legal: T. 1705-2011

UNIVERSITAT ROVIRA I VIRGILI
THEORETICAL DESCRIPTION OF ELECTRONIC EXCITATIONS IN EXTENDED SYSTEMS:
BEYOND THE STATIC MATERIAL MODEL
Alex Domingo Toro
DL:T. 1705-2011

Theoretical description of electronic excitations in extended systems: beyond the static material model

Alex Domingo Toro

PhD Thesis

Universitat Rovira i Virgili

UNIVERSITAT ROVIRA I VIRGILI
THEORETICAL DESCRIPTION OF ELECTRONIC EXCITATIONS IN EXTENDED SYSTEMS:
BEYOND THE STATIC MATERIAL MODEL
Alex Domingo Toro
DL:T. 1705-2011

UNIVERSITAT ROVIRA I VIRGILI
THEORETICAL DESCRIPTION OF ELECTRONIC EXCITATIONS IN EXTENDED SYSTEMS:
BEYOND THE STATIC MATERIAL MODEL
Alex Domingo Toro
DL:T. 1705-2011

Alex Domingo Toro

Theoretical description of electronic excitations in extended systems: beyond the static material model

PhD Thesis

Supervised by Prof. Coen de Graaf

Department of Physical and Inorganic Chemistry
Quantum Chemistry Group

Universitat Rovira i Virgili

Tarragona
2011

UNIVERSITAT ROVIRA I VIRGILI
THEORETICAL DESCRIPTION OF ELECTRONIC EXCITATIONS IN EXTENDED SYSTEMS:
BEYOND THE STATIC MATERIAL MODEL
Alex Domingo Toro
DL:T. 1705-2011

UNIVERSITAT ROVIRA I VIRGILI
THEORETICAL DESCRIPTION OF ELECTRONIC EXCITATIONS IN EXTENDED SYSTEMS:
BEYOND THE STATIC MATERIAL MODEL
Alex Domingo Toro
DL:T. 1705-2011

Departament de Química Física i Inorgànica

Coen de Graaf, investigador ICREA, del Departament de Química Física i Inorgànica de la Universitat Rovira i Virgili,

Faig constar que la present memòria, titulada:

"Theoretical description of electronic excitations in extended systems: beyond the static material model"

ha estat realitzada sota la meva direcció al Departament de Química Física i Inorgànica de la Universitat Rovira i Virgili per Alex Domingo Toro per a l'obtenció del títol de Doctor i que acompleix els requeriments per poder optar a Menció Europea.

Tarragona, 22 de Septembre de 2011

El director de la tesi doctoral

Coen de Graaf

UNIVERSITAT ROVIRA I VIRGILI
THEORETICAL DESCRIPTION OF ELECTRONIC EXCITATIONS IN EXTENDED SYSTEMS:
BEYOND THE STATIC MATERIAL MODEL
Alex Domingo Toro
DL:T. 1705-2011

UNIVERSITAT ROVIRA I VIRGILI
THEORETICAL DESCRIPTION OF ELECTRONIC EXCITATIONS IN EXTENDED SYSTEMS:
BEYOND THE STATIC MATERIAL MODEL
Alex Domingo Toro
DL:T. 1705-2011

Agraïments

El present projecte no s'hagués pogut desenvolupar sense l'ajut i completa dedicació del director de la tesi doctoral, el professor Coen de Graaf. Vull agrair-li el seu esforç i amabilitat al llarg de tots aquests anys, en els que sempre m'ha ofert reflexions i comentaris constructius tan si s'obtenien bons o no tan bons progressos. També vull donar les gràcies per haver tingut cura de mi i per les llargues discussions als professors Ria Broer de la Rijksuniversiteit Groningen i Vincent Robert de la Université de Strasbourg, els quals foren els meus supervisors en les estades que vaig realitzar a Holanda i França, respectivament, en el transcurs d'aquest treball. L'aprenentatge realitzat sobre diversos mètodes computacionals no hagués estat possible sense la col·laboració de l'Antoni Rodríguez-Fortea de la Universitat Rovira i Virgili i del Marcel Swart de la Universitat de Girona, qui m'han ensenyat a entendre i treballar amb aquests mètodes. No vull oblidar tampoc el paper del professor Francesc Illas de la Universitat de Barcelona el qual em va iniciar en el món de la recerca i va ser clau en decidir-me a realitzar aquest doctorat.

Vull recordar a la gent del Grup de Química Quàntica del Departament de Química Física i Inorgànica per tots aquests bons anys passats a Tarragona. Els companys de màster, la Zahra i la Sonia, amb qui he coincidit més temps. La Mireia i el Yannick, que em van ajudar molt al començament quan estava més perdut. El John i el Rémi amb qui hem compartit uns quants Jujols i varies cerveses. El Xavi i el Ramón qui m'han ofert casa per poder pernoctar a Tarragona. A la Maria Àngels amb qui he compartit docència i congressos. El Jose qui ha mantingut el cluster en peu i funcionant. I a tota la resta amb qui he tingut molt bons moments. Gràcies a tots.

Per últim i no menys important, vull agraïr a mon pare i ma mare el haver estat sempre al meu costat, en les bones èpoques i les menys bones, pacientment i deixant-me tenir veu. No m'oblido de l'Esther, ma germana, amb qui sempre he pogut comptar. I acabo amb l'Agnès, la meva parella, qui és la raó per la que he fet dos-cents quilometres diaris i qui m'ha recolzat tots aquests anys animant-me a seguir endavant.

UNIVERSITAT ROVIRA I VIRGILI
THEORETICAL DESCRIPTION OF ELECTRONIC EXCITATIONS IN EXTENDED SYSTEMS:
BEYOND THE STATIC MATERIAL MODEL
Alex Domingo Toro
DL:T. 1705-2011

UNIVERSITAT ROVIRA I VIRGILI
THEORETICAL DESCRIPTION OF ELECTRONIC EXCITATIONS IN EXTENDED SYSTEMS:
BEYOND THE STATIC MATERIAL MODEL
Alex Domingo Toro
DL:T. 1705-2011

"Light and matter are both single entities, and the apparent duality arises in the limitations of our language."

— Werner Karl Heisenberg

UNIVERSITAT ROVIRA I VIRGILI
THEORETICAL DESCRIPTION OF ELECTRONIC EXCITATIONS IN EXTENDED SYSTEMS:
BEYOND THE STATIC MATERIAL MODEL
Alex Domingo Toro
DL:T. 1705-2011

UNIVERSITAT ROVIRA I VIRGILI
THEORETICAL DESCRIPTION OF ELECTRONIC EXCITATIONS IN EXTENDED SYSTEMS:
BEYOND THE STATIC MATERIAL MODEL
Alex Domingo Toro
DL:T. 1705-2011

Contents

UNIVERSITAT ROVIRA I VIRGILI
THEORETICAL DESCRIPTION OF ELECTRONIC EXCITATIONS IN EXTENDED SYSTEMS:
BEYOND THE STATIC MATERIAL MODEL
Alex Domingo Toro
DL:T. 1705-2011

CHAPTER 1

Introduction

Materials with tunable magnetic and electric properties have been the subject of many research efforts during the last decades. A system capable of persistently changing its magnetic or electric properties upon some external stimulation has many potential technological applications, for example to make nano-switches or as memory devices. Nowadays, there are several molecular materials known to behave as bistable systems, which are molecular structures that have at least two accessible and stable electronic states with differentiate electronic characteristics. One of those states is the fundamental state of the material and the other one is some metastable excited state. The external stimulation that triggers the switch between those states can be a change in temperature, in pressure or by light radiation. The population of the metastable state is (quasi-)permanent and, in some cases, reversible. From the applicability point of view, the method that offers better control on the process is the light induced excitation.

Prussian blue ($Fe_4^{3+}[Fe^{2+}(CN)_6]_3$) and its analogues are a good example of this kind of materials. The basic structure of these crystalline materials is a cubic lattice structure formed by Fe–CN–M (M=Fe,Co,Mn) sequences with interstitial K^+ ions. The FeCo Prussian blue analogue shows a clear variation of its molar magnetic susceptibility (χ_m) on temperature (T) change. At room temperature the material is found on a ferrimagnetic state, formed by a Fe^{3+} metal atom on its low-spin state (LS) ($t_{2g}^5 e_g^0$) and a Co^{2+} on its high-spin state (HS) ($t_{2g}^5 e_g^2$), configuration which confers a magnetic moment to the material. On cooling, at $T_{1/2} \downarrow = 180$ K where $T_{1/2}$ represents the temperature at which half population is on the high-temperature state and the other half on the low temperature state, there is an abrupt lowering of $\chi_m T$ that reflects the jump to the diamagnetic state. Hence, the total spin of the system becomes $S = 0$ because the electronic configuration of the metal atoms changes to Fe_{LS}^{2+} ($t_{2g}^6 e_g^0$) and Co_{LS}^{3+} ($t_{2g}^6 e_g^0$). The crystalline material can remain stable on this state and the process is reversible by heating back to room temperature. However, the switch to the magnetic state is now produced at $T_{1/2} \uparrow = 220$ K. This large hysteresis loop of 40 K of amplitude demonstrates that there are strong cooperative interactions conditioning this phenomenon. Furthermore, FeCo Prussian blue also undergoes a photoinduced interconversion from diamagnetism to ferrimagnetism. By irra-

diating this coordination compound with light of ~ 550 nm wavelength at 5 K its magnetization increases significantly. The radiation triggers a metal-to-metal charge transfer (MMCT) from Fe^{2+}_{LS} to Co^{3+}_{HS}, producing the next reaction:

$$Fe^{2+}_{\mathrm{LS}}(t^6_{2g}e^0_g) - \mathrm{CN} - Co^{3+}_{\mathrm{LS}}(t^6_{2g}e^0_g) \longrightarrow Fe^{3+}_{\mathrm{LS}}(t^5_{2g}e^0_g) - \mathrm{CN} - Co^{2+}_{\mathrm{HS}}(t^5_{2g}e^2_g)$$

This reaction path is supposed to go through an intermediate specie in the form of $Fe^{3+}_{\mathrm{LS}}(t^5_{2g}e^0_g) - \mathrm{CN} - Co^{2+}_{\mathrm{LS}}(t^6_{2g}e^1_g)$ before relaxing back to the final product. The increase of magnetization can persist at 5 K for several hours after the radiation is stopped. Additionally, the photoinduced magnetization on the compound exhibits an hysteresis loop on magnetic field change, proving to have turned into a magnetic material. Moreover, this compound also shows a similar variation on conductance by modifying the electric field or the temperature. Therefore, these phenomena turn this material into a possible multifunctional system with tunable magnetic and electric properties determined by external factors. [1, 2]

Coordination complexes of Fe^{2+} can exhibit bistability between a LS state and a HS state in the so-called Spin Crossover phenomenon (SCO). The Fe^{2+} is a d^6 metal that hexa-coordinates on a pseudo-octahedral environment. The fundamental state of these compounds is a diamagnetic ${}^1A_{1g}$ LS state, which is characterized by a $(t^6_{2g}e^0_g)$ electronic configuration for the metal atom. On the other hand, the HS is a paramagnetic ${}^5T_{2g}$ state that presents a Fe^{2+} with a $(t^4_{2g}e^2_g)$ electronic configuration. The most significant effect of this process is the elongation of the metal–ligand bonds in the LS→HS transition, which favours the HS state stability. Since there is no variation on the metal formal charge, the difference in energy between these two states is mainly determined by the ligand field. Thus, the LS–HS energetic difference can become of the order of k_BT by choosing an appropriate ligand. Under these conditions, a rise of temperature or a variation of pressure can trigger a direct LS→HS transition, depending on the relative energy between the LS and HS states. [3]

Nevertheless, compared to the thermal or pressure induced SCO, a more powerful technique is the so-called Light Induced Excited State Spin Trapping

(LIESST), which consists on triggering the LS→HS transition by light radiation. The photon absorption excites the LS state to a higher singlet excited state that rapidly decays through various internal conversions and inter-system crossings to the quintet HS state. This process is very fast, of the order of few ps or less, and leads to quantum efficiencies of nearly 100%. The trapping on the HS state depends on the incapacity of the system to thermally relax back to the LS state, which is accomplished by producing the LIESST at lower temperatures than the spin conversion temperature and by coordinating the Fe^{2+} atom to specific ligands, that result in complexes with large degrees of distortion upon the LS→HS transition. Moreover, it is possible to perform a reverse-LIESST by irradiating the compound on the HS state, which is excited to a higher quintet state and relaxes back to the singlet LS fundamental state. [4]

The described phenomena on those different compounds are a tiny sample of the known bistable systems. However, those two examples clearly show the complexity of these systems, which is mainly related to the interplay of many diverse properties. Nowadays, a main challenge of the research on those materials is to design a compound capable to behave as a bistable system under normal conditions, through the aforementioned photoinduced magnetization or LIESST. That achievement is key for further technological developments based on such systems. Therefore, the understanding of the factors that determine their bistability is equally important to be able to design the future compounds. For this purpose, the theoretical and computational methods become a valuable tool to unveil the underlying mechanisms of these phenomena.

Since the photoinduced process is usually localized on few atoms, it turns very convenient to use local models that only cover the localized electronic transition. Those systems work on a piece of the whole crystalline material, the so-called cluster, or on single molecules. Typically, there are less than a hundred atoms forming the theoretical model and, therefore, it is possible to use sophisticated wave function based methods to describe their electronic structure with an all-electron treatment of electronic correlation effects. Unfortunately, the complexity is high. The presented hysteresis behaviour of the FeCo Prussian blue analogue reflects the definite role of cooperative effects in those systems, which

can also involve a phase transition, like in the FeMn Prussian blue [5]. On the other hand, the decay path of the LIESST process involves many excited states and could depend on some specific vibrational modes [6, 7]. Furthermore, there is a similar process to LIESST that causes photoinduced valence tautomerism on some Co complexes [8]. All these effects cannot be properly described by traditional theoretical approaches based on static material models.

It turns necessary to work with dynamical models that incorporate into the theoretical description the macroscopic concept of temperature and the vibro-rotational degrees of freedom. Hence, it will be possible to explore the vibrational modes and conformational space of the compounds under conditions that better reproduce the experimental set up. Additionally, the theoretical model should include a reactive environment model to describe the changes that cause the photoinduced transition not only to the directly involved atoms, but also to their surroundings. This capability is necessary to study the hysteresis behaviour of these materials taking into account the solvent effects on coordination compounds and cooperative effects on crystalline systems.

Therefore, the aim of the present work is to develop an *ab initio* theoretical procedure, that fulfils the aforementioned requirements to obtain a richer and more accurate description of the electronic structure of bistable materials. Our project consists in combining various well known theoretical methods that complement themselves, giving rise to a more complete description of these systems to better comprehend the phenomena observed on them. We chose an *ab initio* molecular dynamics technique, the so-called Car-Parrinello molecular dynamics (Car-Parrinello MD), to explore the vibro-rotational degrees of freedom of the system at a given temperature by application of first-principles derived potentials. This method offers a good ratio between computational cost and system size. With actual resources, it is possible to perform simulations of tens of ps of crystalline materials and molecules in solvent. Similarly to the Quantum Mechanics / Molecular Mechanics schemes, we use the resulting Car-Parrinello MD simulations as the starting point for the subsequent electronic structure calculations. The description of the electronic structure of the materials is performed by means of the Complete Active Space Self-Consistent Field Second-Order

Perturbation theory (CASPT2), which is a wave function based method that offers an efficient treatment of electronic correlation effects. Thus, for the first time we developed a procedure to reliably combine the Car-Parrinello MD and CASPT2 methods. On the CASPT2 step, we use the embedded cluster approach to describe crystalline systems or single molecule calculations for coordination complexes. However, this local description of extended systems requires specific methods to reproduce the environmental effects onto the cluster/molecule. Solvent effects on molecular systems can be reproduced by a Polarizable Continuum Model (PCM) with some explicit solvent molecules surrounding the compound. On the other hand, the crystalline environment can be modelled by a finite distribution of point charges that reproduce the Madelung potential on the cluster and a shell of model potentials to reproduce the short range interactions. Additionally, we incorporated for the first time the Direct Reaction Field (DRF) self-consistently in the embedding of crystalline systems, to also account for the polarization of the cluster surroundings to the state transition.

Following the described general goal of the project, we established the subsequent objetives for the present research:

- The development of the necessary computational tools to combine CPMD simulations with CASPT2 electronic structure calculations.
- The description of thermal motion effects to the electronic structure of various molecular and crystalline systems.
- The development of a self-consistent implementation of the DRF in the electronic structure calculations of embedded cluster models.
- The application and testing of the DRF embedding on various crystalline systems to describe charge transfer processes.
- The exploration of the benefits of different solvent models on molecular systems.
- The theoretical description of the MMCT on a bistable model system using the CASPT2 method on a cluster with the DRF embedding.

- The study of the LIESST process on Fe^{2+} SCO complexes by combining Car-Parrinello MD simulations with CASPT2 calculations.

The development of this combined procedure has been performed gradually. The first step consisted on studying the relative stability between the LS and HS states of SCO Fe^{2+} compounds with various model ligands of different σ-donation strength. Moreover, we compared the capability of the CASPT2 method against the Coupled Cluster Single-Doubles method to describe those electronic states. We found that the LS state has contributions from charge transfer configurations, which require the use of a multi-configurational method like CASPT2 to get a proper description of that state (Chapter 2).

On the next step we combined the Car-Parrinello MD simulations with CASPT2 calculations. To validate the results of our procedure we chose a well known system, the cytosine molecule. We described the absorption spectra of four cytosine tautomers in water. Those results show that, by including the molecular dynamics, the band broadening appears naturally on the theoretical spectra. Additionally, the relatively simple cytosine molecule reveals a high complex electronic structure with states of mixed character with contributions from different kinds of electronic transitions (Chapter 3).

At this point, we studied another well known material to test the developed procedure on a crystalline system. We described the NiO absorption spectra by combining Car-Parrinello MD simulations with CASPT2 calculations of embedded cluster models with DRF. The results prove similar benefits on using molecular dynamics with crystalline materials as with the cytosine molecule. In this case, the phononic distortions on the NiO lattice allow the study of electronic transitions that, otherwise, are dipole forbidden on the ideal structure. Moreover, the incorporation of the DRF embedding on the cluster model shows that the electric response of the surrounding lattice to the electronic changes occurred in the active site are important and have large effects on charge transfer processes (Chapter 4).

Once we established the procedure to combine all those three methods and proved their usefulness, we stepped forward to study some bistable systems. We started by the $LaMnO_3$ crystal, which is a prototype perovskite crystal that shows the Colossal Magneto-Resistance phenomenon. The $LaMnO_3$ structure has similitudes to that of the Prussian blue analogues, with a prominent role of cooperative effects. We applied the CASPT2 method on a cluster model with a DRF embedding to describe the MMCT of $LaMnO_3$, which is suggested to occur at $\sim$ 2 eV. We obtained overestimated values of the MMCT transition, but a significant improvement of the theoretical description of these states is achieved (Chapter 5).

Subsequently, we studied the organic radical 1,3,5-trithia-2,4,6-triazapentalenyl (TTTA), which shows photoinduced magnetization with a large hysteresis loop. In this case, we investigate the exchange coupling constant (J) by means of the Difference Dedicated Configuration Interaction (DDCI) method and treating the environmental effects through DRF. The role of the environmental effects in the singlet–triplet splitting is calculated and appears to be low, as expected for the small changes in electronic structure caused by the singlet–triplet transition (Chapter 6).

The final goal of the project has been to apply this procedure to a SCO complex, the $Fe^{2+}(bpy)_3$ coordination complex. We performed the Car-Parrinello MD of the LS state of this Fe^{2+} compound in water and computed, by means of the CASPT2 method, the electronic structure of some extracted conformers from the MD trajectory. The character and arrangement of the lower excited states largely depends on the conformational distortions of the $Fe^{2+}(bpy)_3$ molecule. Moreover, a very compact manifold of states is found in a small energetic region of $\sim$ 1 eV, showing the origin of the ultrafast inter system crossing subsequent to the photon absorption that initiates the LS$\rightarrow$HS transition (Chapter 7).

CHAPTER 2

Spin-crossover in Fe(II) complexes: An *ab initio* study of ligand σ-donation

2.1 Introduction

Spin crossover can be observed in transition metal compounds where low-spin and high-spin states are close in energy. The change of spin state can be induced by external perturbations such as change in the temperature (thermal spin crossover), pressure, or irradiation with light (light-induced excited state spin trapping, LIESST) [3, 9, 10]. When collective effects are important in the thermal spin crossover, the transition temperature upon cooling can be different than the transition temperature upon heating the sample. This leads to very interesting hysteresis phenomena and the corresponding bistability of the system. The induction of spin crossover by irradiation with light is also promising from the technological point of view, especially when the system can be both forced to transform from the low-spin to the high-spin phase and back [11].

The experimental study of spin crossover has a long standing history and, as a consequence of the knowledge obtained from this, technological applications are within reach nowadays. On the contrary, the theoretical study of this phenomenon is less well developed and is in many aspects still in an exploratory stage. The pioneering work of Paulsen and co-workers [12–14] established that standard density functional theory calculations are not accurate enough to reproduce a fundamental property as the stability of the high-spin state with respect to the low-spin state (ΔE_{HL}). This work inspired a large-scale study of the performance of a large collection of different functionals [15–25]. The main conclusions from this work are that (i) good estimates of ΔE_{HL} can be obtained by mixing gradient corrected density functionals with exact exchange, albeit that the optimal mixing is material dependent [15, 16], and that (ii) the direct calculation of ΔE_{HL} can give a huge interval of values depending on the functional [18, 19]. It was recently shown that an indirect recipe of calculating this difference, based on the difference of vertical energies at the equilibrium geometry of the high-spin and low-spin states, gives results that are almost independent on the functional [23].

On the other hand, there is an increasing number of studies devoted to the spin crossover related phenomena based on post Hartree-Fock methodologies [7, 26–

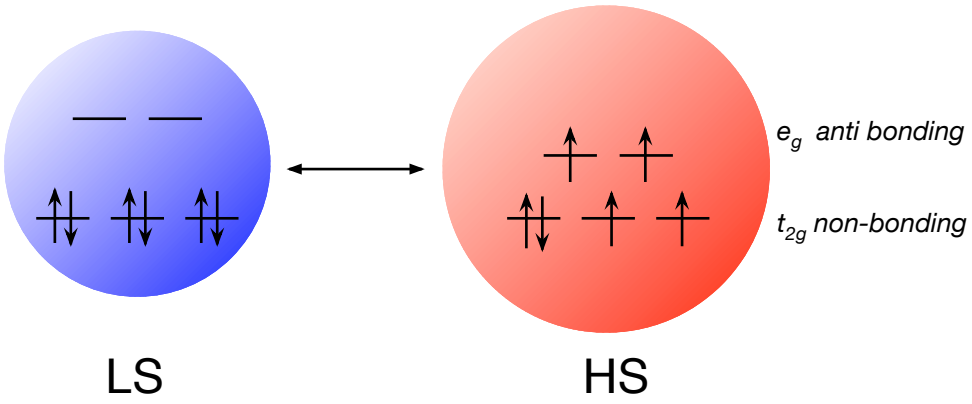

Figure 2.1: Schematic description of the spin crossover process for a TM–3d^6 ion. The low-spin (LS) state on the left has no electrons in the anti-bonding orbitals, while the high spin (HS) state maximizes the exchange interaction between the electrons.

31]. These strategies are based on a multiconfigurational description of the electronic structure and make possible to consider spin eigenfunctions, to treat ground and excited states on an equal footing, and include spin-orbit coupling effects, which are essential to understand the LIESST mechanism. A standard implementation of multiconfigurational self-consistent field (SCF) calculations is given by the complete active space SCF (CASSCF) introduced by Roos and co-workers in the 1980s [32]. Combining CASSCF with multiconfigurational second-order perturbation theory (CASPT2) [33, 34] result in a very successful computational scheme to treat a wide spectrum of problems of chemical interest.

The Racah parametrization scheme gives a rather precise account of the relative energies of the d^n manifolds in transition metal complexes [35] like the ones relevant to spin crossover. An inspection of the Tanabe-Sugano diagram [36] for an octahedral d^6 complex shows that the $^5T_{2g}$ (HS state) and the $^1A_{1g}$ (LS state) are nearly degenerate in a small interval of ligand field strength $10D_q$ of about 2.1 eV, which corresponds to almost twice the ligand field strength of the prototype material NiO containing Ni^{2+}–3d^8 ions [37]. This indicates that spin crossover can only be expected to occur for ligands that exert a strong ligand field on the central metal ion such that the occupation of the anti-bonding e_g

orbitals becomes competitive with the spin pairing in the LS state as illustrated in Figure 2.1.

The largest metal–ligand interaction occurs via the σ-donation of the ligand to the metal ion. When ligands with π-systems are used, the π back-donation may also play an important role. The spectrochemical series orders a collection of ligands by increasing ligand field strength. Here, we will take some representative examples from this series and study with high level quantum chemical techniques the potential energy curves of the HS and LS states of the six-coordinated Fe(II) complexes as function of the ligand–metal distance. The analysis of the calculated wave function along the curves for the different complexes enables us to establish a relation between the occurrence of spin crossover and the covalent interaction between ligand and metal through the σ-orbitals. Furthermore, we calculate the ligand field splitting parameter $10D_q$ in all the complexes and discuss the validity of the monoreferential coupled cluster approach in comparison to the multiconfigurational perturbation theory scheme for the complexes under study.

2.2 Computational Information

The multiconfigurational character of the N-electron wave function in the Fe(II) complexes under study can accurately be described with the complete active space self consistent field (CASSCF) approach. The CASSCF wave function is constructed by performing a full configuration interaction (CI) in a limited valence space (the so-called active space) and simultaneously optimizing both the CI and orbital expansion coefficients. The active space consists of the five Fe–3d orbitals and two ligand σ orbitals of e_g symmetry to provide a balanced description of the σ-donation. To ensure a correct description of the radial correlation of the Fe–3d electrons, five Fe–3d' orbitals were added to the active space [38–41]. This CAS(10,12)SCF gives a balanced description of the different important electronic configurations and has been applied before in many other

applications that were not only restricted to Fe(II) complexes related to spin crossover [42–44].

The CASSCF wave function gives a good description of the electron distribution but lacks important dynamical electron correlation effect. These effects are mainly atomic in nature, and hence, do not strongly affect the electron distribution but may give rise to rather large changes in the relative energies of the different electronic states under consideration. The complete active space second-order perturbation theory (CASPT2) is by now the standard scheme to account for these effects in the case of multiconfigurational wave functions of medium to large sized systems. All electrons are correlated except the deep-core ones (1s, 2s, 2p for P, S and Fe, and 1s for C, N and O).

Previous studies evidenced the importance of extensive basis sets to expand the molecular orbitals [7, 27]. Here, we use basis sets of the atomic natural orbital type, which are especially designed to describe the scalar relativistic effects via the Douglas-Kroll Hamiltonian and the semi-core valence electron correlation. The following contractions of the primitive basis sets are used: Fe (7s,6p,5d,3f,2g,1h); P, S (5s,4p,2d,1f); C, N, O (4s,3p,2d,1f); and H (2s) [45, 46].

Coupled cluster calculations have been performed to validate the CASPT2 results. We use the CCSD(T) variant with the perturbative estimate of the triples following the scheme proposed by Watts *et al.* [47]. All calculations are performed with MOLCAS 7 [48, 49].

The natural molecular orbitals with a marked delocalized character are transformed to atomic-like orbitals by the transformation procedure described in Ref. [50]. This unitary transformation is based on a pair-wise orbital rotation of a mainly metal orbital and a mainly ligand type orbital. The t_{2g}–like Fe–3d natural orbitals are highly non-bonding in character, and hence, do not need to be transformed. However, the two pairs of bonding-antibonding e_g–like active orbitals show important mixing of Fe–3d and ligand–2p basis functions. The expression of the wave function in localized orbitals allows us to decompose the wave function in different valence bond (VB) contributions such as the non

charge transfer configuration (NCT, i.e. the electronic configuration predicted from the ionic model), the ligand-to-metal charge transfer (CT) and the double charge transfer (DCT) electronic configurations.

2.3 Results

The increasing σ-donor strength of the different ligands is reflected in Table 2.1 by the gradual increase of the contribution of the CT configurations in the wave functions of LS and HS states. While the HS wave function of the rather ionic $Fe(H_2O)_6$ complex has weak contributions from the ligand-to-metal CT configurations, these contributions dominate the wave function in the Fe complexes with CO and PH_3 ligands. We observe a more marked CT contribution for the LS state than in the HS state for all complexes. At first glance, this may seem to be counterintuitive since the Fe–ligand distances in the LS equilibrium distance is much smaller than at R_e(HS), see Table 2.2. However, one has to keep in mind that the electron transfer from ligand–p_σ orbitals into the Fe–3d(e_g) orbitals is more favorable in the LS state since the e_g orbitals of Fe^{2+} are unoccupied in the singlet state, while they have two electrons in the quintet state.

The next step is to relate the composition of the wave function for LS and HS state to the possible occurrence of spin crossover phenomena. Table 2.2 lists besides the equilibrium distances also the adiabatic excitation energy of the HS to LS transition, which is defined as the energy difference of both states at their equilibrium distance. Positive ΔE_{HL} values indicate that the HS is more stable than the LS state, and *vice versa* for negative values.

High positive values for ΔE_{HL} are observed for those complexes with a NCT dominated LS state wave function, whereas large negative values are observed for those complexes whose LS state wave function has large contributions from charge transfer contributions. In the first case, the stabilization of the LS state by charge transfer effects is not large enough to create a system with two stable minima. As shown in Figure 2.2, the HS state is much more stable than the LS

Table 2.1: Composition (in %) of the LS and HS state wave function expressed in atomic-like orbitals for a series of Fe(II) complexes. The wave function is decomposed in contributions from the non charge transfer (NCT, Fe–$3d^6$), the charge transfer (CT, Fe–$3d^7$ L^{-1}) and double charge transfer (DCT, Fe–$3d^8$ L^{-2}) electronic configurations.

	LS			HS		
Complex	NCT	CT	DCT	NCT	CT	DCT
$Fe(H_2O)_6$	77.8	20.4	1.4	92.4	7.2	0.1
$Fe(NH_3)_6$	60.3	34.4	4.5	88.7	10.7	0.2
$Fe(NCH)_6$	59.8	34.1	5.2	91.0	8.6	0.1
$Fe(NCS)_2(NCH)_4$	55.3	37.0	6.7	84.4	13.6	0.4
$Fe(NCS)_4(NCH)_2$	54.4	37.9	6.8	88.0	11.4	0.3
$Fe(CO)_6$ [a]	19.8	45.1	27.7	86.6	12.7	0.3
$Fe(PH_3)_6$ [a]	7.7	36.4	40.5	78.5	20.2	0.8

[a] The remainder of the LS state wave function is due to triple CT configurations.

Table 2.2: CASPT2 and CCSD(T) equilibrium distances (R_e in Å) and adiabatic energy difference for the LS and HS states (ΔE_{HL} in cm^{-1}) in a series of Fe(II) model complexes.

	CASPT2			CCSD(T)		
Complex	R_e(LS)	R_e(HS)	ΔE_{HL}	R_e(LS)	R_e(HS)	ΔE_{HL}
$Fe(H_2O)_6$	1.98	2.13	15150	2.00	2.13	11670
$Fe(NH_3)_6$	2.05	2.20	7890	2.07	2.25	5300
$Fe(NCH)_6$	1.91	2.15	2540	1.93	2.15	1500
$Fe(NCS)_2(NCH)_4$	1.88	2.12	-530	–	–	–
$Fe(NCS)_4(NCH)_2$	1.90	2.15	-1300	–	–	–
$Fe(CO)_6$	1.86	2.26	-16700	1.94	2.30	-10100
$Fe(PH_3)_6$	2.22	2.62	-19400	2.29	2.67	-12200

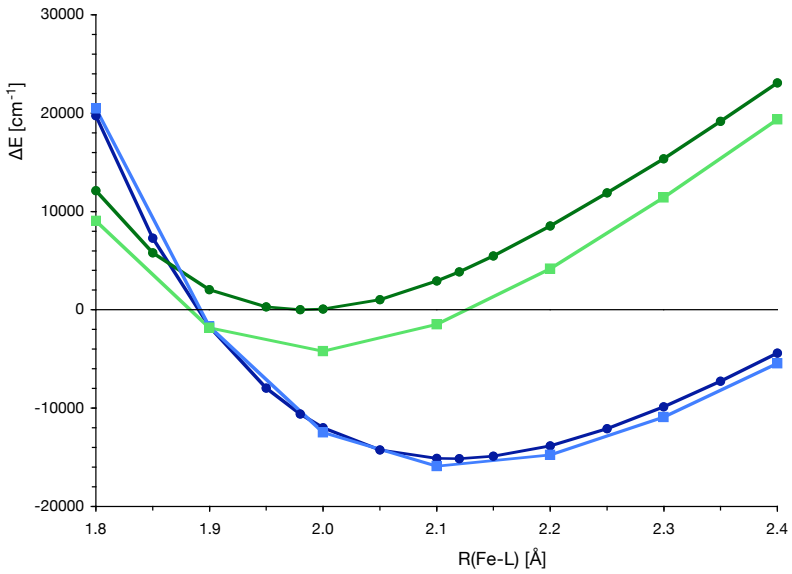

Figure 2.2: CASPT2 (circles) and CCSD(T) (squares) potential energy curves for HS (blue) and LS (green) states of the $[Fe(H_2O)_6]^{2+}$ complex.

state. The difference in stability is such that the minimum of the LS curve is contained within the HS curve. No spin crossover phenomena can be expected for ligands with σ-donor character comparable to the H_2O or NH_3 ligand.

On the opposite side of series, large negative values of ΔE_{HL} are observed for the $Fe(CO)_6$ and $Fe(PH_3)_6$ model complexes. The LS wave function of these complexes is dominated by CT configurations, leading to a significant stabilization of the LS state by ligand-σ donation. This effect is much smaller in the HS state. The large LS stabilization makes impossible the observation of two clearly separated minima, as illustrated in Figure 2.3 for the $Fe(PH_3)_6$ complex. We observe a similar behaviour for the complex with CO ligands.

The three remaining complexes with NCS^- and/or NCH ligands have moderate ΔE_{HL} values ranging from 2500 cm^{-1} to -1300 cm^{-1}. This moderate energy difference is accompanied by a contribution of the CT configuration of roughly

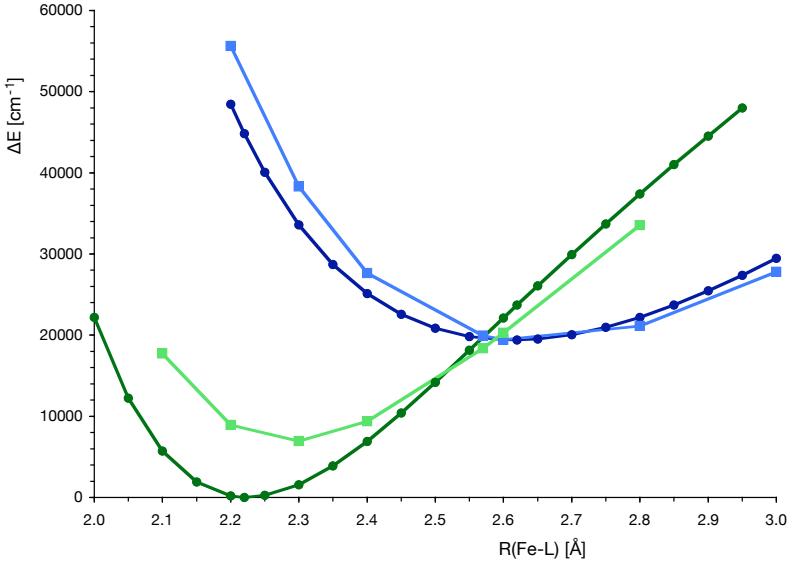

Figure 2.3: CASPT2 (circles) and CCSD(T) (squares) potential energy curves for HS (blue) and LS (green) states of the $[Fe(PH_3)_6]^{2+}$ complex.

40–45%, i.e. a significant but not excessive σ-donation. A very similar composition of the wave function was also found in the tetrazole-based spin crossover complex by Ordejón *et al* [7]. The resulting potential energy curves for HS and LS states as function of the Fe–ligand distance are shown in Figure 2.4. The curves show the typical bistability with clearly separated minima for singlet and quintet state. At low temperatures, when entropy effects are small, the system has a LS ground state with a small Fe–ligand distance. A thermal spin crossover to the HS state is accompanied by an enlargement of the Fe–ligand distance of almost 0.2 Å, in agreement with experimental findings reported for other complexes [10].

The reliability of the applied computational methodology, CAS(10,12) followed by CASPT2, has been subject of various studies [27, 29, 30]. Here, we compare the results with coupled cluster calculations for some of the complexes. The computational requirements for the complexes with NCS ligands made impossible to perform the CCSD(T) calculations for the $Fe(NCS)_2(NCH)_4$ and

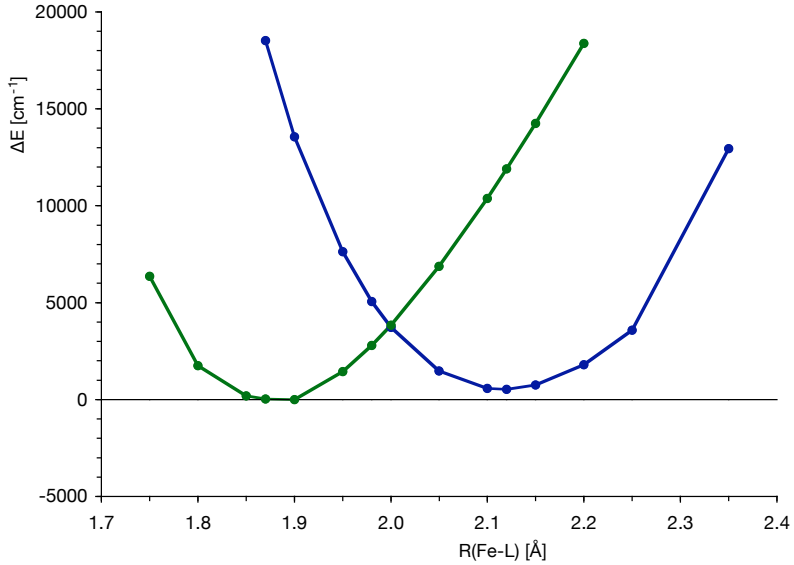

Figure 2.4: CASPT2 (circles) potential energy curves for HS (blue) and LS (green) states of the $[Fe(NCS)_2(NCH)_4]^{2-}$ complex.

$Fe(NCS)_4(NCH)_2$ complexes. The equilibrium distances calculated with the CCSD(T) method differ at most by 0.05 Å from the CASPT2 estimates. The coupled cluster ΔE_{HL} values are in less good agreement with the CASPT2, especially for the complexes with strong σ donating ligands. The squares in Figure 2.2 represent the CCSD(T) relative energies of HS and LS states. The location of the minima and the curvature of both curves is practically identical for CCSD(T) and CASPT2. The only difference lies in the relative position of the HS curve with respect to the LS curve. This results in a slightly smaller ΔE_{HL} for CCSD(T) in comparison with CASPT2.

The situation is different for the $Fe(PH_3)_6$ complex shown in Figure 2.3. The CCSD(T) minima are diplaced to longer distance compared to the CASPT2 estimates and more importantly, the curvature of the LS state deviates significantly from the CASPT2 curve. To answer the question which of the two results is more reliable it is necessary to realize that the coupled cluster method uses a monoconfigurational reference wave function to estimate the electron corre-

lation effects, while CASPT2 is based on a multiconfigurational reference wave function. The electronic structure of the LS state is dominated by the $|e_g^4 t_{2g}^6 e_g^{*0}|$ configuration and the HS state by the $|e_g^4 t_{2g}^4 e_g^{*2}|$ configuration. Here, the e_g orbitals are mainly localized on the ligands and the e_g^* are mainly Fe–3d orbitals. The wave function analysis in Table 2.1 indicates that the CT effects are larger in $Fe(PH_3)_6$ than in $Fe(H_2O)_6$. This is also reflected in the CI coefficients of the wave function expressed in the delocalized molecular orbitals used in the CASPT2 and CCSD(T) calculations. The CASSCF wave function for both LS and HS is almost purely monoconfigurational in the case of $Fe(H_2O)_6$ with almost no other contribution than the $|e_g^4 t_{2g}^6 e_g^{*0}|$ or $|e_g^4 t_{2g}^4 e_g^{*2}|$ configurations. This monoconfigurational character is maintained for the HS state in its equilibrium geometry for $Fe(PH_3)_3$, but the weight of the $|e_g^4 t_{2g}^6 e_g^{*0}|$ configuration decreases to 87% for the LS state at $R_e(\mathrm{LS}) = 2.22$ Å. At this distance, the HS wave function has also more important contributions from other configurations than the above mentioned. This strongly suggests that the validity of the CCSD(T) method for complexes with large σ donation –reflected in large CT contributions to the wave function– is limited and that a multiconfigurational treatment of the electronic structure is mandatory.

Finally, we discuss the relation between the ligand field strength parameter 10Dq, the occurrence of spin crossover and degree of σ-donation. For this purpose we calculate the energy difference between the ${}^5T_{2g}$ and ${}^5E_g$ states at the equilibrium distances of the LS and HS states for all complexes. The electronic configurations of these states are dominated by the $t_{2g}^4 e_g^{*2}$ and $t_{2g}^3 e_g^{*3}$ electronic configuration, respectively. In a one-electron reasoning, the energy difference of these two configurations measure the splitting of the Fe-3d(e_g) and Fe-3d(t_{2g}) orbitals, i.e. the ligand field splitting. The results are listed in Table 2.3. Although there seems to be a tendency of increasing 10Dq with the increase of σ donating character of the ligand at R_e(LS), the trend is not regular and especially for the values at R_e(HS) cannot serve as a guide to order the complexes by increasing σ donor ligands. There are basically two reasons to explain these irregular trends. In the first place, it is well known that 10Dq is strongly distance dependent. The value of R_e is not the same in all the complexes which makes it more difficult

Table 2.3: CASPT2 estimate of the ligand field strength parameter 10Dq (in eV) obtained from the energy difference between the ^{5}T (t^4e^{*2}) and ^{5}E (t^3e^{*3}) electronic states.

Complex	10Dq R_e (LS)	10Dq R_e (HS)
$Fe(H_2O)_6$	1.64	1.10
$Fe(NH_3)_6$	2.69	1.51
$Fe(NCH)_6$	3.21	1.49
$Fe(NCS)_2(NCH)_4$	2.93	1.26
$Fe(NCS)_4(NCH)_2$	2.54	1.07
$Fe(CO)_6$	4.90	1.37
$Fe(PH_3)_6$	3.81	1.34

to compare the results between the different species. In the second place, the assumption that 10Dq is equal to the energy difference of the two mentioned quintet states is only valid in a purely ionic model neglecting the charge transfer effects in the wave function. As discussed before, these charge transfer effects are not constant along the series of complexes, and hence, introduces a second uncertainty in the determination of 10Dq and the subsequent comparison of the parameter for the different complexes.

2.4 Conclusions and Summary

Multiconfigurational second-order perturbation theory has been applied to study octahedral Fe(II) complexes with a series of model ligands. The analysis of the wave function expressed in atomic orbitals reveals a direct relation between the weight of the ligand-to-metal charge transfer configurations and the relative stability of the LS state versus HS state. For LS wave functions with a contribution between 40-45% of CT configurations, the HS and LS states are nearly degenerate and the minima in the potential energy curve are well separated, giving all the essential ingredients for spin crossover phenomena to occur. In the complexes with larger CT contributions, the LS state is over-stabilized ($Fe(CO)_6$

and $Fe(PH_3)_6$), while for the complexes with small CT contributions, the HS state is much lower in energy.

CASPT2 and CCSD(T) results obtained for the complexes with weak σ donors are in good agreement. This establishes the reliability of the second-order perturbation theory treatment of electron correlation effects. The deviations observed for the stronger σ donor ligands can be ascribed to the monoconfigurational reference wave function used in the CCSD(T) calculations. For these complexes, the multiconfigurational character of the wave function becomes so important that electronic structure calculations cannot be based anymore on single reference wave functions.

The increasing σ donor character of the ligands causes an increased ligand field at the Fe(II) ion. In an ionic model of the electronic structure, the energy difference of the ${}^5T_{2g}$ and ${}^5E_g$ electronic states parametrizes the ligand field strength. However, we found two problems in using this energy difference to follow the evolution of the ligand field strength (10Dq) along the series of ligands: (i) the strong distance dependence of 10Dq and (ii) the limited validity of the purely ionic description of the electronic structure of the complexes.

UNIVERSITAT ROVIRA I VIRGILI
THEORETICAL DESCRIPTION OF ELECTRONIC EXCITATIONS IN EXTENDED SYSTEMS:
BEYOND THE STATIC MATERIAL MODEL
Alex Domingo Toro
DL:T. 1705-2011

UNIVERSITAT ROVIRA I VIRGILI
THEORETICAL DESCRIPTION OF ELECTRONIC EXCITATIONS IN EXTENDED SYSTEMS:
BEYOND THE STATIC MATERIAL MODEL
Alex Domingo Toro
DL:T. 1705-2011

CHAPTER 3

The absorption spectrum of cytosine tautomers: beyond the static approach

3.1 Introduction

The sensibility of the DNA molecule to UV light absorption can lead to mutations of the genetic material and eventually carcinogenesis. However, the DNA molecule has effective mechanisms of deactivation to avoid genetic damage. The constituent nucleobases of DNA have a prominent role in this process because all four bases (adenine, thymine, guanine and cytosine) have not only large absorption coefficients on the UV range, but also the monomers and base-pairs show intrinsic molecular fast decays upon electronic excitation. [51, 52]

Even though the four nucleobases are relatively simple molecules, the understanding of their electronic structure is complex. The DNA base cytosine is known to have multiple decay pathways that involve various excited states. The UV radiation of cytosine produces primarily dipole allowed transitions to singlet $\pi\pi^*$ states, the so-called bright states, and dipole forbidden transitions to singlet $n\pi^*$ states in a lower rate, the so-called dark states. Theoretical and experimental research on the potential energy surfaces (PES) of the ground state and the lowest excited states of cytosine have found many plausible radiationless deactivation mechanisms for this chromophore. Nowadays, the proposed decay pathways for cytosine include multiple internal conversion via conical intersections (CI) at different regions of the hyper-PES between various $^1\pi\pi^*$, $^1n\pi^*$ states and the ground state [53–57]. A relaxation mechanism through an intersystem crossing (ISC) to the lowest $^3\pi\pi^*$ state has been also suggested [58]. Furthermore, some decay paths involving conformational distortions [59] or excited tautomerization [60] pointed out the significant role of the structural flexibility of cytosine. These results prove the large versatility and high efficiency of the cytosine molecule to decay back to the ground state but, additionally, the high complexity of its electronic structure.

At first sight, the absorption spectra of cytosine are relatively simple. They show basically two intense and broad absorption bands with some additional minor features depending on the experimental conditions. A brief summary of available spectroscopic data for cytosine is shown in Table 3.1. The main bands

Table 3.1: Summary of spectroscopic data for cytosine.

		Transition Energy (eV)					
Spectrum medium	Ref.	I	II	III	IV	V	VI
Trimethyl phosphate	[65]	4.5	5.2		6.1,6.7		
Vapor	[66]	4.3					
Water (pH=7)	[67]	4.7					
Water (pH=2)	[67]	4.5			5.9		
Crystal monohydrate	[68]	4.6					
Water[a]	[62]	4.7	5.3	5.6	6.2	7.7	8.1
Ethanol	[69]	4.5	5.2		6.0		

[a] Transitions I-IV adjusted from crystal polarized reflection spectra. Transitions V-VI estimated from thin film spectrum.

of the absorption spectra of cytosine correspond to transition I ($\sim$ 4.5 eV) and IV ($\sim$ 6.0 eV), which are transitions in the molecular plane assigned to $\pi\pi^*$ excitations [61]. Transitions II and III ($5 - 6$ eV) are usually masked by the more intense $\pi\pi^*$ bands, becoming difficult their characterization by means of experimental polarization data and transition moments [62–64].

The theoretical research of the electronic structure has put some light into these weak absorptions. Early calculations of the cytosine molecule using an all valence electrons Self Consistent Field Molecular Orbital with Configuration Interaction (SCF-MO-CI) resulted in detailed information about the characteristics of both the $\pi\pi^*$ [70] and $n\pi^*$ [71] transitions, identifying the transition II at 5.2 eV as a $n\pi^*$ excitation from the non-bonding orbital of the carbonyl group. Moreover, Matos *et al.* used the Complete Active Space Self Consistent Field (CASSCF) method to treat the complete π electronic system of cytosine. They found that the lone pairs of the O and N atoms have a large effect on the electron correlation of the molecule and calculated the three lowest $\pi\pi^*$ transition energies to be 5.6, 6.9 and 8.1 eV [63]. Subsequent calculations by Fülscher *et al.* included $\sigma - \pi$ polarization through the Second-Order Perturbation theory using a CASSCF reference wave function (CASPT2) to treat the dynamical correlation of σ electrons. They obtained more accurate results with this method and

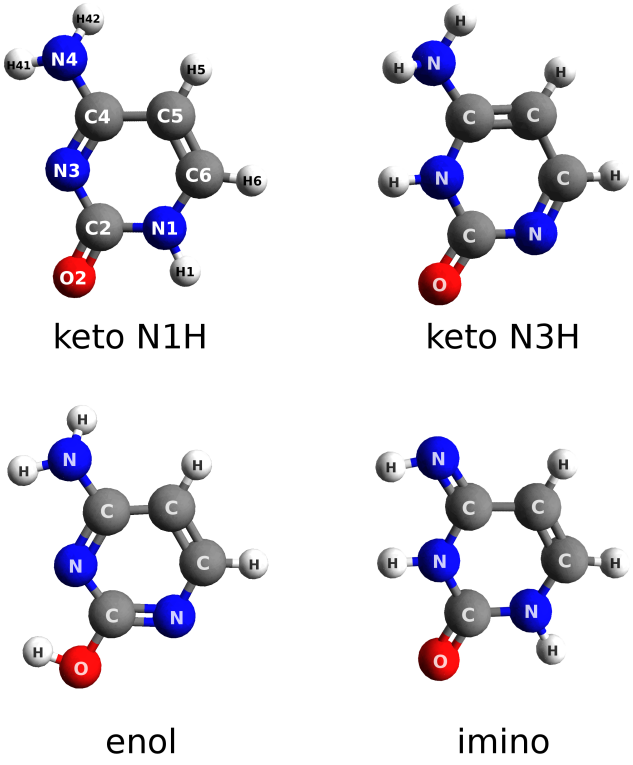

Figure 3.1: Structures of four tautomeric forms of cytosine.

calculated the transition energies of four $\pi\pi^*$ states at 4.4, 5.4, 6.2 and 6.7 eV, a $n\pi^*$ transition as the second excited state at 5.0 eV and a possible higher $n\pi^*$ transition at 6.5 eV [72]. Petke *et al.* performed Multi-Reference CI calculations of cytosine that lead to similar conclusions for the lowest transitions, but pointed at the complexity of the higher energy region due to spectral congestion above 5.2 eV [64].

The influence of different solvents to the electronic structure of cytosine has been another important subject of research. The absorption spectrum of cytosine depends on the dielectric constant of the solvent (Table 3.1) and, in the case of water, on the pH value [67, 73]. Furthermore, cytosine has various tautomeric forms that can be classified based on their functionalization in three

basic structures: keto, enol and imino (Figure 3.1). The population of these tautomers varies depending on the characteristics of the solvent and, additionally, they have quite different electronic properties complicating even more the interpretation of spectroscopic data [74]. Even though various tautomeric structures can be present for a given solvating condition, the enol form is the most stable in apolar solvents and gas phase, while the keto form is the most stable in polar solvents [69, 75–79].

There has been much effort to incorporate aqueous solvent effects on the theoretical models of cytosine and other organic molecules to achieve biologically relevant data [80]. To simulate the electrostatic effect of the solvent in the computational model one commonly includes some kind of continuum reaction-field around the quantum system [81–85]. Additionally, some explicit water molecules can be included in the electronic structure calculation to achieve a more accurate description of the solute–solvent interactions [86–89]. The main known effect of aqueous solvent to the electronic structure of cytosine is a blue shift of the $n-\pi^*$ transitions due to stabilization of the electron lone pairs, which pushes the lower dark excitations to the spectral congestion region.

The cytosine tautomer found in the Watson & Crick structure of DNA is the keto form [90]. However, the large capability of the nucleobases to transfer protons and the charge transfer phenomena through the nucleobases stacks in the DNA chain [91, 92] can lead to tautomerization of the DNA bases. It has been suggested that the tautomerization of cytosine occurs primarily through ionic structures [75] and that photoinduced tautomerization could offer extra pathways for deactivation [60, 86]. Moreover, work on other biologic systems like urocanic acid showed the role that different tautomers can have on the absorption spectrum [93]. Thus, it becomes important to consider not only the keto form of cytosine but also its other tautomeric structures to understand the electronic properties of cytosine related biologic systems.

The main drawback of the theoretical models described so far is that they are limited to a static description of the system. Although it is possible to treat different tautomers and include solvent effects in the calculation, only ideal

structures of the molecule have been studied so far. However, cytosine is known to be very flexible and easily looses its planarity. Molecular dynamics simulations using the Car-Parrinello scheme explored the conformational space of the DNA bases showing a wide range of accessible distortions for this molecule [94]. Thus, once a cytosine molecule deviates from planarity, it is not strictly possible to talk about π and n states and $\pi\pi^*$ and $n\pi^*$ transitions, because σ, π and n MOs start to mix and the interpretation of the single contributions to the absorption spectra turns difficult to perform. Nevertheless, the inclusion of the vibro-rotational degrees of freedom on the theoretical study of these compounds is required to achieve a good understanding of their electronic structure. Nowadays, it is becoming rule to combine molecular dynamics simulations with QM/MM calculations to study biologic systems [95–99] and the cytosine molecule is no exception [56, 57, 100, 101]. Hence, this theoretical framework incorporates the conformational evolution of the system at a given temperature plus the effect of the solvent and sophisticated electronic structure calculations.

The aim of the present work is to continue developing the *ab initio* theoretical description of the cytosine molecule by combining Car-Parrinello molecular dynamics (Car-Parrinello MD) [102] with the Complete Active Space Self-Consistent Field Second-Order Perturbation theory (CASPT2) [32, 34]. We study the conformational space of four tautomeric forms of cytosine in water (Figure 3.1) by means of Car-Parrinello MD simulations. Subsequently, on a representative sample of the resulting trajectories, we perform CASPT2 calculations to obtain an accurate description of the electronic structure of each conformation. The solvent effects are incorporated on the CASPT2 step through two solvent models, the Polarizable Continuum Model (PCM) [103] and a combination of PCM including some explicit water molecules. The resulting data set for each tautomer is combined to generate its absorption spectrum in water. We offer a detailed view of the underlying structure of the absorption spectrum of cytosine, comparing the two solvent models and analysing the large mixing observed between the different transition types.

3.2 Computational Scheme

We performed Car-Parrinello MD simulations for each tautomeric form of cytosine considered in this work, namely the keto N1H, keto N3H, enol and imino forms (Figure 3.1). All simulations were performed in a box of 12.5487 Å side length containing 60 water molecules and 1 cytosine molecule. The molecular dynamics conditions were set according to the previous work by Isayev *et al* [94] of cytosine in vacuum. The core electrons are described by Troullier-Martins normconserving pseudo-potentials [104]. The electronic potential was calculated by means of the BLYP density functional [105, 106] using a plane waves basis set with a cut-off of 80 Ry. The system was first equilibrated at 300 K and then maintained at a steady temperature with a Nosé-Hoover chain thermostat [107, 108]. All H atoms are deuterium isotopes to avoid the high frequency hydrogen stretchings and be able to use a larger time step of 0.121 fs with a fictitious electron mass $\mu = 700$ a.u. to improve the computational cost [109]. For each tautomeric form 100 conformational structures were extracted from a trajectory of 2 ps. The MD simulations were carried out with the CPMD software version 3.11.1.

The 400 conformers selected from the Car-Parrinello MD simulations are the ones used in the electronic structure calculations of the excited states of cytosine. To ensure the sample representativeness of this set of structures we analysed the degree of puckering of their aromatic ring in terms of the Cremer-Pople (CP) parameters [110], which offer a systematic method to measure the distortion of each conformer and classify them following the Boeyen's scheme [111]. All structures are classified in symmetrical non-planar conformations based on their CP parameters Q, θ and ϕ. The Q parameter serves as a measure of ring planarity, being the more planar structures the ones with a smaller Q. The conformers with a weighted average torsion angle smaller than $\pm 5°$ are considered planar, which corresponds to Q values smaller than 0.1 Å. Figure 3.2 shows the relative population of planar structures and the pronounced loss of planarity of the four tautomeric forms of cytosine. Only three conformations out of ten can be considered as planar. The degree of distortion of the four tautomers is very

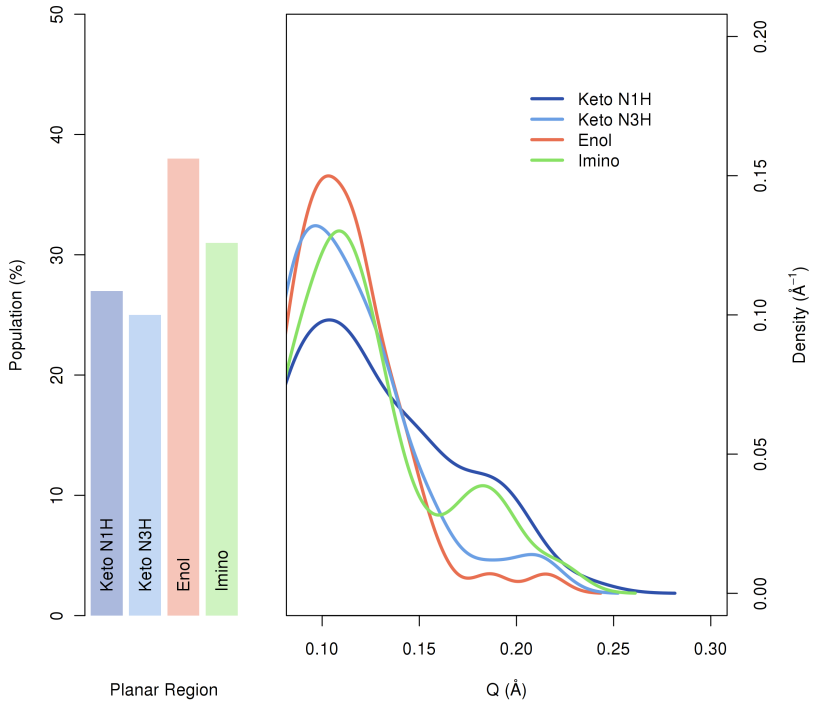

Figure 3.2: Degree of puckering of the cytosine aromatic ring for each tautomeric form. Left: Proportion of planar structures. Right: Value of the Q parameter for non-planar structures.

similar and all of them have significant smaller Q values in water than in the gas phase [94]. Furthermore, the tautomeric forms with a protonated N3 ring atom show slightly larger average distortions. This behaviour could be ascribed to a larger steric repulsion caused by the N3 hydrogen atom on the out-of-ring heteroatoms. The other two parameters θ and ϕ are used to identify the type of distortion of the conformer and assign them to one of the six symmetrical forms of a molecule with a six-membered ring. Table 3.2 analyses the proportion of the symmetrical forms between the different tautomers of cytosine. The percentage of chair like forms is low for all tautomers compared with the planar and boat like forms, which are the most abundant. The presented analysis was performed using the PLATON package [112].

Table 3.2: Classification in the six symmetrical distorted and planar forms of the 100 conformational structures of the four cytosine tautomers.

	Relative Proportion (%)			
Symmetrical Form	Keto N1H	Keto N3H	Enol	Imino
Planar	27	25	38	31
Chair	2	3	1	5
Half-Chair	13	5	7	12
Envelope	14	17	13	14
Screw-Boat	18	19	12	12
Boat	13	14	20	16
Twist-Boat	13	17	9	10

The aqueous solvent effects in the electronic structure calculations were computed by means of a PCM to reproduce the electrostatic interaction of water with the cytosine molecule. The electronic response of the solvent upon absorption is partially defined by the ground state properties of the solute, the so-called slow component, and the excited final state, the so-called fast component. Moreover, we performed a second set of calculations for all the structures including in the wave function some explicit water molecules surrounding the cytosine molecule, in addition to the PCM wrapping. Hence, the effect of hydrogen bonding between the solute and closer water molecules can be incorporated into the electronic structure. Those explicit water molecules come directly from the Car-Parrinello MD, maintaining their relative orientation to the cytosine conformer and being selected based on their distance to the electronegative atoms of the molecule.

The two keto tautomers have three water molecules added, whereas the enol and imino tautomers have four explicit water molecules. This choice is based on the number of available sites for H-bonding. We consider the interaction of water with the functional groups and the heteroatoms of the ring. Therefore, the keto tautomers have three main interaction sites with the solvent, the carbonyl and amine groups and one lone pair of a N atom on the ring. In the case of the enol and imino tautomers, we add an additional water to maintain the balance

between the two N atoms of the ring. Figure 3.3 shows the relative orientation of the selected explicit water molecules on the cytosine tautomers. Even though each cytosine conformer has its closest water molecules particularly oriented, they are found primarily positioned near the lone pairs and the various functional groups, as expected. The superposition of the water molecules extracted for all conformers show how the polarity of the tautomer affects the mobility of the first solvating shell. The water molecules are significantly more fixed along the MD simulation of the enol tautomer than for the less polar keto forms.

The scope of this work is restricted to the lowest 9 eV region of the absorption spectrum of cytosine, not only to cover the largely studied first and second intense broad bands but also to explore the higher energy features observed above 7 eV [62]. Thus, we performed CASPT2 calculations of the twelve lowest singlet excited states of each conformer of cytosine with the two solvent models proposed, totalling 800 electronic structure calculations. The active space (CAS) of these calculations is formed by 14 electrons in the eight π orbitals plus two non-bonding σ orbitals. This CAS allows the description of the $^1\pi\pi^*$ and $^1n\pi^*$ transitions that contribute most to the absorption spectra of cytosine with an accurate treatment of the correlation from the lone pair electrons [63] and the $\sigma - \pi$ polarization [72]. The basis set for the cytosine molecule is of the Atomic Natural Orbitals (ANO) type including scalar relativistic effects [45] to obtain an optimum treatment of correlation and polarization. The C, N and O atoms of cytosine have (4s,3p,2d,1f) contracted basis functions and the H atom a (2s,1p) contracted set. The contracted basis set employed for the explicit water molecules is (3s,2p,1d) for the O atom and (2s,1p) for the H atom. These basis sets are large enough to describe all considered valence states of cytosine. We performed the CASPT2 calculations with a shift factor of 0.20 a.u. [113], which we previously tested to be the minimum value to eliminate possible intruder states. The intensity of the eleven lowest electronic transitions was computed by State Interaction calculations between the ground state and all the excited states at the CASPT2 level, inserting the transition dipole operator in the Hamiltonian [114]. The electronic structure calculations were carried out with the MOLCAS 7 package [48, 49]. The resulting data from the 800 calculations

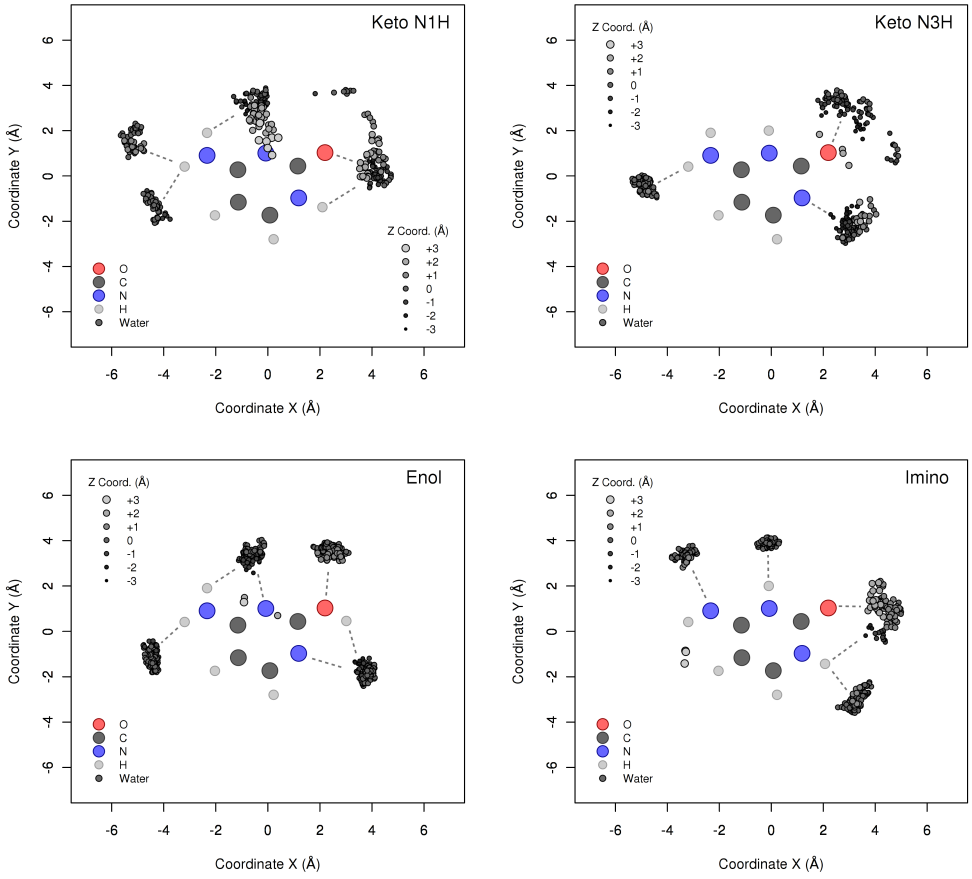

Figure 3.3: Relative orientation of the selected water molecules on each tautomeric form of cytosine: Keto N1H (top left), Keto N3H (top right), Enol (bottom left) and Imino (bottom right). Each graph is a superposition of the position on the moleclar plane of all water molecules chosen along the 100 conformations (dark dots). The H-bonding formed by the solvent molecules is qualitatively represented by dashed lines to the respective ideal tautomeric structure.

was statistically treated with the R package [115] to generate the corresponding spectra by means of kernel density estimations with Gaussian kernel functions of 0.13 ± 0.01 eV of bandwidth (bw), depending on the characteristics of the data set.

3.3 Results

We obtained the absorption spectrum of the keto N1H, keto N3H, enol and imino tautomers in water. For each tautomer we show two spectra, one using a PCM solvent model and another with a PCM including some explicit water molecules. Both spectra are compared and analysed in the next sections. Additionally, to check the molecular description obtained by the combination of molecular dynamics with CASPT2 calculations, we show the energetic evolution of each tautomer along the Car-Parrinello MD simulation. The energy values of spectroscopic properties are given in eV and the analysis of the relative energy between the four tautomers is done in kcal mol^{-1} to ease the comparison with previous studies.

Relative Stability of Cytosine Tautomers

Figure 3.4 shows the CASPT2 energies of the 400 conformers selected from the Car-Parrinello MD simulations of the considered cytosine tautomers. We compared the relative energy of the electronic ground state of all the structures using a PCM solvent model of water. We did not use the solvent model including explicit water molecules to make easier the analysis. A rigorous study of the relative stability of the cytosine tautomers in water is out of the scope of the present work, because it is much more complex than what we can obtain from the present calculations. Nonetheless, this straightforward comparison served to check that the description of the different tautomers offered by the combination of Car-Parrinello MD with CASPT2 is correct.

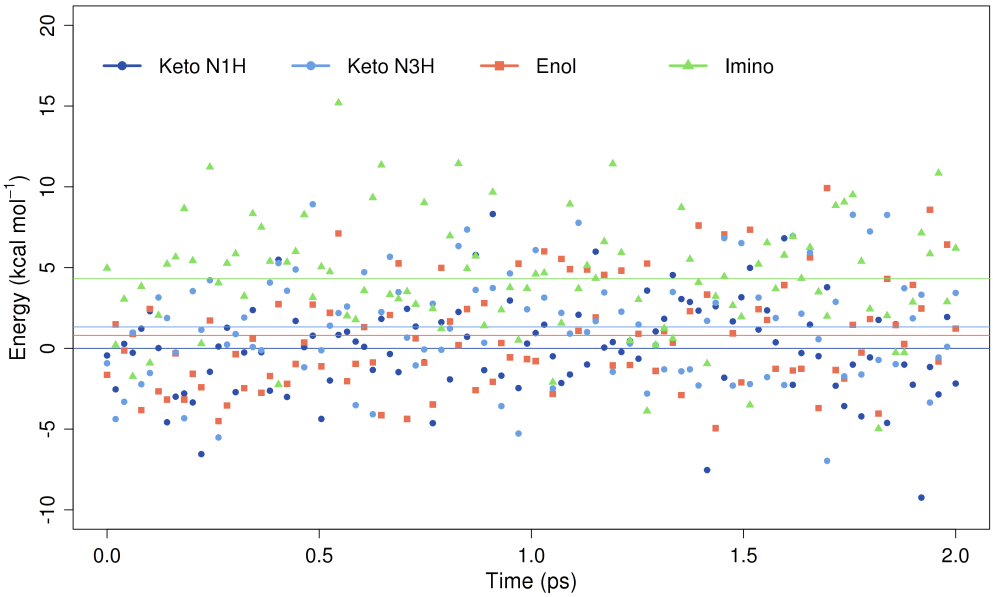

Figure 3.4: Ground state energy of the 400 conformers extracted from the Car-Parrinello MD simulations. Results from CASPT2 calculations using a PCM solvent model for water. The reference energy has been set to the average energy of the keto N1H tautomer. Horizontal lines represent the average energy of each tautomeric form.

The tautomer with the lowest energy is the keto N1H, followed by the enol at 0.8 kcal mol^{-1} higher energy, the keto N3H at 1.3 kcal mol^{-1} and the imino form being the most energetic at 4.3 kcal mol^{-1}. These results are in good qualitative agreement with previous theoretical studies about the relative stability of cytosine tautomers in water [69, 82, 83, 86]. The most stable form in water is known to be the keto N1H, followed by the enol tautomer. The keto N3H and imino forms are both more unstable but their difference in energy varies depending on the theoretical model employed. Our results show that the energy between the four tautomers ranges from 1 to 5 kcal mol^{-1}. These values are in good agreement with other theoretical studies that obtained differences in energy smaller than 10 kcal mol^{-1} using diverse methods. Such small energetic differences suggest that the barriers of the tautomerization processes of cytosine can be easily overcome at room temperature [116]. Actually, the energetic fluctu-

ations of these tautomers during the MD simulation is larger than 5 kcal mol^{-1}, being each of the four tautomers the lowest-energy form at some point of the simulation.

Absorption Spectra of Cytosine Tautomers

The spectra of cytosine tautomers are shown in Figures 3.5, 3.7, 3.8 and 3.9. The global absorption spectra has been decomposed in its individual contributions for each transition type, the $\pi\pi^*$, $n_O\pi^*$ and/or $n_N\pi^*$. Since the wave function describes the complete electronic system involved in this kind of excitations, we know in detail the characteristics of those excited states. However, the classification of transitions between the $\pi\pi^*$ and the $n\pi^*$ is not straightforward. Once the molecule becomes distorted, it is not strictly possible to talk about the symmetric features of the planar structure. The MOs can mix formal aromatic π orbitals with σ orbitals to some degree. Moreover, the MO approach employed in these calculations is intrinsically delocalized, which can result in non-bonding σ orbitals spanning over two atoms with lone electron pairs. Therefore, the breakdown of the total absorption spectrum has been done by thoroughly analysing the contributions to the orbitals in the CAS and by a population analysis of the atoms in the excited states.

We started by identifying all the active orbitals of each conformer by means of their atomic orbital coefficients. We focused in finding the non-bonding orbitals of the corresponding O and N atoms with lone pairs. No attempts were made to classify the remaining π orbitals. The deviations from the strict π symmetry of the planar geometry are significant, making it too complicated to discriminate between the $\pi\pi^*$ transitions. The next step consisted in distinguishing those electronic transitions that significantly change the population of the non-bonding orbitals. We set a minimum criteria for the non-bonding orbitals of 0.4 electrons of difference between the ground state and the excited state to accept those transitions as $n\pi^*$ excitations. The rest of transitions were assigned to $\pi\pi^*$.

It must be noted that in the non-ideal conformers taken from the simulation, the composition of the twelve lowest states is not equal for each structure of a single tautomer. The proportion of $n\pi^*$ and $\pi\pi^*$ transitions varies from one structure to another, resulting in a total number of different transitions found along the series of conformers to be larger than eleven. Depending on the structural distortions of the conformer it can show either a complete lack of $n\pi^*$ transitions or more $n\pi^*$ than $\pi\pi^*$ excitations.

Keto N1H tautomer. Figure 3.5 shows the computed absorption spectra of the cytosine keto N1H tautomer in water. We have identified eight $\pi\pi^*$, four $n_O\pi^*$ and three $n_N\pi^*$ transitions along all conformers of this tautomer. The number of these transitions is independent of the solvent model employed. The explicit water molecules cause a slight blue shift of ~ 0.2 eV on all transitions except for a few $\pi\pi^*$ of the high absorption band that remain stable. The major effect of the inclusion of the water molecules in the calculation is a large increase on intensity of some $n_O\pi^*$ excitations. These $n_O\pi^*$ are located in the region of spectral congestion around $\sim$ 6 eV, where the most intense $\pi\pi^*$ transitions occur. This characteristic suggests that the water molecules could favour the π character of these transitions, increasing the overlap between the involved states and, consequently, increasing their absorption. Additionally, the three water molecules improve the description of the highest excited states, reducing the mixing between the $\pi\pi^*$ and $n_O\pi^*$ transitions observed at 9 eV in the PCM spectrum.

There are four pure $\pi\pi^*$ bands in the spectrum of the keto N1H, the first absorption band located at 4.5 eV and the two peaks at 7.7 and 8.1 eV, which mask a fourth transition at 8.4 eV. The other spectral features that can be unequivocally assigned to single excitations are two optically nearly inactive transitions, a $n_N\pi^*$ at 6.9 eV and a $n_O\pi^*$ at 9.2 eV. The remaining electronic transitions appear in the high absorption band at $\sim$ 6 eV, which is formed by a mix of various absorptions. The transitions observed can be grouped in three main bands that correlate rather well with the bands identified by Zaloudek *et al.* [62]. Transition II has contributions of all three types of excitations, transition III is quite intense and formed equally by $\pi\pi^*$ and $n_O\pi^*$ absorptions, and

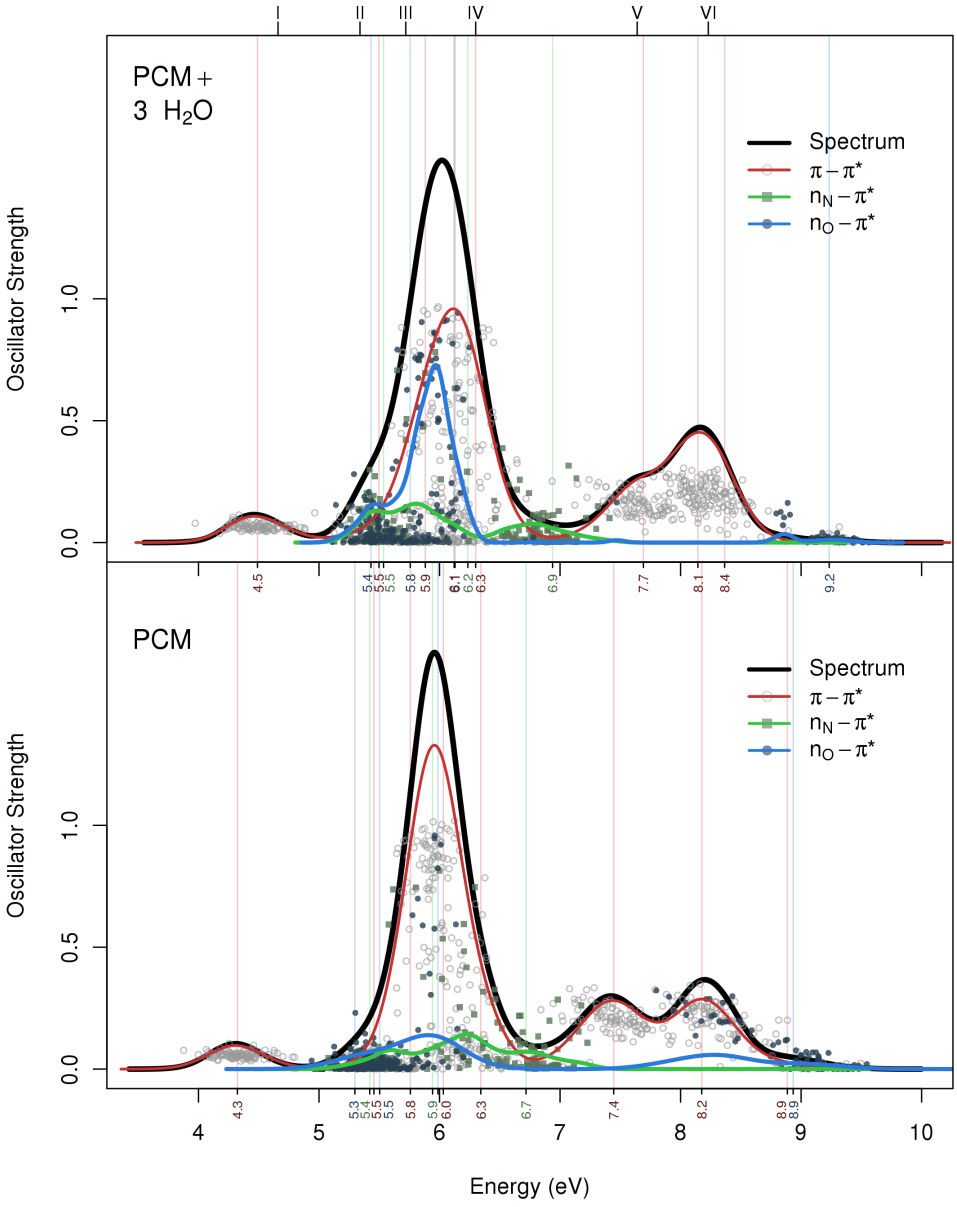

Figure 3.5: Computed absorption spectra of cytosine keto N1H tautomer. Result from 100 conformers using a PCM solvent model (bottom) and, additionally, with 3 explicit water molecules (top). Density estimation with Gaussian kernel functions ($bw = 0.14$ eV). Roman numbers on top mark the experimentally observed features [62].

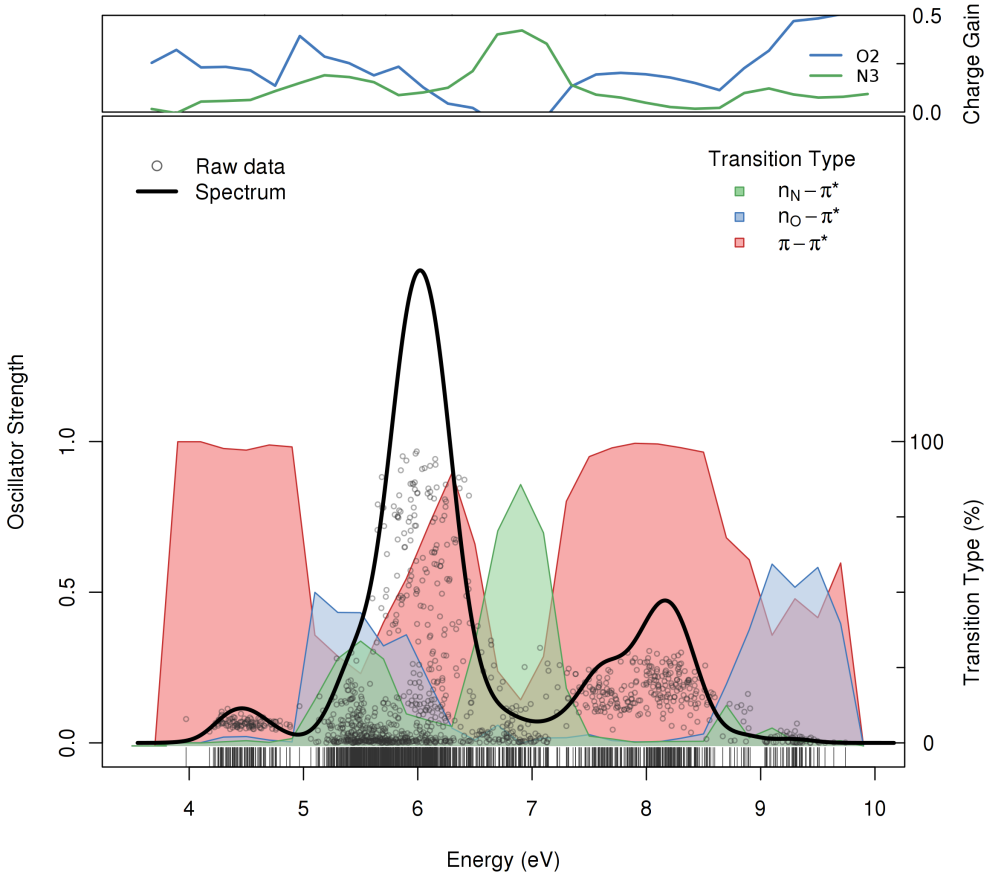

Figure 3.6: Analysis of the absorption spectra of cytosine keto N1H tautomer with 3 explicit water molecules. The colored graphs behind the spectrum show the percentage in intervals of 0.2 eV of each type of transition and the graph on the upper part shows the LoProp population analysis on the O and N atoms with lone pairs.

transition IV is raised basically by two $\pi\pi^*$, which seem to correlate to the E_{1u} state of benzene as suggested by Tinoco *et al.* [65]. Furthermore, Transition I clearly corresponds to the first $\pi\pi^*$ band at 4.5 eV. On the higher energy region, we observe three $\pi\pi^*$ transitions that match very accurately in energy and band morphology to transitions V, formed by one $\pi\pi^*$, and transition VI, formed by two $\pi\pi^*$. Even though the computed spectrum is much more complicated than previously expected it has a very good agreement with the experimental data of this tautomer.

We performed a second analysis of the absorption spectrum of the keto N1H tautomer to confirm the results obtained by the classification of transitions previously made. We calculated in intervals of 0.2 eV the percentage of absorptions assigned to each type of electronic transition considered for the keto N1H form, the $\pi\pi^*$, $n_O\pi^*$ and $n_N\pi^*$. Additionally, we computed the population of the O and N atoms with lone electron pairs, namely the O2 and N3 atoms, by means of the LoProp partitioning scheme [117]. Figure 3.6 shows a graphical representation of both data for comparison. The charge variation on the N atom correlates well with the regions of the spectrum with large contributions of $n_N\pi^*$ transitions, the region between 5 and 6 eV and the $n_N\pi^*$ transition at 6.9 eV. Moreover, the agreement between the charge gains of the O atom and the assignments of $n_O\pi^*$ transitions performed is also good. The larger charge gains for O are found primarily in the 5–6 eV region and at energies higher than 9 eV, where the $n_O\pi^*$ bands have been identified. The non-zero charge gain for O in some regions of the spectrum dominated by $\pi\pi^*$ transitions is due to the π orbital of the O atom, which usually forms a MO localized on the carbonyl group. Therefore, the $\pi\pi^*$ transitions involving that π MO will produce significant changes in the charge of the O atom. This is not the case for the N atom, which will delocalize the charge to some part of the pyrimidine ring. This comparison shows that the breakdown performed on the absorption spectra is valid.

Keto N3H tautomer. Figure 3.7 shows the computed absorption spectra of the cytosine keto N3H tautomer in water. This tautomer has one fewer $n_O\pi^*$ transition compared with the keto N1H. We have identified eight $\pi\pi^*$, three $n_O\pi^*$ and three $n_N\pi^*$ transitions in total. The number of these transitions is independent

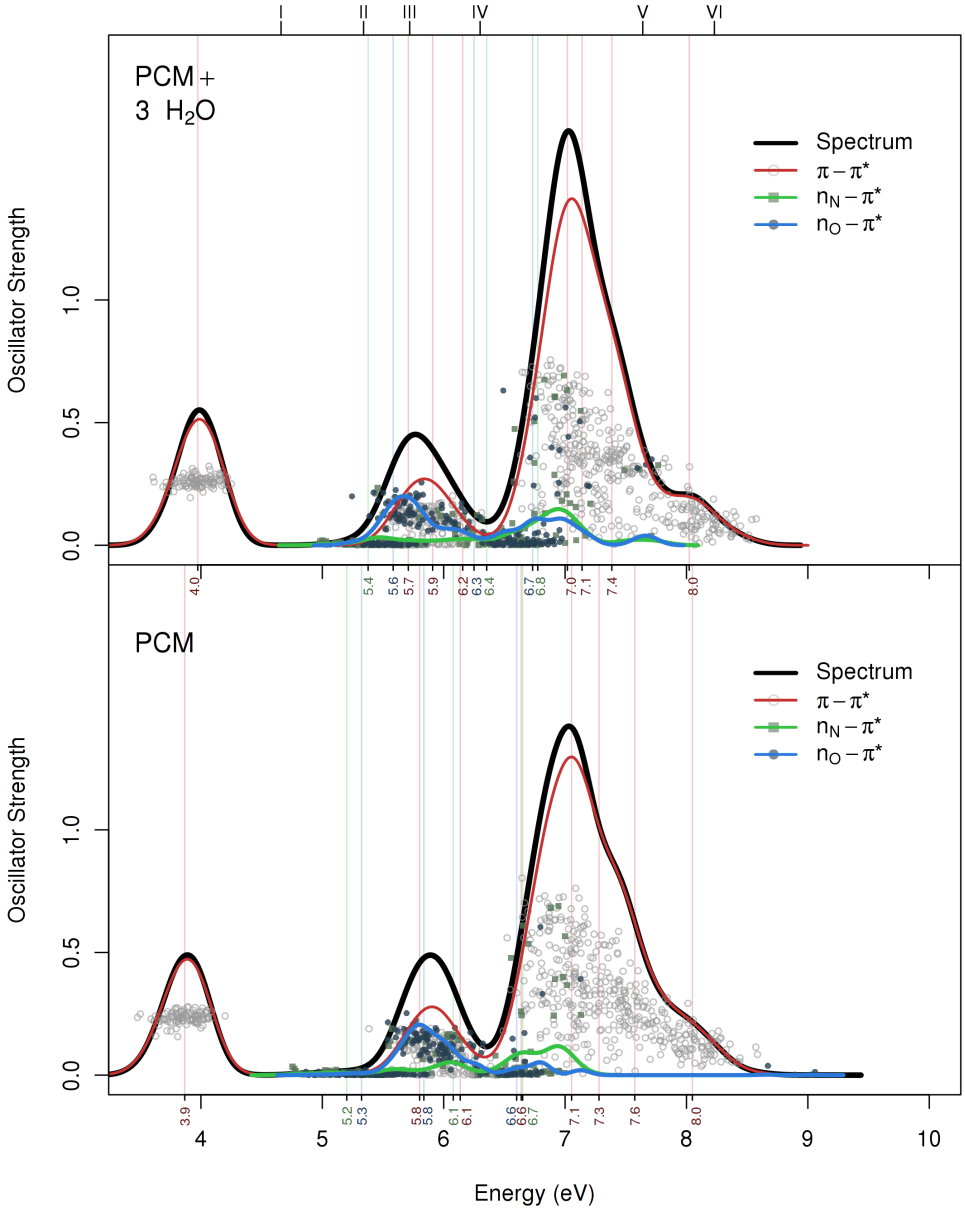

Figure 3.7: Computed absorption spectra of cytosine keto N3H tautomer. Result from 100 conformers using a PCM solvent model (bottom) and, additionally, with 3 explicit water molecules (top). Density estimation with Gaussian kernel functions ($bw = 0.12$ eV). Roman numbers on top mark the experimentally observed features [62].

of the solvent model employed. The inclusion of explicit water molecules in the calculations of this tautomer does not affect much its electronic structure. The $n\pi^*$ transitions are slightly blue shifted by ~ 0.3 eV while the $\pi\pi^*$ transitions are in general lowered by ~ 0.2 eV. Qualitatively, the main effect of treating the hydrogen bonds is a larger differentiation between the different types of transitions that form the second band of the spectrum and a small shrinking of the main absorption band. However, we do not observe a high increase in intensity of any $n\pi^*$ transition, as was the case for the keto N1H form; this is ascribed to the small amount of $n\pi^*$ excitations in the main $\pi\pi^*$ band region.

The first band on the spectrum of the keto N3H tautomer is formed solely by transitions of the $\pi\pi^*$ type. The second observed band shows a more complex structure, composed primarily by one $n_O\pi^*$ with relatively high intensity, mixed with two $\pi\pi^*$ transitions. On the red edge of the second band there is a $n_N\pi^*$ transition that does not contribute to the absorption. Similarly, in the optically inactive region between the second and third band there are dark transitions of all types. The high absorption band of this spectrum has a maximum plus two shoulders at higher energies of decreasing intensity, all these features are caused by intense $\pi\pi^*$ transitions.

Enol tautomer. Figure 3.8 shows the computed absorption spectra of the cytosine enol tautomer in water. The spectral analysis of this tautomeric form is simpler compared to the keto and imino forms. There are no $n_O\pi^*$ transitions and only one type of $n_N\pi^*$ can be considered because the lone pairs of the two N atoms are indistinguishable. Accordingly, six $\pi\pi^*$ and six $n_N\pi^*$ transitions are identified along all enol conformers. The inclusion of explicit water molecules produces small blue shifts on some $n_N\pi^*$ transitions and small red shifts of some $\pi\pi^*$, in line with the results of the previous tautomers. The largest effect is found in the third $\pi\pi^*$ transition at the beginning of the high absorption bands which forms a new visible band at 6.4 eV. Moreover, the $n_N\pi^*$ transitions located in regions of the spectrum with a large number of intense $\pi\pi^*$ transitions, like the second band at 5.5 eV and the two high absorption bands found between 6.5 and 8.0 eV, experience a significant gain of intensity upon inclusion of the water molecules in the CASPT2 calculation. Similarly to the other tautomers,

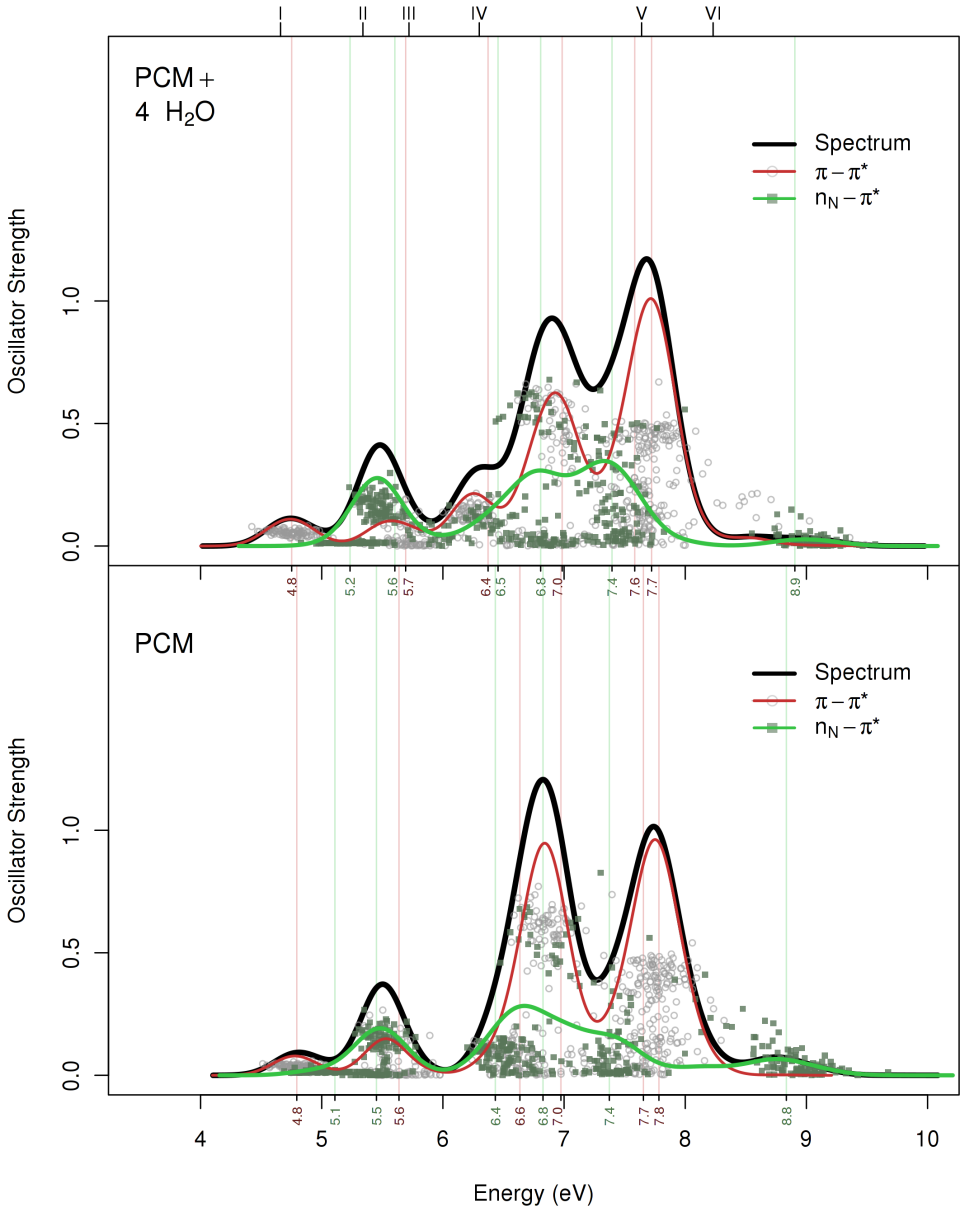

Figure 3.8: Computed absorption spectra of cytosine enol tautomer. Result from 100 conformers using a PCM solvent model (bottom) and, additionally, with 4 explicit water molecules (top). Density estimation with Gaussian kernel functions (bw = 0.14 eV). Roman numbers on top mark the experimentally observed features [62].

this phenomenon arises from an increase of the π character of these transitions, increasing the overlap between the ground state and the involved excited state.

The peaks of absorption of the enol tautomer spectrum are well defined and have contributions from few transitions, easing their assignments. The first and fifth absorption bands, at 4.8 eV and 7.7 eV respectively, can be assigned to pure $\pi\pi^*$ bands. Instead, the second band is caused primarily by $n_N\pi^*$ excitations. The complexity of this spectrum increases for the third and fourth bands, at 6.4 and 6.9 eV, which appear as a mix with similar weights of both types of transitions. Furthermore, there are some features which are masked in the spectrum. Located at 7.3 eV, in the valley between the two high absorption peaks of the fourth and fifth bands, there is a $n_N\pi^*$ band of lower intensity but optically active. The rest of transitions do not contribute to absorption, like the excitations found at ~ 9 eV.

Imino tautomer. Figure 3.9 shows the computed absorption spectra of the cytosine imino tautomer in water. We have identified eight $\pi\pi^*$, three $n_O\pi^*$ and three $n_N\pi^*$ transitions along all conformers. This tautomer shows the largest change upon addition of explicit water molecules in the solvent model. The basic morphology of the spectra is formed by three peaks of increasing intensity, which are present in both solvent models. However, the inclusion of water molecules to the imino tautomer forms a fourth band in the higher energy region of the spectra. This band appears by the concentration of $\pi\pi^*$ transitions that otherwise are found as a disperse cloud in the PCM spectrum. There is a relatively large blue shift of a $\pi\pi^*$ excitation from 7.1 eV in PCM to 8.0 eV including four waters. Moreover, there is also a red shift of another intense $\pi\pi^*$ transition from 8.9 to 8.5 eV. These intense absorptions are the main peak and shoulder of the fourth band. Additionally, the inclusion of water molecules to the imino form has two effects that we already observed in the other tautomers. The first one is the increase in absorption of some $n_O\pi^*$ excitations located in the most intense band, due to an increase of their π character that leads to a larger overlap between the involved states. The second one is a higher differentiation between the transitions that contribute to each absorption band, which in this case is observed along all the spectrum.

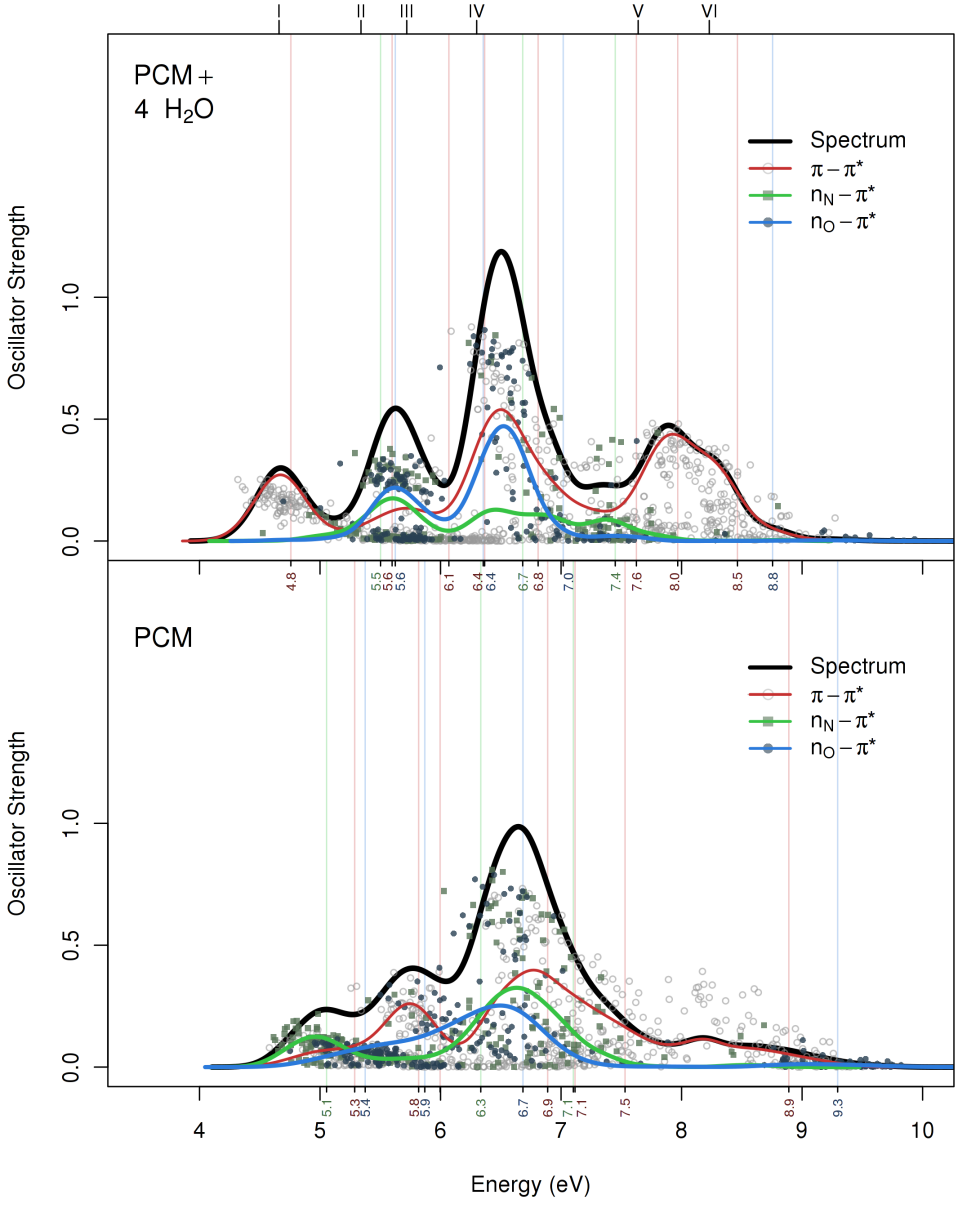

Figure 3.9: Computed absorption spectra of cytosine imino tautomer. Result from 100 conformers using a PCM solvent model (bottom) and, additionally, with 4 explicit water molecules (top). Density estimation with Gaussian kernel functions (bw = 0.14 eV). Roman numbers on top mark the experimentally observed features [62].

The first band on the absorption spectrum of the imino tautomer is a pure $\pi\pi^*$ band. However, the source of these excitations is not the π MO on the carbonyl group as for the two keto tautomers. Instead, they involve a π MO mainly localized on the amine group. These transitions are identified as $n_N\pi^*$ excitations in the spectrum without explicit water molecules. The hydrogen bonds formed with surrounding solvent molecules stabilize the lone pair in the N atom, increasing the $\pi\pi^*$ character of the lowest electronic excitations and pushing the first $n_N\pi^*$ transitions into the second absorption band. This band is formed by a mix of three transitions, each one of a different type, that contribute in the same proportion to the total absorption. Subsequently, an optically almost inactive $\pi\pi^*$ transition is identified at 6.1 eV. The third band is the most intense feature in the imino tautomer spectrum. One $\pi\pi^*$ and one $n_O\pi^*$ transitions are the main excitations behind this band. Additionally, there is a weak $\pi\pi^*$ transition that produces a shoulder on the end of the third band. There are two dark transitions masked by the intense absorption, a $n_N\pi^*$ at 6.7 eV and a $n_O\pi^*$ at 7.0 eV. Furthermore, a small peak appears in the valley between the third and fourth band caused by a $n_N\pi^*$ transition at 7.4 eV. The high end of the spectrum shows a low absorption produced by a $n_O\pi^*$ transition.

3.4 Conclusions

We have successfully combined the Car-Parrinello MD method with CASPT2 calculations to describe the absorption spectrum of four cytosine tautomers (Figure 3.1). We explored the conformational space of these tautomeric forms in water, extracted a representative sample of 100 conformers for each tautomer and studied their electronic structure with an efficient treatment of electron correlation. The wave function based calculations included the solvent effects through a PCM for water and some additional explicit water molecules. From the resulting data set we built the spectrum of each tautomer and analysed their underlying structure.

The computed absorption spectrum of the keto N1H tautomer has a very good agreement with previous experimental data (Figure 3.5). The combination of

Car-Parrinello MD and CASPT2 generates a theoretical spectrum of cytosine that not only reproduces the energetics, but also the bandwidths and intensities of the spectral features. The analysis of the calculated excitations makes possible to identify them by their characteristics and describe the different individual contributions to the spectrum. The six observed transitions in the experimental spectrum are formed by a total of fifteen transitions, which are grouped arising the six experimental absorptions. The difference in energy between the calculated and the experimental bands is very low, of the order of 0.1 eV. A comparison with the LoProp population of the O and N atoms with lone electron pairs proved the classification of the different transition contributing to the spectrum to be correct (Figure 3.6). Additionally, following the same procedure performed on the keto N1H tautomer, we computed and analysed the absorption spectra of the other three tautomers (Figures 3.7, 3.8 and 3.9). All of them show similar characteristics to the keto N1H tautomer but with significant differences on their spectrum composition.

The results obtained confirm the complexity of studying the cytosine molecule. Even though it is a relatively small molecule, its flexibility and tautomerization phenomena impose the use of dynamical techniques to cover vibro-rotational degrees of freedom that are not accessible from static approaches. Moreover, the increased complexity also affects the electronic structure and its analysis. Each tautomer shows different electronic properties which require an individualized study of them. The absorption spectra are formed by various transition types, which we classified in $n_O\pi^*$, $n_N\pi^*$ and $\pi\pi^*$ excitations. These archetypical transitions can mix due to the conformational distortions that break the planar symmetry of the ideal cytosine molecule.

The effect on the absorption spectrum of the hydrogen bonds between cytosine and solvent molecules is to shift both $n\pi^*$ and $\pi\pi^*$ transitions. However, there is not a clear trend on the change produced to the absorption energies. The $n\pi^*$ transitions are usually blue shifted but the effect on $\pi\pi^*$ transitions is very variable. We observe that the hydrogen bonds combined with the structural distortions of the conformer can favour even more the mix between excitations involving a non-bonding MO with those involving a π MO. Some $n\pi^*$ excitations

experience a large increase of intensity due to their increased π character. This behaviour shows that once the conformational distortions are incorporated into the theoretical model it is no longer possible to get pure transitions of one single type. Thus, there is no simple description of the electronic structure of cytosine, even though its molecular structure and absorption spectra can look simple.

CHAPTER 4

Ab initio absorption spectrum of NiO combining molecular dynamics with the embedded cluster approach in a direct reaction field

4.1 Introduction

Nickel oxide is a prototype transition-metal oxide with a relatively simple crystalline structure but complex electric and magnetic properties. Understanding the electronic structure of this basic material is an important step to achieve a better knowledge about more sophisticated systems like superconducting oxides and manganites with magneto-resistance. NiO has a rocksalt lattice structure in its paramagnetic phase, whereas below the Néel temperature (T_N=523 K) the antiferromagnetic ordering induces a slight rhombohedral distortion of the crystal structure [118] with a small increase of the angle between the lattice vectors of 0.100° [119]. In both phases NiO behaves as an electric insulator whose conductivity increases as temperature raises [120] and remains insulating up to pressures on the order of 1 Mbar [121–123].

The clear non-conductivity observed in NiO is in contradiction to what can be expected from simple arguments regarding the partially filled 3d band. Various spectroscopical techniques have been employed since the 1950s to study the electronic structure of NiO and understand the nature of its non-conductivity. The most widely used techniques have been based on photoabsorption spectroscopy or the combination of photoemission with inverse-photoemission spectroscopy. These studies invariably showed that there is an energy gap between the insulating electronic ground state of the system and the lowest conducting excited states. This gap is the source of non-conductivity in NiO and is measured to be ~ 4 eV. However, the interpretation offered by those studies about the nature of the conductivity gap in NiO is diverse and not conclusive. Each technique measures different electronic processes which causes the analysis to be dependent on the type of spectroscopy employed, even though they coincide in the measure of the conductivity gap. The difficulty in encountering a satisfactory and univocal explanation of the insulating behaviour of NiO is directly related to the complexity of its electronic structure that can be observed from the spectroscopic data available.

Ultraviolet-Visible Absorption Spectroscopy (UAS) offers direct measurements of electronic transition energies. The UAS spectrum of NiO shows a high ab-

sorption plateau above ~ 4 eV and some features with low optical activity below it [37]. The high absorption plateau extends constantly to 8 eV with some signals appearing along it [124]. Thus, the optical gap in NiO can be defined as the optically almost inactive region below the absorption edge at ~ 4 eV. The signals observed below the optical gap are very similar to the spectrum of Ni:MgO [125]. Therefore, these weak absorptions are assigned to dipole-forbidden intra-atomic Ni d–d transitions [37] revealing the high localization of Ni(3d) orbitals on the Ni site [124]. The Ni^{2+} cation can be considered in an octahedral coordination environment with six O^{2-} anions where the crystal-field strength ($10Dq$) splits the Ni(3d) orbitals in e_g and t_{2g} molecular orbitals (MO). The ground state of the Ni^{2+} ion in this octahedral environment is a ${}^3A_{2g}(t_{2g}^6 e_g^2)$ and the lowest d–d excited states have configurations of the form $(t_{2g}^5 e_g^3)$. The electron-hole pair formed by these d–d transitions is a so-called Frenkel exciton localized on the Ni atom and does not contribute to conductivity.

Early interpretations of the nature of the absorption edge at ~ 4 eV were more differing than the assignments of the weak features in the optical gap [37, 124, 126]. The Resonant Raman Scattering experiments by Merlin and collaborators for NiO [127, 128] gave an empirical proof pointing towards a ligand to metal charge transfer (LMCT), from the ligand O(2p) to metal Ni(3d) orbitals, as the source of the absorption band. However, it is not clear if this charge transfer process is a localized $d^8 \rightarrow d^9\underline{L}$ transition (here $\underline{L}$ means a hole in the ligand) or an itinerant inter-site $d^8 + d^8 \rightarrow d^8\underline{L} + d^9$ transition, with no interaction between electron and hole. Evidence of photoconductivity slightly above the optical gap indicates the presence of free carriers in the system as a result of the absorption process [126, 129]. Since the electrons in the localized Ni(3d) orbitals will be trapped, the only available carriers formed by the LMCT are the holes in the ligand O(2p) orbitals which by hopping can produce polaronic conductivity. Hence, this observation points towards an inter-site LMCT as the source of the high absorption plateau. Nevertheless, the fact that photoconductivity appears slightly above the optical gap indicates that there are some excitonic effects involved in the absorption process which point to a localized intra-site LMCT instead, where the electron-hole pair will be moderately trapped at the site of

absorption. Therefore, the conductivity gap of NiO should be slightly larger than the observed optical gap.

Photoemission spectroscopy (PES) measures the binding energy of valence electrons revealing the valence density of states (DOS) in relation to the Fermi level (E_f). The X-ray Photoemission Spectroscopy (XPS) [130], Resonant XPS [131, 132] and Angle-Resolved XPS [133, 134] have been used to study the valence electronic structure of NiO. Furthermore, Inverse PES (IPES) measures the binding energy of electrons in the lowest unoccupied levels, allowing the study of conducting bands and complementing PES data. Thus, the PES/IPES combination provides the complete DOS that covers both valence and conducting levels of the system. The XPS combined with Bremsstrahlung-Isochromat Spectroscopy (BIS) shows a gap between the top of the valence band and the bottom of the conducting band of 4.3 eV for NiO [129]. It must be noted that the exact value of this conductivity gap is subject to the band position chosen to define the highest valence and lowest conducting levels, obtaining values that range from 3.20 to 5.67 eV [135]. The experimental results show that the lowest conduction band has mainly d^9 character and the upper part of the valence band has contributions from both d^7 and $d^8\underline{L}$ levels. Nowadays it is widely accepted that NiO is a charge-transfer insulator with a final $d^8\underline{L} + d^9$ state because the $d^8\underline{L}$ levels are found at slightly lower binding energies than the d^7 levels.

However, the descriptions of the nature of the conductivity gap present many subtle differences regarding the degree of localization of the transitions involved [135] and the contribution and hybridization of the Ni(3d) and O(2p) levels in the valence band. Moreover, the indirect measure of the electronic levels offered by PES/IPES techniques are inherently delocalized, giving no information on local transitions which could be important to get the complete picture of the electronic structure of NiO. A study with Site-Specific X-ray Photoelectron Spectroscopy (SSXPS) localized on Ni and O sites showed that the top of the valence band has a higher O(2p)–Ni(3d) mixing than previously thought [136] and the comparison of these techniques with X-ray Absorption Spectroscopy (XAS) proved that this kind of data obtained for the valence band is dependent

on the methodology applied [137]. Furthermore, all these spectroscopic methods produce core-holes in the sample during the measure and these hole levels could be not completely innocent, requiring a sophisticated theoretical model to interpret the experimental results [138–140].

An ongoing challenge during the last 60 years has been the development of a theoretical model that could offer an accurate description of both the electric and magnetic phenomena observed on NiO. An early model based on band theory capable of explaining the non-conductivity of late transition-metal oxides is the Mott-Hubbard insulator concept [141–143]. The source of the conductivity gap in this model is the large electron correlation in NiO, which is caused by the high localization of 3d states on Ni sites and generates a large on-site Coulomb interaction (U) for the electrons in the 3d orbitals. This large U opens a gap in the metal 3d band between the occupied and unoccupied 3d levels, or the so-called lower and upper Hubbard bands, making the system non-conducting [126, 144–146]. U is defined as the energy of the inter-site $d^8 + d^8 \rightarrow d^7 + d^9$ process which makes PES/IPES techniques very convenient to measure it. However, as shown by the spectroscopic data, LMCT processes also play an important role in NiO. The incorporation of the charge transfer energy (Δ) into the theoretical model was performed by Zaanen *et al.* [147], who also defined the ratio U/Δ as a parameter to classify the source of non-conductivity in different materials. According to this model NiO is an intermediate insulator with U and Δ on the same order of magnitude. This behaviour makes U and Δ difficult to measure experimentally due to the hybridization between Ni(3d) and O(2p) states. Therefore, much theoretical research has been performed in the last decades to obtain accurate estimates of these parameters.

Density Functional Theory (DFT) calculations with the Local-Density Approximation (LDA) functional applied to a periodic model of the system is known to be a solid approach to the description of Bloch itinerant states in metallic systems. However, the band gap values obtained with LDA are clearly underestimated for NiO ($\sim$ 0.5 eV) [148] and other ionic insulators. The latter is a consequence of the shortcomings of LDA to correctly treat the electron correlation and properly describe the localized Ni(3d) states in the vicinity of

E_f. Subsequent improvements over the LDA functional offered more accurate methods to describe highly correlated materials. Some examples are the Self-Interaction Correction (SIC-LDA) [149], the Dynamical Mean Field Theory taking into account many-body effects [150], treating local states with Wannier functions [151] or by means of hybrid DFT functionals [152]. Other approaches add explicitly the on-site Coulomb interaction through various implementations of LDA+U [153, 154] and, additionally, the electron correlation can also be accounted for through Green's functions (GW) [155, 156]. The DOS of NiO calculated with a recent application of GW@LDA+U is in very good agreement with experimental PES/IPES data, obtaining gaps for $\Delta = 3.75$ eV and $U = 5.2$ eV [157], which enforces the description of NiO having $\Delta \approx U$ but being a charge transfer insulator. An important drawback of the LDA+U method is that it requires U as a starting parameter which can be either estimated from experimental data or calculated specifically with some external method like the constrained DFT formalism [158].

An alternative to the periodic calculations is the embedded cluster approach. The model of the system defined by this approach is composed by few atoms that form the active site of the material (cluster) which is immersed into a finite approximation of its environment (embedding). Hence, the cluster can be described "all-electron" by a wave function based method capable to treat the strong electron correlation found in systems like NiO, without any *a priori* assumption about the effect of correlation on the electronic structure. On the other hand, the embedding can be formed by a combination of *Ab Initio* Model-Potentials (AIMP) [159] with a point charge distribution in order to reproduce the long range electrostatic interactions. Albeit this approach is not able to deal with delocalized states like the Bloch states of periodic systems, in highly correlated materials it has proven very accurate in the description of the ground and excited states where the localized Ni(3d) states play an important role [160, 161]. Fujimori *et al.* [162] gave a reinterpretation of the PES/IPES spectrum based on parametrized Configuration Interaction (CI) calculations on a NiO_6^{10-} cluster pointing to the charge transfer as the source of the conductivity gap in NiO. They also obtained d–d transitions in good agreement with the

UAS data but slightly overestimated LMCT energies (7 – 8 eV). Furthermore, a Multi-Reference CI (MR-CI) based method applied to a NiO_6^{10-} cluster [163] resulted in better values for the LMCT process (6.2 eV). Ionization and electron affinity calculations were also performed using a NiO_6^{9-} and a NiO_6^{11-} cluster respectively, which resulted in estimations of $U = 11.6$ eV and $\Delta = 10.3$ eV. These results were further improved in the same study by including semi-empirical corrections to the correlation energy and bulk polarization effects through the Discrete (or Direct) Reaction Field (DRF) method obtaining values in better agreement with the experimental band gap, $\Delta = 4.4$ eV and $U = 4.6$ eV.

The aim of the present work is to continue developing the *ab initio* approach offered by the embedded cluster model and provide a more complete description of the electronic structure of NiO. By combining *ab initio* molecular dynamics (MD) simulations with highly correlated electronic structure wave function calculations we obtain not only the transition energies of local excitations but also their intensities and bandwidths. We use Car-Parrinello MD to explore the vibrational degrees of freedom of the ground state potential energy surface of NiO. Subsequently, we calculate the electronic structure in a representative sample of the simulation with the Complete Active Space Self-Consistent Field Second-Order Perturbation theory (CASPT2) which has proven very efficient in treating both the static and dynamic electron correlation on transition-metal compounds [39, 164, 165]. Moreover, the embedded cluster model has been improved in comparison to previous studies by a self-consistent incorporation of the aforementioned DRF method to take into account the extra cluster polarization produced by the electronic excitations. We give estimations of the low energy region of the UAS spectrum of NiO, including d–d transitions and LMCT processes, and of its DOS nearby E_f, from which we extract the U and Δ parameters, and compare the results obtained with a static embedding and the DRF approach.

4.2 Computational Scheme

The proposed *ab initio* procedure to study the electronic structure combines Car-Parrinello MD [102] simulations at a given temperature with the highly efficient treatment of electron correlation and excited states offered by the CASPT2 method [32, 34]. Car-Parrinello MD explores the classically allowed vibrational levels accessible in the electronic ground state and CASPT2 calculates the vertical electronic excitations in a limited number of snapshots of the simulation. Hence, the effect of the movement of the ions on the electronic structure can now be incorporated. The extraction of these conformational structures from the MD trajectory is not trivial because it requires the transformation of the employed material model; from the periodic description of the molecular dynamics to the embedded cluster model of the electronic structure calculations. The extraction step was automated by a tool developed with FORTRAN95 specifically for this purpose. This algorithm selects multiple distorted structures from the simulation using as reference the ideal structure of the cluster and performs the required transformations on the model.

Furthermore, it is important to consider extra-cluster polarization effects induced by the electronic excitations considered, which can produce large electronic distortions on the cluster and were shown to have a significant role on NiO [163]. Hence, once the clusters are generated, the polarization of the embedding is incorporated in a self-consistent scheme that has been developed integrating the DRF method [166–168] with the electronic structure calculations.

Combination of Car-Parrinello MD with CASPT2

The simulation box in the Car-Parrinello MD consisted of a NiO supercell of 15.7372 bohr side length, which is equivalent to a 2x2x2 crystallographic unit cell and contains 32 Ni atoms and 32 O atoms. The core electrons are described by Troullier-Martins normconserving pseudo-potentials [104] and, in the case of Ni,

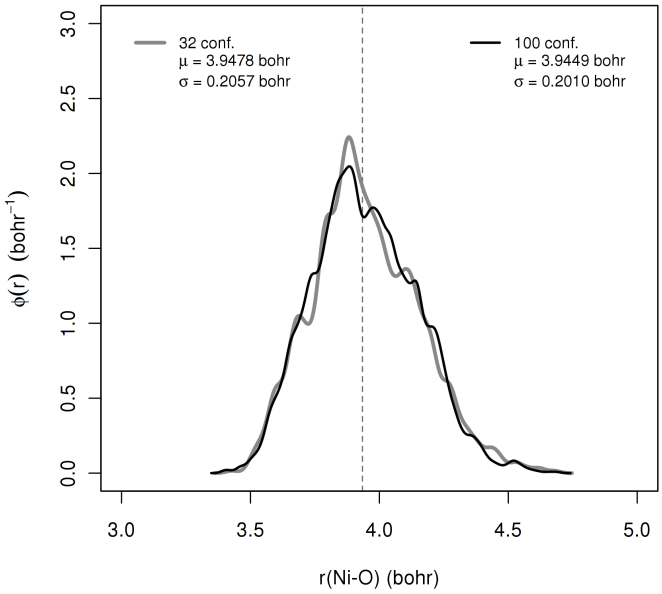

Figure 4.1: Thermal distributions of Ni–O bond lengths resulting from the Car-Parrinello MD simulation at 300 K for the 32 conformations set (grey) and the 100 conformations set (black). The dashed line indicates the Ni–O bond length (3.9343 bohr) derived from X-ray diffraction [169].

non-linear core corrections were added. The electronic potential was calculated by means of the BLYP density functional [105, 106] using a plane waves basis set with a cut-off of 80 Ry. The system was equilibrated at 300 K and then maintained at a steady temperature with a Nosé-Hoover chain thermostat [107, 108]. The simulation was performed in time steps of 0.096 fs with a fictitious electron mass $\mu = 700$ a.u. Finally, the conformational structures were extracted from a trajectory of 2 ps. This MD simulation was carried out with the CPMD software version 3.11.1.

The number of extracted conformations varied depending on the type of calculation performed on them. The main factor in choosing the size of the set of conformations is the computational cost of the subsequent electronic structure calculations to be performed on each structure. The simpler calculations of

small clusters in a static embedding were performed over a set of 100 conformations, but the more complex calculations of bigger clusters obliged us to use a smaller set of 32 conformations. To check the sample's representativeness of the simulation, the thermal distribution of Ni–O bond lengths of the two sets is compared in Figure 4.1. The close resemblance of the two density curves shows that both sets used in this work can be considered effectively equivalent in terms of simulation sampling.

The embedded cluster model of each conformation was built from a single supercell equivalent to a 10x10x10 NiO crystallographic unit cell with a total of 8000 atoms, which was formed by replication of one of the simulation supercells extracted from the trajectory. Three different clusters of increasing size and their embeddings were constructed: *i*) NiO_6 cluster + 6 Ni-AIMP(1s,1p) + 2184 point charges; *ii*) NiO_{14} cluster + 42 Ni-AIMP(1s,1p) + 2140 point charges; *iii*) NiO_{38} cluster + 78 Ni-AIMP(0s) + 2080 point charges. Figure 4.2 shows a graphical representation of the structure of these clusters. The smallest cluster is formed by a central Ni atom surrounded by the first shell of six O atoms in a pseudo-octahedral environment. Then this cluster is further expanded with the second and third O shells to better describe the surroundings of the active site. The electrons of the Ni ions in the cluster region, except for the central Ni atom, are described by model potentials to avoid an artificial delocalization of the electron density towards the positive charges and because, additionally, their explicit inclusion in the *ab initio* wave function would lead to a computational problem of unmanageable size. The point charges around the cluster form a cube of $\sim$ 47 bohr side length with the charges placed on lattice positions. The charge values were set by the Evjen's method [170] where the inner point charges have the corresponding formal charge for Ni^{2+} and O^{2-} ions and the charges on the outside of the cube have fractional charges to ensure the overall charge neutrality. This way of representing transition metal oxides has been extensively used and proven to accurately model the crystal for the description of local electronic structure properties [171–175].

The basis sets used throughout the electronic structure calculations of all clusters are of the atomic natural orbitals type including scalar relativistic effects

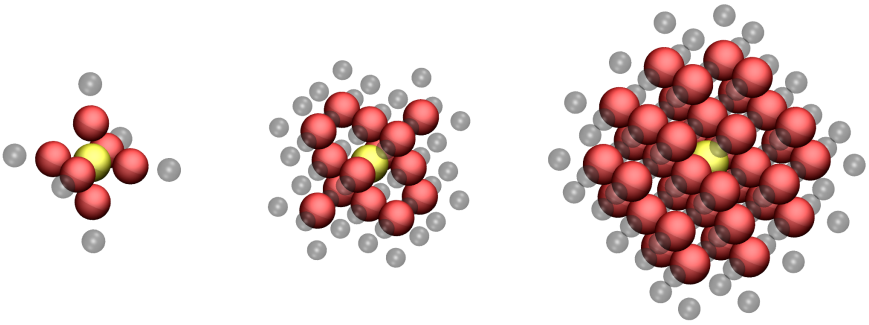

Figure 4.2: Structure of the three cluster models of NiO. From left to right they are NiO_6, NiO_{14} and NiO_{38}. The central Ni atom is represented in yellow, O atoms in the cluster are in red and the smaller transparent grey spheres represent Ni-AIMP.

(ANO-RCC). The contracted basis functions for Ni were (5s,4p,2d,1f) [46] and for the O atoms were (3s,2p,1d) [45]. These basis sets were chosen as a balance between computational cost and flexibility to describe electron correlation and polarization phenomena in the cluster. The reference wave function of the CASPT2 calculation is constructed following the Complete Active Space Self-Consistent Field (CASSCF) approach, which provides an unbiased treatment of the different electronic configurations that play a role in the total electronic structure of the cluster. The multi-configurational CASSCF wave function is obtained by distributing a limited number of valence electrons over a set of valence orbitals in all possible ways. In the present case the so-called complete active space (CAS) contains 10 electrons and 11 orbitals, in short CAS(10,11). After the orbital optimization procedure, the active orbitals can be identified as five Ni–3d orbitals, five more diffuse Ni–d orbitals in the so-called 3d' shell [39], and one O–2p orbital. This active space offers a solid footing to describe the electronic ground state of NiO [50] and the excited states arising from internal Ni d–d excitations and from the lowest LMCT excitations. The so-obtained zero-order wave function is further improved by the aforementioned CASPT2 approach, a second-order perturbation treatment of the remaining dynamic elec-

tron correlation. We performed the CASPT2 calculations with a shift factor of 0.10 a.u. [113], which we previously tested to be the minimum value to eliminate possible intruder states.

The intensity of the considered electronic transitions was computed by State Interaction calculations between the ground state and all the excited states at the CASPT2 level, replacing the Hamiltonian by the transition dipole operator [114]. The electronic structure calculations were carried out with the MOLCAS 7.2 package [48, 49]. The resulting data set of electronic transitions was statistically treated with the R package [115] to generate the corresponding spectra or DOS. For this purpose we have employed a kernel density estimation with Gaussian kernel functions with a variable bandwidth (bw) depending on the length of the data set.

Self-Consistent DRF

The electronic excitations like the local d–d transitions do not change substantially the electronic density on the site of absorption. Therefore, the polarization on the rest of the crystal in response to such excitation is expected to be small. However, this is no longer the case for LMCT states and even less for ionization and electron addition states, which produce a larger electronic change in the atoms directly involved in the excitation and will induce a major response in the surroundings of that site. The adaptation of the extra-cluster region to the changes of electron density in the cluster will be first electronic and later structural, forming a polaron. The static embedding used so far in the model of NiO is not capable to deal with this situation. To overcome this limitation we apply the DRF method, which offers a rigorous treatment of the electric response of the embedding through the inclusion of a set of dipole polarizabilities and which can be combined with the quantum description of the cluster.

Even though the DRF method was already applied to NiO successfully [163], we present here for the first time an integration of DRF with CASSCF calculations in a self-consistent manner for highly excited states using the embedded

cluster model. In the first step of the developed procedure, the electronic density of the cluster is computed in a static embedding and used to generate the corresponding induced extra-cluster polarization through DRF. The polarized embedding is formed by the same AIMPs and point charges of the static embedding but adding induced electric dipoles on the lattice sites around the cluster. The CASSCF step is then rerun with the DRF polarized embedding to produce a new electronic density and the process is repeated until the energy of the excited state of interest remains constant. However, there are two main issues with this basic design. The first one is that the electronic density used by the DRF method should be the one from the electronic state that causes the perturbation in the system. For example, the inclusion of the relaxation due to the LMCT process requires the calculation of the electronic density of the 11^{th} excited state (the first ten states are d^8 spin-triplet states). Unfortunately, state specific CASSCF calculations for such high states do not converge and, thus, we are forced to work with state average calculations from which the state specific response cannot be extracted directly. Nevertheless, it is possible to get closer to the state specific situation by changing the weight of the states in the average. We observed that the induced dipoles vary linearly with respect to the weight of the LMCT state in the state average CASSCF procedure (Figure 4.3). This behaviour is observed in several conformations and over a wide range of weights. Therefore, under the hypothesis that the linear behaviour is maintained along the complete range of LMCT weights, it is possible to obtain the polarization in the embedding caused by the LMCT state through linear extrapolation.

The second issue finds its origin in the fact that the cluster model lacks the translational symmetry found in the crystalline material. The isolation of the active site and its surroundings in an infinite void causes the DRF embedding to be highly polarized even in the ground state. This behaviour has no physical basis because, from a global view of the material in its ground state, the electronic density on one site is equivalent to its neighbouring sites and no polarization should occur. In order to study the physically meaningful electronic transition between the ground state and the LMCT state in its polarized embedding, we first generate an "artificial" DRF embedding for the ground state and subtract

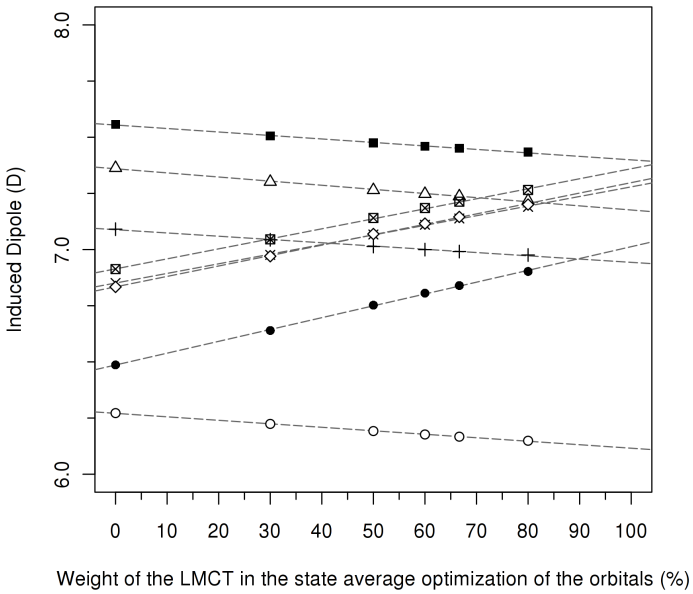

Figure 4.3: Variation of 8 induced dipoles of an arbitrary conformation with respect to the increase of LMCT weight in a state average including the ground state. The dipoles shown are the ones which suffer the largest change with the increase of LMCT weight. The dashed lines represent the linear adjustment performed on each dipole with the following linear regression coefficients: $R^2_{\circ} = 0.9991$; $R^2_{\triangle} = 0.9959$; $R^2_{\bullet} = 0.9994$; $R^2_{\times} = 0.9995$; $R^2_{\diamond} = 0.9994$; $R^2_{\blacksquare} = 0.9969$; $R^2_{\boxtimes} = 0.9993$; $R^2_{+} = 0.9969$.

it from the DRF embedding induced by the LMCT. With this procedure we obtain a polarized embedding with contributions exclusively from the charge transfer process.

The last step consists of the State Interaction calculation at the CASPT2 level between the ground state in the non-polarized embedding and the LMCT state in its polarized embedding to obtain the corresponding transition energies and intensities. This step requires to compute the LMCT state of the system including the DRF embedding previously generated. However, as shown before, it is in general not possible to perform the CASSCF state specific calculations of these excited states. Therefore, we perform once again a state average CASSCF

calculation including the LMCT state and the ground state but this time with the polarized embedding by the LMCT. Nevertheless, for one conformation, we were able to converge the wave function for the LMCT state alone. The final result is nearly identical to the one obtained using a state average reference wave function, less than 0.2 eV difference in the energy of the LMCT state.

In the case of ionized ($d^8\underline{L}$ and d^7) and electron addition (d^9) states the procedure is exactly the same but without the difficulties inherent to the treatment of the LMCT states. All these states are the lowest states with different spin multiplicities and, hence, they can be calculated separately by state specific CASSCF calculations.

The DRF method requires to define the atomic polarizability of each atom in the system. We set $\alpha_{O^{2-}} = 1.988$ Å^3 [176] for the O atoms and $\alpha_{Ni^{2+}} = 0.653$ Å^3 for the Ni atoms, based on the total polarizability of NiO ($\alpha_{NiO} = 2.641$ Å^3 [124]). The DRF calculations were performed with the DRF90 software [177].

4.3 Results

Static Non-Polarized Embedding

Optical Absorption: Figure 4.4 shows the computed UAS spectrum of NiO at 300 K. This spectrum is formed by electronic transitions of 100 conformations modelled with a NiO_6 cluster in a static non-polarized embedding. For each structure we performed a state average CASSCF/CASPT2 calculation of the lowest 12 triplet electronic states and another state average calculation of the lowest 17 singlet states. Although there is no symmetry in the analysed distorted structures, we will use the term symbols of the O_h symmetry group to facilitate the discussion and the comparison with previous studies. Due to the conformational distortions, the electronic transitions from the triplet $^3A_{2g}$ ground state are no longer forbidden by the dipole selection rule and, therefore,

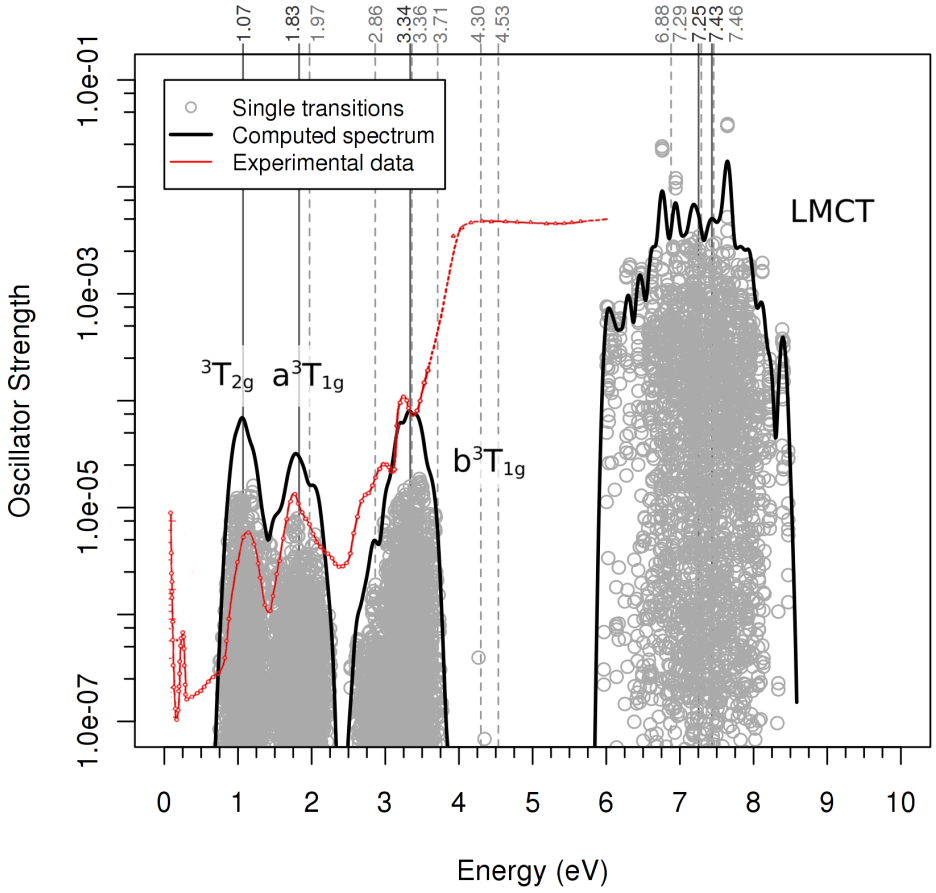

Figure 4.4: Absorption spectrum of NiO at 300 K obtained from 100 conformations modelled by NiO_6 clusters with a static embedding (black) and the experimental spectrum (red) [37]. The circles mark single electronic transitions from the ground state. The average energy of the absorption bands is noted on the upper part of the graph and in Table 4.1. Density estimation with Gaussian kernel functions ($bw = 0.038$ eV).

Table 4.1: Average CASPT2 energies of the Ni–$3d^8$ and the lowest LMCT states in NiO obtained from 100 conformations modelled with a NiO_6 cluster in a static non-polarized embedding. The results provided are the mean energy ($\overline{E}$) and the standard deviation (σ) of the absorption bands. Experimental data is also shown for comparison.

	Exp.[a]	Present work		
State	E (eV)	C_1 $\overline{E}$ (eV)	O_h $\overline{E}$ (eV)	O_h σ (eV)
$^3A_{2g}$	0.00	0.00	0.00	
$^3T_{2g}$	1.13	0.98 1.06 1.16	1.07	0.13
a^3T_{1g}	1.95	1.70 1.85 1.93	1.83	0.18
a^1E_g	1.75	1.95 1.99	1.97	0.06
a^1T_{2g}	2.75	2.78 2.85 2.95	2.86	0.12
b^3T_{1g}	2.95	3.21 3.33 3.46	3.34	0.16
a^1A_{1g}	3.25	3.36	3.36	0.06
$^1T_{1g}$	3.52	3.61 3.82 3.89	3.71	0.16
b^1E_g		4.33 4.27	4.30	0.12
b^1T_{2g}		4.50 4.53 4.56	4.53	0.13
b^1A_{1g}		6.88	6.88	0.35
a^3LMCT	~ 4	7.25	7.25	0.50
b^3LMCT		7.43	7.43	0.47
a^1LMCT		7.29	7.29	0.43
b^1LMCT		7.46	7.46	0.40

[a] Newman and Chrenko [37]

it is possible to compute their intensity. Moreover, by including the spin-orbit coupling, we could also take into account spin-forbidden transitions to singlet excited states, which are less intense but nevertheless do significantly contribute to the final spectrum. The combination of all the electronic transitions from the 100 conformations, 14431 in total, was performed by means of a density estimation using Gaussian kernel functions with a minimal bandwidth of 0.038 eV. From this density estimate the UAS spectrum bands of NiO appear naturally.

The energy distribution of the calculated triplet and singlet excited states is detailed in Table 4.1. A comparison with the experimental spectrum reveals good agreement of the computed spectrum in the region below 4 eV, where energetics, intensities and bandwidths of the d–d bands are accurately reproduced. The

three spin-allowed transitions from the ground state $^3A_{2g}$ to the excited states $^3T_{2g}$, a^3T_{1g} and b^3T_{1g} are the origin of the three main bands on this region of the spectrum. The remaining features below 4 eV are spin-forbidden transitions to singlet excited states. Although the overall agreement with previous data is good, the results suggest that some of the assignments in the spectrum should be reconsidered. Most notably are the three features found in the third d–d band (2.5 – 4.0 eV), where the first signal at 2.75 eV can indeed be attributed to the $^3A_{2g} \rightarrow a^1T_{2g}$ excitation, but the other 2 features at 2.95 eV and 3.25 eV both belong to transitions to the different non-degenerate components of the b^3T_{1g} state. The excitations to the a^1A_{1g} and a^1T_{1g} states that also appear in this zone are completely masked by the triplet band. Figure 4.5 decomposes the d–d region of the global UAS NiO spectrum in the contributions of each single band and shows how the transitions to a^1E_g and a^1T_{2g} states appear as weak shoulders on the a^3T_{1g} and b^3T_{1g} bands, respectively.

On the other hand, the high absorption plateau extending over 4 eV is clearly overestimated by $\sim$ 2 eV. This band is mainly formed by dipole and spin-allowed LMCT processes where an electron is transferred from an O(2p) orbital to a 3d(e_g)–like orbital on Ni. Hidden in this band there are also less intense spin-forbidden LMCT and higher d–d transitions. The large overestimation of the LMCT band is produced by the shortcomings of the NiO_6 cluster employed. This small cluster combined with a static non-polarized embedding is not well suited to properly describe the charge transfer process which will polarize the surroundings to some extent. Nevertheless, the relative intensity between the optically weak d–d transitions and the dipole-allowed LMCT processes is correctly reproduced. The increase in intensity among the d–d bands observed in the experimental spectrum, but not found in the computed spectrum, is due to a background signal of raising intensity seen below 4 eV. This signal is caused by impurities in the sample analysed in the original experiment [37], but not treated in our model.

Conduction Band Gap: We applied a similar approach to describe the band gap of NiO. We increased the model size in this case because the involved cationic and anionic states produce large electronic distortions in the system. As a first

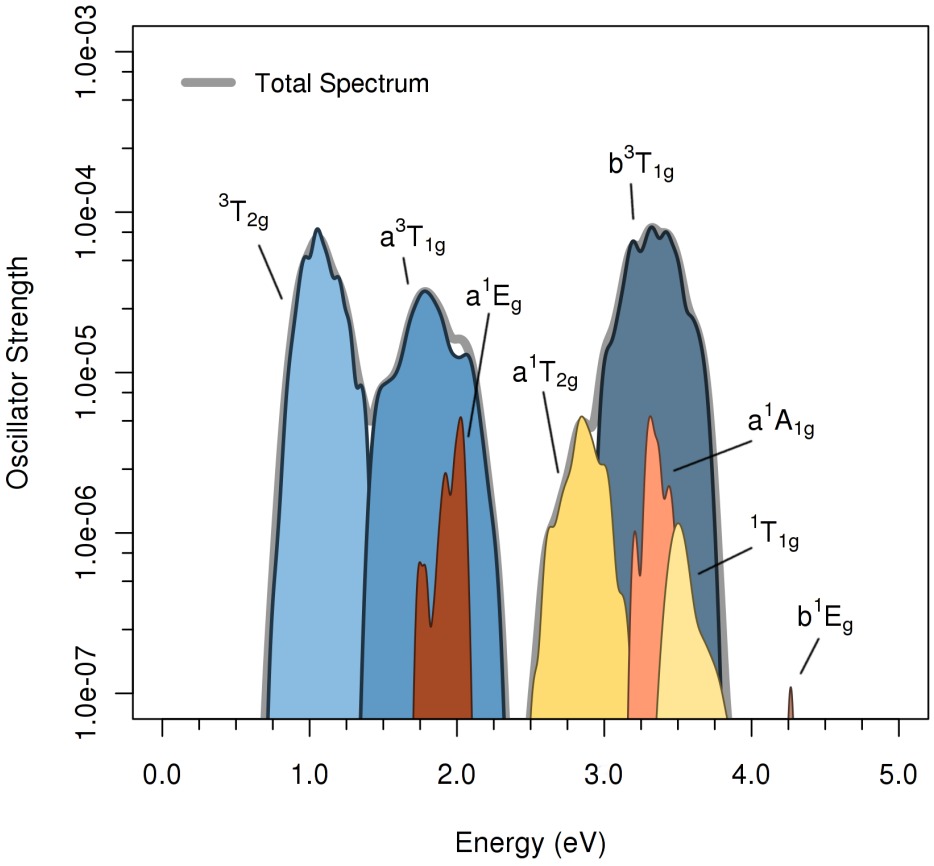

Figure 4.5: Breakdown of the absorption spectrum of NiO into its contributing bands at the d–d region. Density estimation with Gaussian kernel functions ($bw = 0.038$ eV).

step, we used a NiO_{14} cluster with a static non-polarized embedding and the smaller set of 32 conformations due to the increased computational cost. For each conformation we calculated the lowest anionic doublet ($^2A^{n+1}$), neutral triplet ($^3A^n_{2g}$) and cationic quartet ($^4A^{n-1}$) states, which are the ground states of their respective electronic configurations [178]. Furthermore, these anionic, neutral and cationic ground states were calculated using two different active spaces: one with Ni(3d,3d') MOs and another one with Ni(3d,3d')+O(2p) MOs. The difference in energy between the cationic/anionic states and the neutral triplet state is the n-electron equivalent of the binding energy of the corresponding mono-electronic levels. The smaller Ni(3d,3d') active space is used to study the Ni($3d^n$) states restricting the ionization to localize on the Ni atom and, thus, obtaining the energies of the $3d^7$, $3d^8$ and $3d^9$ levels, which are required to calculate the Coulomb interaction U in NiO. On the other hand, the larger Ni(3d,3d')+O(2p) active space allows the ionization to delocalize on the ligand, enabling the description of ligand-hole levels, like the $3d^8\underline{L}$, and the calculation of the Δ parameter. We have calculated the U and Δ parameters of NiO by means of the relation given by Zaanen *et al.* [147]:

$$U_{NiO} = E(^4A^{3d^7}) + E(^2A^{3d^9}) - 2E(^3A^{3d^8}_{2g})$$

$$\Delta_{NiO} = E(^4A^{3d^8\underline{L}}) + E(^2A^{3d^9}) - 2E(^3A^{3d^8}_{2g})$$

Figure 4.6 shows the DOS nearby E_f for NiO at 300 K computed at the CASSCF level. Both $3d^7$ and $3d^8\underline{L}$ bands are highly overlapping, but the top $3d^8\underline{L}$ levels appear at slightly lower binding energies. This DOS is qualitatively in good agreement with the generally accepted behaviour of NiO, with a conductivity gap defined by the charge transfer process and a large mixing between the metal-hole and ligand-hole levels. Moreover, the calculation of Δ_{NiO} had to be done with data from only 24 out of the 32 conformations, because only those 24 structures have a $^4A^{n-1}$ electronic ground state of $3d^8\underline{L}$ character, with the hole localized in an O atom. The other 8 conformations have the hole mainly localized in the Ni atom independently of the active space used, being more similar to a $3d^7$ level. This behaviour confirms the large mixing between the $3d^7$ and $3d^8\underline{L}$

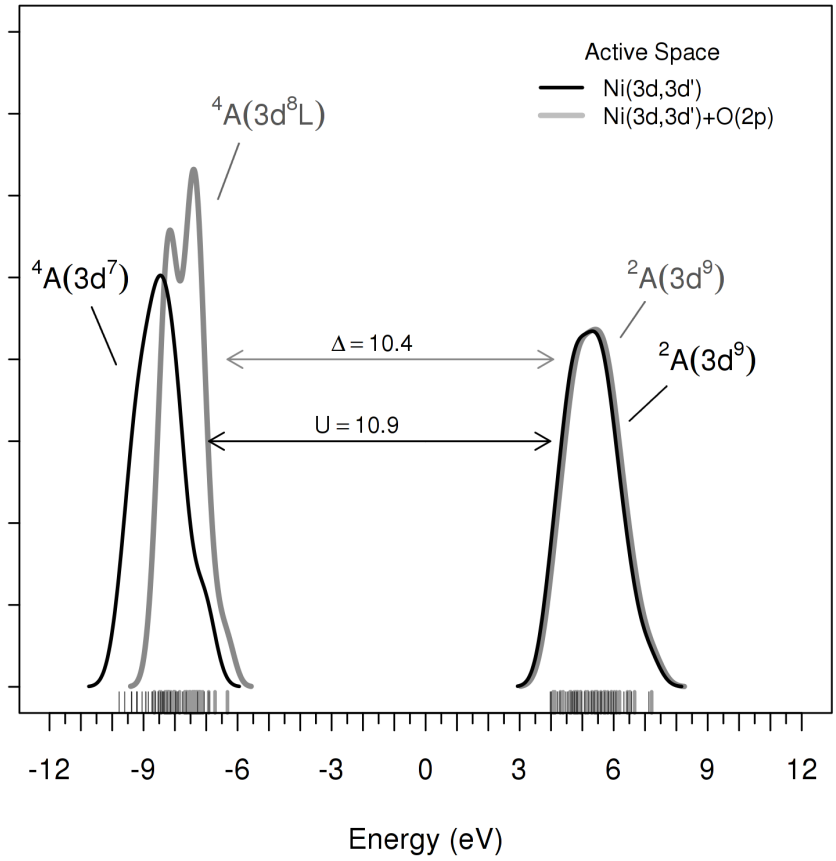

Figure 4.6: Density of states of NiO for the states nearby E_f at the CASSCF level. Obtained from a set of 32 conformations modelled with NiO_{14} clusters with a static non-polarized embedding. The energy of the $^3A_{2g}$ state is set as the reference value. Density estimation with Gaussian kernel functions ($bw \approx 0.3$ eV).

levels in NiO. However, even though the hole level character varies between different conformational structures, we have not observed any direct relation with simple distortions of the NiO_6 octahedron or the Madelung potential on the Ni site.

The mean computed values of U and Δ parameters for NiO are $\overline{U}_{NiO} = 13.8$ eV and $\overline{\Delta}_{NiO} = 13.0$ eV. As expected, both parameters are largely overestimated in comparison to data derived from experiment ($U \approx 5$ eV and $\Delta \approx 4$ eV). However, looking at the computed DOS (Figure 4.6) the actual picture is somewhat better. The inclusion of dynamical data and the associated phononic broadening reduces the gap by ~ 3 eV. Since the transitions involved are inter-site processes it will be more probable that the two active sites are found in different conformational states. This circumstance in the extreme case reduces these parameters to $U_{NiO} = 10.9$ eV and $\Delta_{NiO} = 10.4$ eV, which is of course a significant improvement but unfortunately these values are still too large. Nevertheless, the observed degree of broadening points towards a dominant role of the phonons over the hopping phenomena in determining the character of these ionic states, including the ligand hole states. Thus, confirming the local nature of this system.

Moreover, the calculation of the DOS for NiO at a higher level of theory, incorporating dynamical correlation effects through CASPT2, resulted in largely uneven reductions of the binding energy between the two cationic states. The $3d^7$ levels shift to ~ 2 eV lower energies while there is practically no change for the $3d^8\underline{L}$ levels, resulting in $U_{NiO} = 8.4$ eV and $\Delta_{NiO} = 11.0$ eV. The difference in correlation between these two types of states is caused by a deficient description of the ligand-holes levels compared to the metal-hole levels by the employed NiO_{14} cluster model, because the hole in a O ligand is surrounded by five Ni AIMP which do not contribute to correlation.

Therefore, we have obtained a good qualitative description of the DOS for NiO, but we also identified two main issues derived from the embedded cluster model employed. The static model employed is not able to correctly describe the large polarization that the addition/subtraction of an electron produces on the system and, on the other hand, the NiO_{14} cluster does not offer a good treatment of

ligand-hole states. Both effects lead to a deficient description of the states that take part in these phenomena.

Direct Reaction Field

Optical Absorption: Previous results obtained with a cluster model of the material in a static non-polarized embedding revealed the problems in treating the more polarizing excited states like the LMCT or the on-site electron-removal and electron-addition states. These phenomena generate large electronic distortions in the system that go far beyond the active site modelled by the cluster. In order to correct this shortcoming of the model we included extra-cluster polarization effects by means of the DRF method as described in section 4.2.

We started with a NiO_6 cluster and computed the induced polarization in the embedding caused by the lowest LMCT process. Figure 4.7 shows the modulus of the induced dipoles on the lattice sites surrounding the cluster (left) and a qualitative topological representation of the induced polarization in a slab of the embedding (right) for one arbitrary conformation. We observe large polarization effects near the cluster, which gradually decrease and become very small for lattice sites at more than 20 bohr from the central Ni atom. Although the chosen embedding size demonstrates to be large enough to account for the major part of the bulk polarization, it is preferable to increase the NiO_6 cluster by including the closest 32 oxygen ions with large induced dipoles and treat their polarization in the *ab initio* wave function.

Notwithstanding that such a NiO_{38} cluster gives a quite accurate treatment of the response phenomena, this large cluster combined with the DRF embedding turned out to be computationally too demanding and therefore we decreased the size of the cluster to NiO_{14}. This medium-sized cluster model incorporates into the wave function most of the system polarization with a reasonable computational cost, leaving in the embedding only five highly polarized ions ($1\ Ni^{2+} + 4\ O^{2-}$) found at ~ 9 bohr from the central Ni atom. In order to

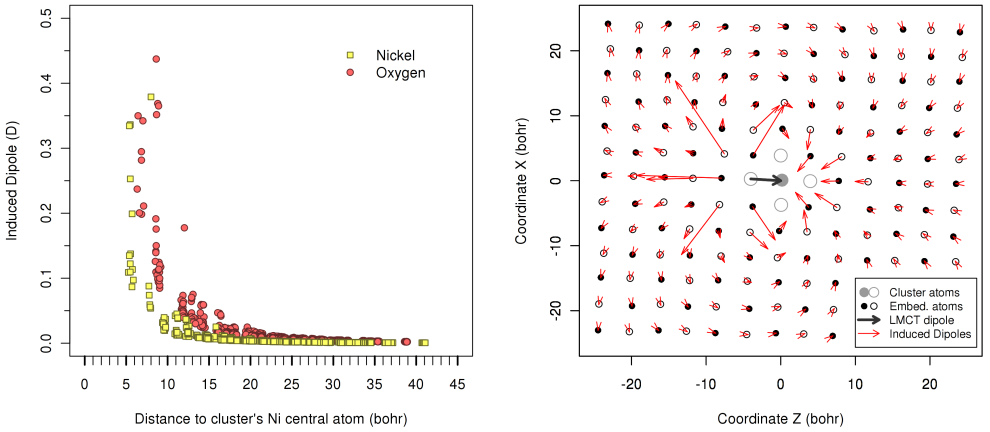

Figure 4.7: Induced dipoles by the LMCT in a NiO_6 cluster. Left: Variation of the modulus of the dipoles with the distance to the Ni central atom. The empty region between 0 – 5 bohr is the cluster's space. Right: Topological qualitative representation of the electronic polarization in a slab of the embedding (red) and the cluster (grey).

check the consistency of this model we performed DRF calculations for the local d–d transitions because this kind of excitations produce very small electronic changes in the crystal and, thus, the corresponding transition energies should not vary significantly by adding the polarization effects that they induce in the embedding. The resulting energies of all the d–d transitions increase by less than 0.03 eV on application of DRF, confirming the validity of the model.

Next, we repeated the calculations of the UAS spectrum of NiO but now with the bigger NiO_{14} cluster and incorporating the bulk polarization induced by excited states. We performed two series of calculations on 32 conformations applying the DRF method separately to the lowest nine 3d excited states and to the lowest two LMCT states. For both series, we obtained the average polarization caused by these two types of transitions. In this case we neglected the spin-orbit coupling and hence only considered spin-allowed transitions. Figure 4.8 shows the computed spectrum including both the d–d region and the charge transfer band. The triplet d–d bands remain practically unchanged compared with the non-polarized static embedding. The mean energy of each band changes

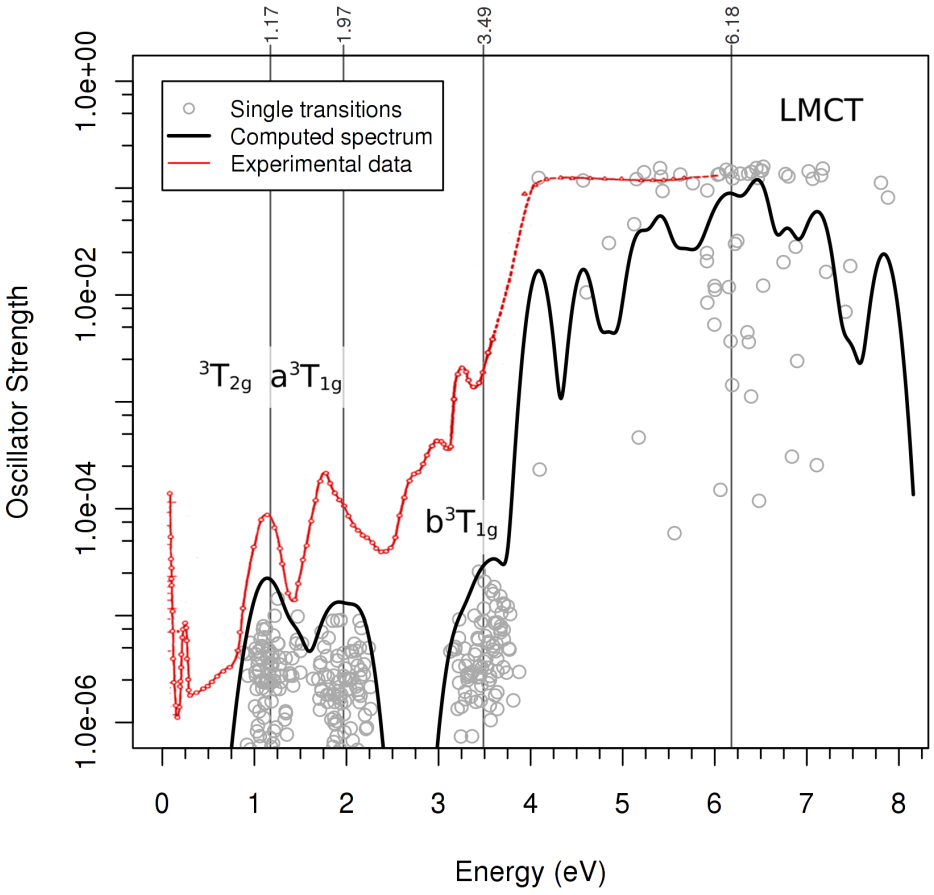

Figure 4.8: Absorption spectrum of NiO at 300 K computed with 32 conformations modelled by NiO_{14} clusters with a polarizable DRF embedding (black) and the experimental spectrum (red) [37]. The circles mark single electronic transitions from the ground state. The average energy of the absorption bands is noted on the upper part of the graph. Density estimation with Gaussian kernel functions ($bw = 0.092$ eV).

by $\sim$ 0.1 eV which is solely caused by the increase of the cluster model. On the other hand, the situation for the LMCT band is completely different. The relaxation produced by the induced bulk polarization shifts the LMCT band to lower energy by $\sim$ 2 eV bringing the computed spectrum in good agreement with the experimental one.

A detailed analysis of the origin of the broadening of the LMCT band reveals some interesting aspects. Figure 4.9 shows a comparison of the charge transfer band with and without extra-cluster polarization. Once the bulk polarization is conveniently treated, the induced polarization by the LMCT becomes the main factor in defining the broadening of the band. The polarization caused by the LMCT in the outer side of the Ni–O bond subject to the charge transfer process varies linearly along the band, experiencing a larger relaxation the LMCT states with a larger induced polarization. Since the LMCT excitations are highly localized in NiO, we quantified the degree of distortion of the NiO_6 octahedron along the LMCT band to check if there is a correlation between the induced polarization and the local geometry of the absorption site. Therefore, we defined two distortion parameters for the NiO_6 cluster, the standard deviation of the 6 Ni–O bonds (σ_r) and the standard deviation of the 12 O–Ni–O angles ($\sigma_\angle$) with respect to the ideal O_h structure of NiO_6:

$$\sigma_r = \sqrt{\frac{1}{N_r}\sum_{i=1}^{N_r}(r(NiO)_i - r(NiO)_{O_h})^2}$$

$$\sigma_\angle = \sqrt{\frac{1}{N_\angle}\sum_{i=1}^{N_\angle}(\angle(ONiO)_i - \angle(ONiO)_{O_h})^2}$$

being $r(NiO)_{O_h} = 3.9343$ bohr and $\angle(ONiO)_{O_h} = 90°$.

The mean values of σ_r and $\sigma_\angle$ in intervals of 1.0 eV for each LMCT band are shown with overprinted filled circles in Figure 4.9. Although we have no sufficiently large samples to go in deeper detail than 1.0 eV and these are simple measures of the cluster distortion that only account for the immediate environment of the Ni central atom, they do offer a first glimpse to the internal

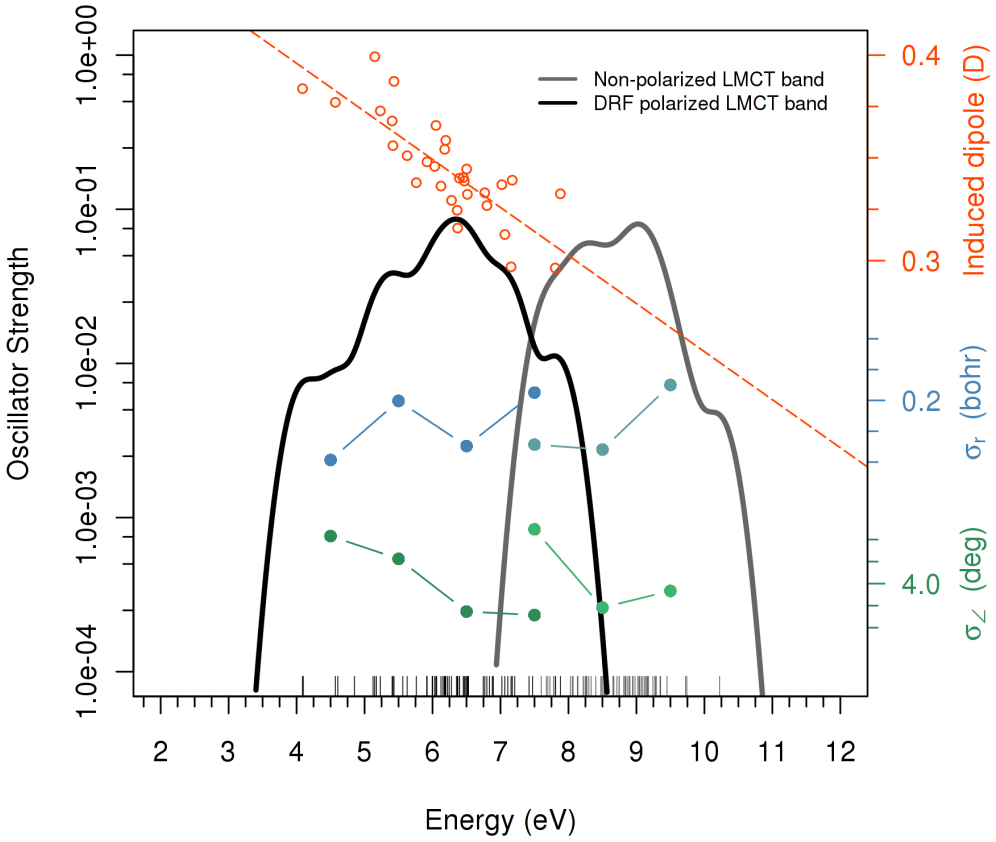

Figure 4.9: Comparison between the LMCT bands with polarization of the embedding (black) and without (grey). Filled circles show the NiO_6 octahedron distortion along the band, $\sigma_\angle$ in green and σ_r in blue. Empty orange circles show the total induced dipole in the 5 most polarized ions outside the cluster. Density estimation with Gaussian kernel functions ($bw = 0.229$ eV).

structure of the LMCT band. In the first place, we concentrate on the LMCT band obtained before including the extra-cluster polarization. The center of the band arises mainly from conformations that are weakly distorted with respect to the ideal octahedral structure, with low values of both $\sigma_{\angle}$ and σ_r, whereas the distortion of the system increases to both extremes of the band. The situation changes significantly once the electronic response of the environment is taken into account. The broadening of the band is now primarily driven by the LMCT induced polarization. In this case, the conformations with a highly distorted NiO_6 cluster, mainly because of a larger $\sigma_{\angle}$, produce a higher polarization in the Ni–O bond direction where the LMCT occurs and experience a larger stabilization of their LMCT transition energies. As a consequence, these states become the front of the band. On the other hand, the more symmetric structures induce a lower polarization on their surroundings having higher LMCT states and appearing at the high-energy end of the band. Moreover, we performed calculations of the LMCT states for an idealized octahedral structure of NiO using the same model employed for the rest of the conformations. The LMCT energy of this ideal conformation of NiO resulted in 8.55 eV with a non-polarized embedding and 6.83 eV with DRF, which are in good concordance with the analysis previously made. Nonetheless, this is indeed a first simple analysis of the broadening of the LMCT band, which indicates that the crystalline structure has some influence in the stabilization of the LMCT. Further analysis of this influence will require a more detailed study with a larger conformational set and considering long-range structural distortions.

These results demonstrate that the response phenomena have a crucial role in those excited states that cause large electronic distortions on the absorption site. Moreover, the embedded cluster model proves to be adequate to study these phenomena on highly correlated materials like NiO, where the underlying phenomena of the UAS spectroscopy can be considered highly localized. While in a theoretical treatment of the electronic structure based on the ideal and highly symmetric geometry, the band broadening is usually ascribed to hopping processes of the holes or electrons, the present results suggest a different viewpoint. Here, the broadening of the valence and conduction band is caused by the inho-

mogeneity of the structure due to the movement of the nuclei, which introduces variations in the relative energies of the relevant n-electron states. Furthermore, the DRF method showed as an adequate approach to treat the polarization in crystalline environments under the condition that the largest polarization effects are treated in the wave function and that the artificial polarization of the ground state is removed from the system.

Conduction Band Gap: We applied the DRF method to the calculation of the U and Δ parameters of NiO. We performed this study on only five conformations due to the problems found in the DOS calculation without DRF (section 4.3), but nonetheless we tried to address the issue regarding the lack of extra-cluster polarization offered by the static embedding. The resulting parameters at the CASPT2 level are $U_{NiO} = 3.0$ eV and $\Delta_{NiO} = 4.6$ eV, which are in much better agreement with the expected values of $U \approx 5$ eV and $\Delta \approx 4$ eV than the values obtained with the non-polarized embedding. Hence, the inclusion of electronic response effects turns out to be very important for the description of the band gap, as it is expected due to the large electronic distortions caused by the ionized states involved.

However, these values for U and Δ still suffer from the poor description of the ligand-hole states offered by the NiO_{14} cluster. Δ_{NiO} should be lower than U_{NiO}, which is the case at the CASSCF level, but U shifts from 7.2 eV to 3.0 eV upon application of the CASPT2 step, whereas Δ practically does not change. Figure 4.10 shows a qualitative representation of the polarization induced by the cationic $3d^7$ (left) and $3d^8\underline{L}$ (right) levels. There are large differences in the embedding polarization depending on where the hole is localized. In the case of the ligand-hole level involved in Δ_{NiO} ($3d^8\underline{L}$) there is a large polarization on atoms outside the cluster region which, preferentially, should be treated in the n-electron wave function by enlarging the cluster.

Furthermore, the calculated U value is slightly lower than previous theoretical estimations [157]. The source of this deviation could be an overestimation of the extra-cluster polarization by the DRF method, which relies on atomic polarizability parameters. It must be noted that the calculation of the DOS

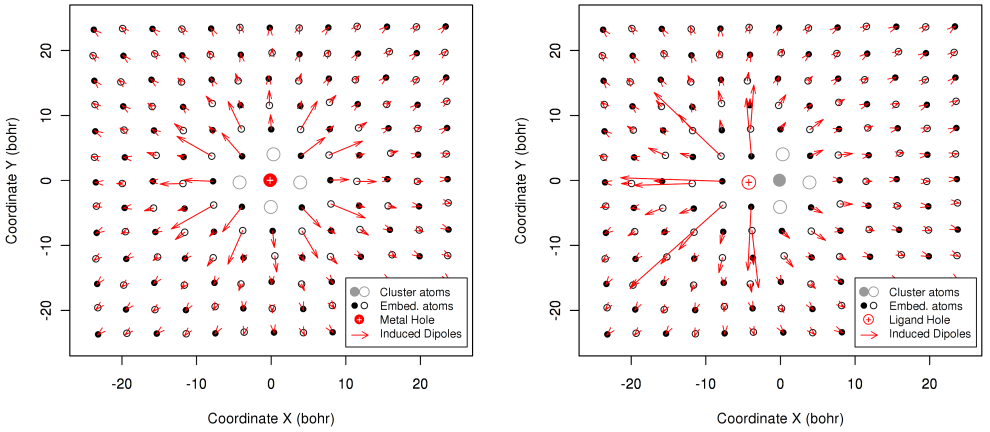

Figure 4.10: Topological qualitative representation of the polarization in a slab of the embedding of a NiO_{14} cluster by the $3d^7$ level (left) and the $3d^8\underline{L}$ level (right).

with the DRF embedding is not possible due to a limitation of the employed model. The potential energy between the cationic, anionic and neutral systems results in large non-physical differences. The NiO_{14} cluster with 42 Ni^{2+} AIMPs is far from the stoichiometry of the NiO crystal and has a total formal charge of 56+. This positively charged cluster combined with a polarized embedding puts each state in a different potential background, preventing the calculation of the electron affinity and ionization potential and, consequently, the computation of the DOS of NiO with DRF. Notwithstanding this shortcoming of the material model, the calculation of U and Δ parameters is possible, because the involved cationic and anionic states produce opposed electric potential shifts, which are mutually compensated on the calculation of the band gap parameters applying the expression of Zaanen *et al.* [147]. A more detailed explanation of this limitation of the employed cluster model is available in the Appendix A.

NiO_{38}

We compared the method proposed here for including the extra-cluster polarization through DRF against calculations of a big NiO_{38} cluster in a static non-polarized embedding. The NiO_{38} cluster is expected to include the major part of the response due to the O^{2-} ions, the most polarizable atoms in the lattice. The static model potential representation of Ni^{2+} neglects any polarization effect due to these cations. We have calculated the LMCT absorption edge and the U and Δ parameters with this big cluster (Table 4.2). In the case of the LMCT process we observe an important lowering of the excitation energy from 8.53 to 6.11 eV. This behaviour is expected, as we already showed that the ions with the largest induced dipoles are left outside the cluster in the NiO_{14} case, whereas the NiO_{38} incorporates them. However, the bulk polarization extends beyond the limits of the NiO_{38} cluster (see Figure 4.7) and, moreover, the induced dipoles on Ni^{2+} ions in the cluster surrounding are significant. Therefore, it is not possible to obtain accurate results of the LMCT energies with a static non-polarized model. We tried to improve this result by using the DRF embedding obtained with the NiO_{14} cluster in the NiO_{38}, but even though the resulting LMCT energy is better, it does not offer good accuracy (5.39 eV). Obviously, the induced dipoles and the cluster electronic density must be included in a self-consistent manner, which is computationally too expensive, at present.

The situation is similar for the calculation of U: the NiO_{38} cluster recovers $\sim 40\%$ of the polarization caused by the $3d^7$ and $3d^9$ ionized levels. In the case of

Table 4.2: Comparison of the LMCT energy and U and Δ parameters obtained with the different models employed in the present work. The computational time (t) in hours of the LMCT calculations are included.

		LMCT		U	Δ
Cluster	Emb.	E (eV)	t (h)	E (eV)	E (eV)
NiO_{14}	Static	8.53	32	13.8	12.7
NiO_{38}	Static	6.11	97	9.9	13.2
NiO_{14}	DRF	4.09	141	4.5	5.4

cationic/anionic states the polarization spreads further away and induces weaker dipoles in the vicinity of the cluster than in the LMCT transition, reducing the amount of polarization incorporated in the NiO_{38} cluster. On the other hand, in the case of the Δ parameter there is no gain by using this bigger cluster. An important reason for this situation is that the hole in the $3d^8\underline{L}$ state is not localized on the center of the cluster (see Figure 4.10); the localization of the hole in the O atom induces large polarization on its neighbouring region, which will need even a bigger cluster than NiO_{38} to be treated effectively.

In terms of computational cost, the NiO_{14} cluster with the DRF embedding calculations are the most expensive we performed. Due to the iterative process required to reach self-consistency, treating the bulk polarization has a cost ~ 5 times larger than using a static non-polarized embedding. However, the difference becomes rapidly smaller as the cluster size increases. Compared to NiO_{38}, the difference is reduced to 1.5 times approximately, but still resulting in a better description of the system.

4.4 Conclusions

We have combined successfully three different methodologies to provide an *ab initio* description of the electronic structure of local excitations in ionic insulators taking NiO as a prototype. We used the Car-Parrinello MD simulations to incorporate the effect of the lattice vibrations on the local structure at one of the Ni sites. By means of the CASPT2 method we were able to study the electronic excited states with an efficient treatment of the electron correlation. Moreover, we could include electronic response effects in the form of bulk polarization in the material model, by coupling the electronic structure calculations self-consistently with the DRF method.

As a first application of the procedure we have studied the absorption spectrum of NiO and its DOS near the Fermi energy. These features are convenient to be treated by the proposed procedure as they imply localized changes in the

electronic structure, which can be described using the embedded cluster model. The best results for both the absorption spectrum and the DOS have been obtained with the NiO_{14} cluster incorporating the DRF embedding to take into account extra-cluster polarization effects.

The computed UAS spectrum is in good agreement with the experimental data (Figure 4.8). The results obtained by incorporating the Car-Parrinello MD simulations allowed to pinpoint the origin of some features observed in the spectrum, like the d–d transitions to a^1E_g and a^1T_{2g} singlet states, at 1.97 eV and 2.86 eV respectively (Figure 4.5). Moreover, by integrating the DRF into the model, we could explain the origin of the broadening of the LMCT band as caused by a linear decrease of the induced polarization on the different conformational structures that form the band (Figure 4.9). Finally, the computed U and Δ parameters are in good agreement with their expected values. Even though the phononic broadening reduces the conductivity gap by ~ 3 eV, the main reduction factor with respect to a static embedding appears to be the bulk polarization, which lowers this gap to $U_{NiO} = 3.0$ eV and $\Delta_{NiO} = 4.6$ eV.

The major drawback of the method is the high computational cost, which makes cumbersome the use of larger conformational sets to analyse with deeper detail the resulting data for both the UAS spectra and the DOS. Furthermore, it has been shown that it might be also necessary to use a larger cluster than NiO_{38} to treat ligand-hole states like the $3d^8\underline{L}$, where the hole is localized in a ligand O atom away from the center of the cluster. The effect of the extra-cluster polarization in cationic/anionic states is still an issue not completely resolved which will need further investigation.

Nevertheless, the method presents an important advance in the *ab initio* description and analysis of the electronic structure of transition-metal oxides. We conclude that the local LMCT process is the origin of the optical gap starting at 4.1 eV and that the conductivity gap is slightly larger, between 4.5 – 5.0 eV, being caused by U or Δ depending on the conformational distortions. The computational issues are expected to become less and less important given the ever increasing computer power.

UNIVERSITAT ROVIRA I VIRGILI
THEORETICAL DESCRIPTION OF ELECTRONIC EXCITATIONS IN EXTENDED SYSTEMS:
BEYOND THE STATIC MATERIAL MODEL
Alex Domingo Toro
DL:T. 1705-2011

CHAPTER 5

Ab initio study of the optical absorption data of $LaMnO_3$: the MMCT as the origin of the 2.0 eV peak

5.1 Introduction

The discovery in the 1990s of colossal magnetoresistance (CMR) at room temperature in manganese oxides [179] renewed the interest in this family of materials [180]. The CMR involves an interrelated change in the ordering of charge, magnetism and crystal lattice degrees of freedom of these perovskite-type manganites. These phenomena are mainly determined by cooperative effects that arise from the high electron correlation of these materials. However, it is not straightforward to establish the origin of these cooperative effects, which involve the interplay of the electronic structure, the crystal phonons and the lattice structure.

The prototype perovskite $LaMnO_3$ has a lattice structure formed by corner sharing MnO_6 Jahn-Teller (JT) distorted octahedra, with La ions enclosed in boxes formed by eight MnO_6 groups. Thus, the lattice presents an alternate orientation in the *ab*–plane of the long Mn–O bond of the MnO_6 pseudo-octahedra, in the so-called collective JT mode. Additionally, the adjacent MnO_6 groups are tilted on the *ab* directions, leading to O–Mn–O angle values smaller than 180°. Figure 5.1 shows a schematic representation of the $LaMnO_3$ crystalline structure. [181]

The manganese metal ions are formally $3d^4$ Mn^{3+} with a high spin (HS) ground state electronic configuration ($t_{2g}^3 e_g^1$). The half occupied e_g orbitals present an ordering in the *ab*–plane below $T_{OO} = 780$ K [182], which follows the lattice alternation in orientation of the MnO_6 pseudo-octahedra. The orbital ordering is accompanied by an A-type antiferromagnetic (AF) ordering below the Néel temperature ($T_N = 140$ K) [183] and, in the case of doped $LaMnO_3$ systems, there can also be a charge ordering along the Mn sites [184]. These phenomena are part of the cooperative effects that are present in $LaMnO_3$ and play a fundamental role on its electronic and magnetic properties. However, the description of the detailed interplay between the lattice, phononic and electronic properties is difficult to perform. The cooperative nature implies that either the

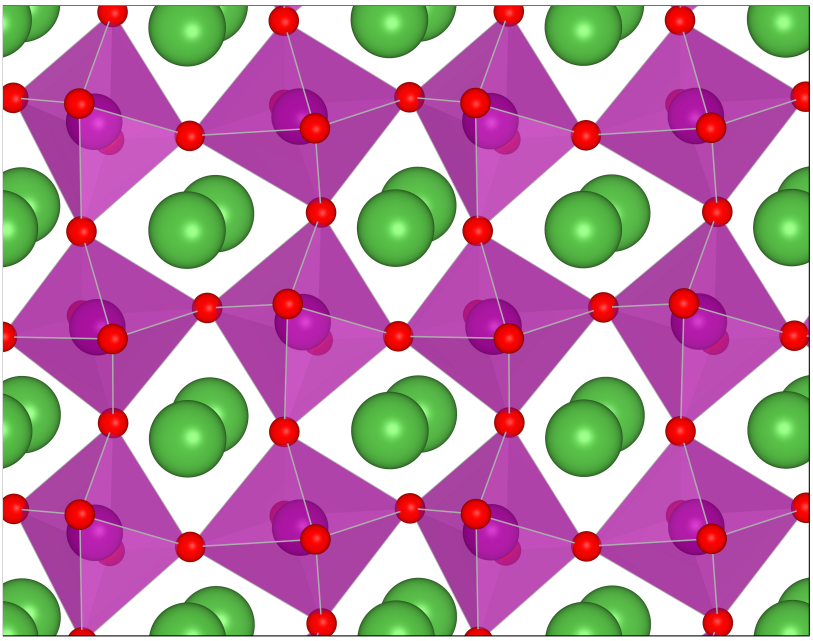

Figure 5.1: Schematic representation of the $LaMnO_3$ crystalline structure. Expansion of MnO_6 octahedra on the lattice *ab* directions is shown in purple. The green atoms exemplify the positions of the deeper La ions.

electron-electron interaction leads to the orbital ordering that causes the lattice distortion; or, otherwise, that the electron-phonon interaction breaks the metastable undistorted state, causing the lattice distortion that produces the orbital ordering patterns [185, 186].

The analysis of the optical properties of $LaMnO_3$ contributes to a better comprehension of the electronic structure of this material. The optical conductivity spectra of $LaMnO_3$ show an optical gap of $\sim$ 1 eV and a first band with a maximum peak at $\sim$ 2 eV [187]. However, the nature of the $LaMnO_3$ optical gap and the source of the first band are difficult to identify. Quantitative analysis of $LaMnO_3$ optical conductivity spectra suggested that the on-site Coulomb interaction (U) and the JT splitting are behind the origin of the gap [188]. Additionally, calculations based on the tight-binding model predicted a value of $U = 1.6$ eV [189]. Both results point towards a d–d transition as the source of

the first absorption band. On the other hand, the polarization and temperature dependence of the spectra suggested that the ~ 2 eV band is caused by a charge transfer (CT) process of p–d character [190]. Nonetheless, wave function calculations based on the embedded cluster approach offered an accurate description of the local electronic structure on the Mn sites, including the JT and crystal field (CF) splittings, and revealed that the lowest ligand CT states appear above 3 eV [191, 192]. Moreover, studies based on temperature-dependent optical absorption spectra of $LaMnO_3$ thin films [193] and the spectral ellipsometry technique [194], which were subsequently complemented with theoretical model calculations [195, 196]; showed that the absorption band at ~ 2 eV is probably caused by an inter-site d–d transition between two adjacent Mn atoms on the *ab*–plane, the so-called metal to metal charge transfer (MMCT). Therefore, the $LaMnO_3$ could not be classified following the ZSA model [147] because neither the on-site Coulomb interaction U nor the charge transfer Δ would be the origin of the optical gap.

The aim of the present work is to theoretically investigate the MMCT hypothesis, the latest proposed source of the ~ 2 eV peak in the spectra of $LaMnO_3$. The *ab initio* wave function based methods applied to embedded cluster models of $LaMnO_3$ proved adequate to treat the high electron correlation of this system and resulted in accurate descriptions of the crystal field states, including the effects of lattice ordered distortions [191, 192]. Therefore, we applied and improved this approach to study the MMCT states, which is much more challenging due to the inherent higher complexity of this type of transitions. Two Mn sites must be included in the wave function, which implies working with, at least, a Mn_2O_{11} cluster to get a balanced description of both sites. The electronic structure of this model can incorporate the localized MMCT between the two Mn sites, but it also requires an efficient treatment of the dynamical correlation, which largely benefits the MMCT transitions. Thus, we perform Complete Active Space Self-Consistent Field (CASSCF) [32] and Restricted Active Space Self-Consistent Field (RASSCF) [197] calculations, combined with a subsequent Second-Order Perturbation theory step (CASPT2) [34], on various embedded cluster models of $LaMnO_3$. Furthermore, since charge transfer processes can

produce significant electronic changes in the absorption site, we include a Direct Reaction Field (DRF) [166–168] on the embedding of the cluster to take into account the electric adaptation of the surroundings of both Mn sites and study its derived relaxation effect on the MMCT transition.

5.2 Computational Scheme

We applied the embedded cluster approach to model the $LaMnO_3$. This method defines a finite piece of the whole crystal (cluster) large enough to describe the phenomena of interest. The long range electrostatic effects of the bulk material are incorporated by means of a distribution of point charges surrounding the cluster (embedding). The relatively small size of the cluster makes possible to employ sophisticated *ab initio* quantum chemical methods that offer an efficient treatment of both the static and dynamic electron correlation. This procedure has proved as an adequate strategy to study localized electronic processes that take place in materials with strongly correlated electron movement, typical of many transition-metal compounds [198, 199]. Furthermore, it is important to consider extra-cluster polarization effects induced by the MMCT process, which produces a large electronic distortion in the cluster and on its surroundings. The polarization of the embedding is incorporated in a self-consistent scheme, integrating the DRF method with the electronic structure calculations.

Electronic Structure

We defined a $[MnO_6]^{9-}$ cluster to perform all-electron calculations of one Mn site and its coordination sphere of six O atoms. The electronic structure of this cluster will serve to study the internal d–d transitions on the metal center. We also built a bigger $[Mn_2O_{11}]^{16-}$ cluster to include two Mn sites in the quantum region and be able to investigate the MMCT process between those neighbouring sites. Figure 5.2 shows a graphical representation of such cluster models. Both clusters are surrounded by a first layer of *Ab Initio* Model-Potentials (AIMP) [159]

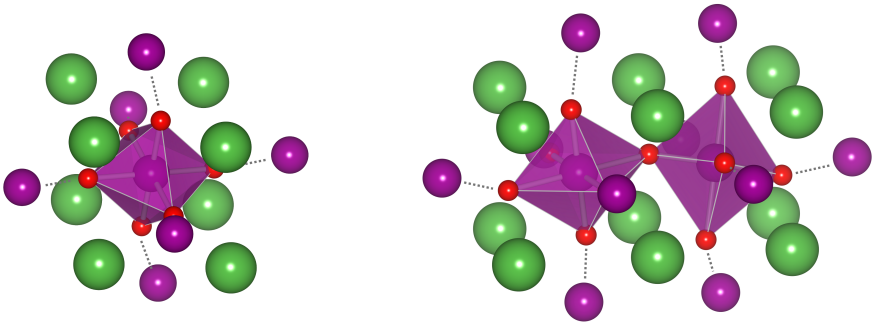

Figure 5.2: Structure of the two employed cluster models. The purple octahedra represent the quantum described cluster region and the surrounding spheres represent model potentials of La (green) and Mn (purple) atoms. Left: $[MnO_6]^{9-}$ cluster with 8 La^{3+} and 6 Mn^{3+} AIMPs. Right: $[Mn_2O_{11}]^{16-}$ cluster with 12 La^{3+} and 10 Mn^{3+} AIMPs.

that reproduce the short-range interactions between the cluster and its immediate environment. The AIMPs reduce the electronic dispersion from the cluster to the surrounding cations and, additionally, can incorporate orthogonalization basis functions. The $[MnO_6]^{9-}$ cluster has eight La^{3+} and six Mn^{3+} AIMPs and the $[Mn_2O_{11}]^{16-}$ cluster has twelve La^{3+} and ten Mn^{3+} AIMPs. The cluster and the AIMPs are embedded in a distribution of point charges placed on lattice positions. The value of the point charges is optimized to accurately reproduce the Madelung potential on the cluster region [200]. The embedding of the $[MnO_6]^{9-}$ cluster is formed by a total of 188 point charges and the $[Mn_2O_{11}]^{16-}$ cluster is surrounded by a total of 1113 point charges. Similar models to the hereby presented have been successfully employed to study the electronic structure of $LaMnO_3$ [50, 184, 191, 192], including a localization scheme based on cluster fragments proposed by Stoyanova *et al.* [201].

The electronic structure calculations of the $[MnO_6]^{9-}$ cluster are performed by means of the CASPT2 method. The active space defined for this system is a CAS(4,10), which includes four electrons on five Mn(3d) molecular orbitals (MO) and a shell of five Mn(d) MO, which are more diffuse 3d orbitals with an additional radial node, the so-called Mn(3d'). This extra set of orbitals im-

proves the capabilities of the wave function to describe the crystal-field states of $LaMnO_3$, which have significant covalent contributions that require to incorporate some charge transfer character from the neighbouring O atoms into the otherwise $3d$ pure states [50, 202]. Furthermore, to obtain an optimal treatment of the covalency observed in $LaMnO_3$, we employ atomic natural orbital basis sets including scalar relativistic effects (ANO-RCC) on both Mn and O atoms of the cluster. A contracted set of (6s,5p,4d,2f) basis functions was employed for the Mn [46] atom and another contracted set of (4s,3p,2d) basis functions for the O [45] atoms. The calculations of the internal Mn d–d transitions is done by means of state average CASSCF calculations of the lowest five quintet states and the lowest five triplet states of the $[MnO_6]^{9-}$ cluster. The subsequent CASPT2 step has a shift factor set to 0.20 a.u. to eliminate possible intruder states [113].

The direct extrapolation of the former active space and state average calculations to the description of MMCT states in the $[Mn_2O_{11}]^{16-}$ cluster does not lead to the same success achieved for the crystal-field states. The main shortcoming of the CASSCF/CASPT2 method is that the dynamical correlation is recovered *a posteriori* from the CASSCF reference wave function. This procedure is not conveniently suited to treat the MMCT states, which largely benefit from dynamical correlation effects and, therefore, can not be properly described at the CASSCF level. An example can be found in the research of the photoinduced magnetization on cyanomolibdates performed by Carvajal *et al.* [203], who found clear deficiencies on the CASPT2 calculations of MMCT states. On a first approach, the MMCT of $LaMnO_3$ can be calculated by a state average CASSCF calculation with a CAS(8,20) formed by two sets of Mn(3d,3d') orbitals, one on each Mn site. The result is that the MMCT state is found as the 26^{th} root, having a very low weight of 1/26 on the MO optimization procedure. Due to the large differences between a MMCT excitation and the other 25 crystal-field states, the description of the orbitals obtained is rather deficient for the MMCT state and causes the subsequent CASPT2 step to fail. The analysis of the results of the CASPT2 calculation reveals large contributions from excitations involving the bridge O between the two Mn metal atoms. However,

including a single O(2p) orbital in the active space introduces a huge number of extra excitations in the electronic structure. The state average increases with ligand to metal charge transfer states, in addition to the MMCT and crystal-field states. Due to the lack of dynamical correlation, the MMCT is found above most of those other states at the CASSCF level, even above the lower 300 states of the system. Making completely unfeasible this approach.

We opted for a different approach to get a better description of the MMCT using wave function based methods. Instead of increasing the active space to improve the capabilities of the wave function to describe the electronic states of the system, we put additional restrictions on the active space to reduce the number of roots contained in it. In this way, the weight of the MMCT in the MO optimization procedure can be increased, leading to an improvement of the orbital space for that particular state. We switch to the RASSCF method for the calculations on the $[Mn_2O_{11}]^{16-}$ cluster. This method works with a restricted active space (RAS) that is divided in three sub-spaces, the so-called RAS1, RAS2, and RAS3; and makes possible to control the number of allowed excitations between the sub-spaces. We defined a RAS space with eight electrons in six Mn(t_{2g}–like) orbitals in the RAS1 sub-space, four Mn(e_g–like) on the RAS2 sub-space and all the Mn(3d') orbitals on the RAS3 sub-space. Additionally, we limited the number of holes in the RAS1 space to six, disallowing any excitation from this set of orbitals. The main benefit obtained with this active space is that the MMCT is now found as the fifth excited root of the system, having a much larger weight in the orbital optimization. We also explore the application of the RASPT2 method with the resulting RASSCF wave function as reference.

Previous works proposed that the the most probable MMCT process occurring at ~ 2 eV is an excitation from the local quintet HS state of one Mn site to a local HS sextet state of the neighbouring Mn atom [193, 194]. Thus, we computed the nonet electronic states of the $[Mn_2O_{11}]^{16-}$ cluster, which incorporates both HS states in a ferromagnetic coupled nature as found experimentally in the *ab*–plane. All the calculations have no symmetry restrictions due to the JT effect and the tilted distortions of the lattice structure. The Cholesky decomposition of the two-electron integrals was applied to reduce the computational cost [44, 204].

The electronic structure calculations were carried out with the MOLCAS 7.2 package [48, 49].

Direct Reaction Field

We investigate the effect of the electric response phenomena on the crystalline environment of the lattice sites involved in the MMCT process. The charge transfer excitations cause significant alterations on the electronic density of the atoms affected. The MMCT of the $LaMnO_3$ is a next-nearest-neighbour charge transfer that will produce a relatively large dipole between two Mn atoms. Additionally, this localized rearrangement of charge will produce some changes on the surrounding crystal, both structural and electrical. Therefore, to obtain a better theoretical description of the MMCT transition, we treat the electric response phenomena on the embedding of the cluster model by means of the DRF method, in a similar fashion as in the Quantum Mechanics / Molecular Mechanics schemes.

The DRF method is incorporated self-consistently with the RASSCF electronic structure calculations. The basic procedure consists in computing the electronic structure of the cluster; generate the induced dipoles by the quantum region electronic density in the embedding; incorporate the polarized embedding in the electronic structure calculation of the cluster; and repeat until self-consistency. Moreover, the cluster model causes an artificial polarization, caused by its isolation in an infinite void, that must be systematically subtracted from the induced dipoles by the MMCT transition. The ground state does not produce any polarization on the crystal and, thus, as a first step, it is necessary to compute the induced polarization by the electronic ground state of the system to correct this artefact. Once the polarized embedding is converged for the state average RASSCF of the ground state, plus three d–d states and the MMCT; it can be linearly extrapolated to obtain the induced dipoles solely by the MMCT transition, as described in detail in chapter 4.

The DRF method requires to define the atomic polarizability of each atom in the system. We set $\alpha_{O^{2-}} = 1.988$ Å^3 for the O atoms, $\alpha_{Mn^{3+}} = 2.140$ Å^3 for the Mn atoms and $\alpha_{La^{3+}} = 2.798$ Å^3 for the La atoms [176]. The DRF calculations were performed with the DRF90 software [177].

5.3 Results

MnO_6 Cluster

Table 5.1 shows the resulting energies at the CASSCF and CASPT2 levels for the lowest five quintet states and the lowest five triplet states of the MnO_6 cluster. The excited states considered are all crystal-field states, which allow the study of internal Mn d–d transitions arising from the quintet ground state (^5E_g). Taking into account the typical accuracy of the CASPT2 method for the d–d transitions (≤ 0.15 eV), the calculated transition energies show that there is no one close to 2.0 eV at the CASPT2 level. Moreover, the oscillator strength of these absorptions calculated on a Mn_2O_{11} cluster is of the order of 10^{-6}, which is far too low to explain the intense band observed in the spectrum. In fact, d–d transitions on the Mn^{3+} sites are dipole forbidden given the inversion symmetry at those sites. They become very weakly allowed by coupling to phonons that lift the local inversion symmetry. Therefore, we discard an on-site d–d process as the source of the $LaMnO_3$ first absorption peak.

Mn_2O_{11} Cluster

Table 5.2 summarizes the CASSCF and RASSCF results obtained for the MMCT transition on a Mn_2O_{11} cluster. The MMCT energy obtained from the state average CASSCF calculation with a CAS(8,20) is clearly overestimated (13.65 eV). The reason is the small weight of the MMCT state in the energy expression that is minimized in the molecular orbital optimization procedure.

Table 5.1: Energy of the lowest Mn internal d–d electronic transitions of the MnO_6 cluster.

	Transition Energy (eV)	
State	CASSCF	CASPT2
^5E_g	0.00	0.00
	1.23	1.33
$^3T_{1g}$	1.43	1.20
	1.60	1.39
	1.82	1.62
$^5T_{2g}$	2.20	2.47
	2.45	2.73
	2.61	2.90
^3E_g	2.63	2.31
	2.91	2.49

As mentioned before, this leads to a poor description of the MMCT state. The CASPT2 results of this system show large contributions from excitations involving bridge O(2p) orbitals. Thus, we increased the active space by including one O(2p) MO and improve the capability of the wave function to describe the MMCT. However, using this larger active space in the form of a RAS(10,21) and allowing only single excitations from the RAS1 formed by the O(2p) and six Mn(t_{2g}–like) MOs, the MMCT state rises to the root 175, obtaining an even worse estimation of the transition energy (14.45 eV) and making impossible to perform the subsequent perturbation theory step.

On the other hand, by using an opposed approach and reducing the active space of the RASSCF calculations, the predicted MMCT energy improves. The state average RASSCF of five nonet states on a RAS(8,20) without any allowed excitation from the RAS1, shows again a clear overestimation of the transition energy (12.71 eV), but it is slightly lower than for the CASSCF case. This improvement is directly related to the limitations established in the number of excitations permitted and the consequent increase of weight in the MO optimization procedure

Table 5.2: Energy of the lowest MMCT state resulting from Mn_2O_{11} cluster calculations with complete and restricted active spaces.

	CASSCF		RASSCF		
Active Space	$(8, 20)$	$(10, 21)$	$(8, 20)$	$(8, 20)$	$(8, 20)$
RAS1 Holes	–	7	6	6	6
MMCT Root	26	175	5	5	5
Weight (%)	3.85	0.01	20.00	60.00	52.94
MMCT Energy (eV)	13.65	14.45	12.71	7.80	6.11
Embedding	Static	Static	Static	Static	DRF
	CASPT2		RASPT2		
Reference Weight (%)	49.72	–	48.19	53.74	53.49
Imaginary Shift (a.u.)	0.5	–	0.5	0.5	0.5

of the MMCT state. The morphology of the two e_g–like orbitals involved in the MMCT transition are very similar on both cases, but the MOs resulting from the RASSCF calculation are more oriented towards the Mn–O–Mn direction and show a higher delocalization over the O bridge (Figure 5.3). Therefore, the loss of flexibility in the wave function is completely compensated by an improvement of the molecular orbitals participating in the MMCT transition. Moreover, the restricted active space removes many excited states from the Mn_2O_{11} electronic structure, generating a gap of $\sim$ 10 eV between the MMCT and the fourth excited state, a double d–d transition. This situation offers the possibility to increase the weight of the MMCT in the energy expression, leading to a set of molecular orbitals that are better adopted to describe the MMCT state. This process would, of course, converge to MOs exclusively optimized for the MMCT state if the weight could be increased to 100%.

However, the MMCT weight can be increased to 60% before it relaxes to the same energy level of the fourth state, which rises in energy due to its diminution of weight in the average and, consequently, the root flipping between these states avoids any further increase of the MMCT weight. The effect of increasing the MMCT weight to 60% is large and lowers the transition energy by $\sim$ 5 eV. Additionally, the reference weight of the subsequent RASPT2 calculation also

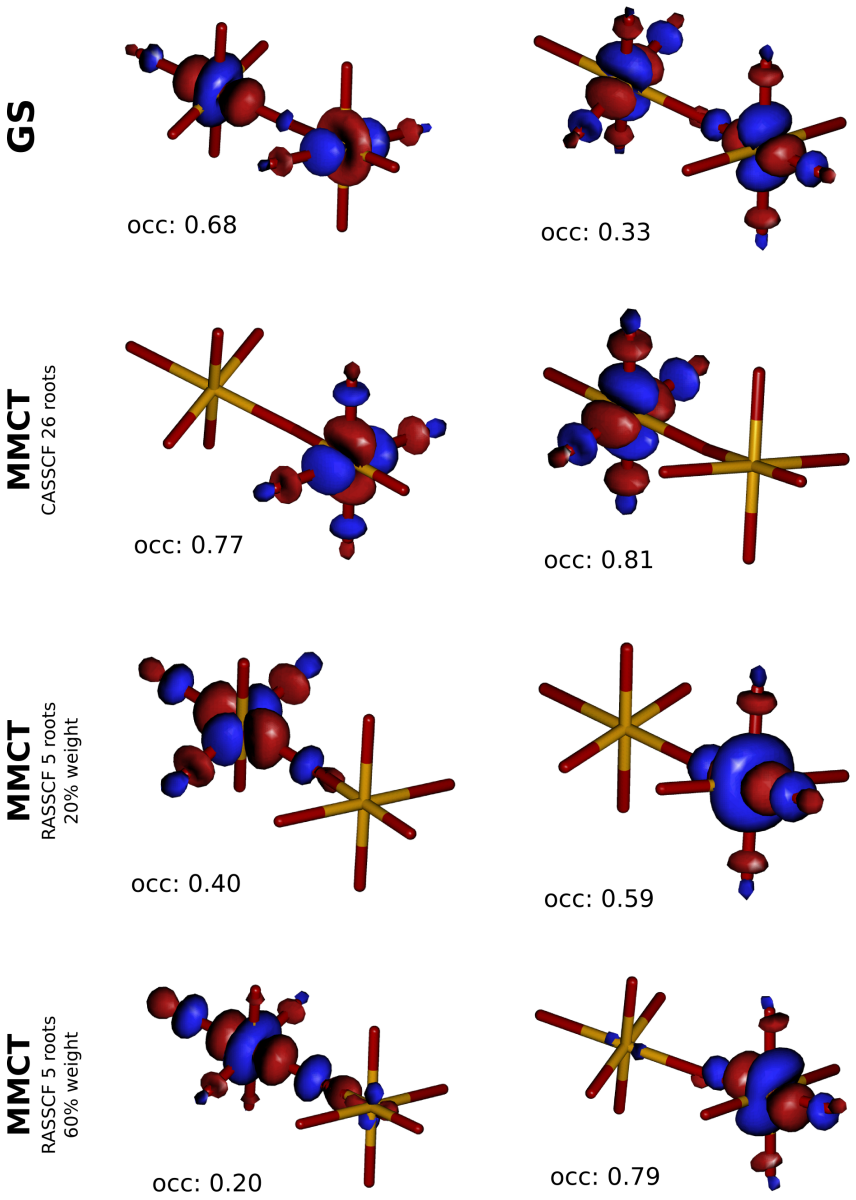

Figure 5.3: Comparison of the molecular orbitals involved in the MMCT transition on the Mn_2O_{11} cluster. The MMCT consists on an excitation from the MO on the left to the MO on the right. The average natural occupation numbers for each MO are indicated.

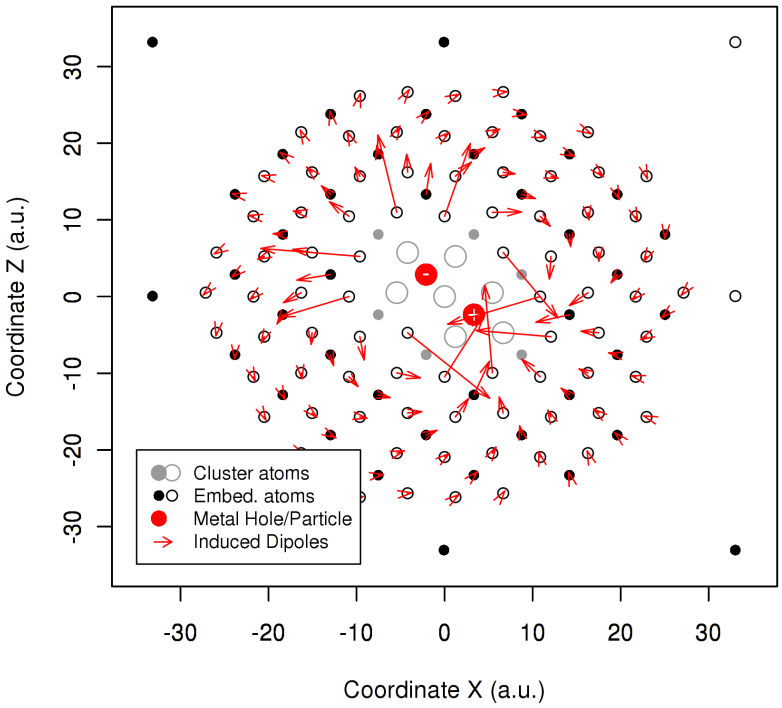

Figure 5.4: Polarization of the embedding caused by the MMCT process in $LaMnO_3$. Graphical representation of a slab of the Mn_2O_{11} embedded cluster model containing the charge transfer.

shows an improvement from 0.48, for the initial weight of 20%, to 0.54; which reflects the better quality of the reference wave function. The optimized MOs with a MMCT weight of 60% are very similar to the RASSCF state average MOs, but they show an even larger delocalization over the bridge O atom. Furthermore, there is a major differentitation on the average natural occupation number between the two orbitals, from a ratio of $4 : 6$ to $2 : 8$, better representing the charge transfer process (Figure 5.3).

The last step consisted in applying the DRF embedding to the description of the MMCT state. We computed the induced dipoles by the MMCT in the point charge distribution. However, the induced polarization in the shell of AIMPs

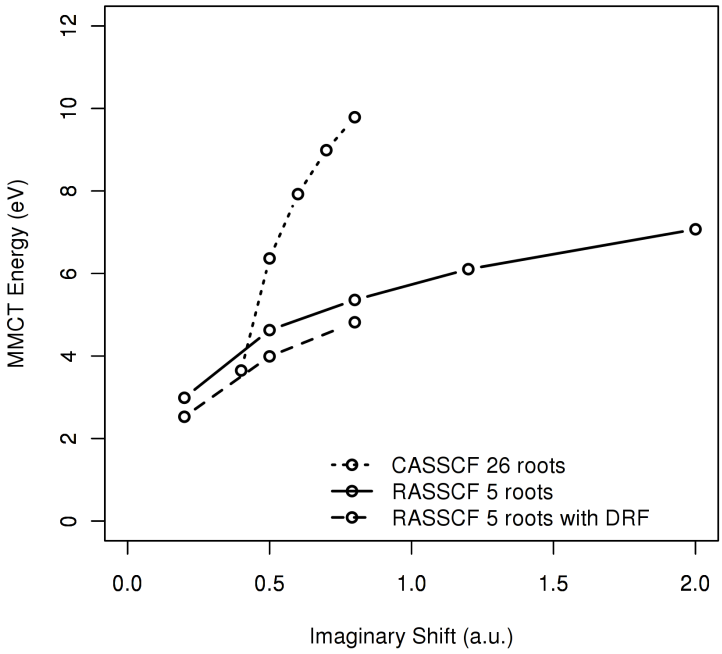

Figure 5.5: Evolution of the MMCT RASPT2 and CASPT2 energy with respect to the imaginary shift parameter. The reference of the CASPT2 is the CASSCF state average calculation of 26 roots. The reference of the RASPT2 is the RASSCF of 5 roots with a MMCT weight of 60%, with and without DRF.

could not be calculated due to technical limitations of the present implementation. Nevertheless, this approach should recover a large part of the embedding polarization, even though the largest induced dipoles will appear on the closest region to the cluster. The resulting polarization on the embedding forms a closed field around the MMCT lattice sites, analogously to other charge transfer processes (Figure 5.4). The main effect of the induced dipoles is an additional lowering of the MMCT transition energy at the RASSCF level of ~ 2 eV, to a value of 6.11 eV. This prediction of the MMCT is a big step forward, but is still largely overestimated, unfortunately. The weight of the MMCT can be lowered to practically the same proportion as with the static embedding model and the molecular orbitals have the same characteristics as the orbitals without DRF.

We have made some CASPT2 and RASPT2 calculations of the previous systems. Unfortunately, rather large level shifts are needed to obtain results that are not affected by intruder states and the excitation energies show a large dependency on the imaginary shift value. Figure 5.5 shows the evolution of the MMCT energy with respect to the variation of the imaginary shift parameter. It is obvious that the CASPT2 calculations based on the 26^{th} root of the CAS(8,20) cannot be used to, even qualitatively, estimate the MMCT energy. The RASPT2 energies behave slightly better, which reflects the better quality of the reference wave function in these cases. For smaller shifts, the inclusion of dynamical correlation tends to lower the relative energies of the MMCT state significantly. It is difficult to establish to what extent the values of 2.98 eV (without DRF) and 2.53 eV (with DRF) are affected by intruder states, but they are undoubtedly a step in the good direction. The study of MMCT in simpler systems is foreseen to better determine the precision of second-order perturbation theory estimates of the MMCT excitations.

5.4 Conclusions

We have improved the theoretical description of the MMCT transition on the prototype perovskite $LaMnO_3$. By using a RASSCF wave function that limits the major part of excitations and excited states that form the electronic structure of the system, we have been able to increase the weight of the MMCT state in the molecular orbital optimization procedure and obtain a more accurate orbital set for the description of the MMCT transition (Figure 5.3). However, the MMCT weight on the RASSCF calculation can not be raised to the ideal 100% amount due to the presence of other lower lying electronic states.

Moreover, we have improved the embedded cluster approach by incorporating responsive effects into the cluster environment to take into account the polarization of the surroundings of the MMCT transition. We used the DRF method to compute the induced dipoles on the point charge distribution, self-consistently with the RASSCF electronic structure calculations (Figure 5.4). However, it has

been unfeasible to calculate the induced dipoles on the AIMPs around the cluster, which would experience the largest polarization due to its proximity to the charge transfer region.

Nevertheless, the MMCT energy has been estimated in 6.11 eV. A larger value than the experimental measures of ~ 2 eV, but a significant step forward on the theoretical field. The RASPT2 calculations to treat the dynamical correlations effects on the system have lead to unsuccessful results though. The MMCT energy at the RASPT2 level has a too large dependency on the imaginary shift value employed. This behaviour proves that the reference wave functions obtained are not accurate enough to describe the MMCT state. Nonetheless, the RASSCF weighted average calculations have a slower variation with the increase of the shift parameter (Figure 5.5).

At this point we reached the limit of the theoretical method employed. There is no possible further improvement with the actual resources and schemes. The next steps to perform would be including the polarization on the AIMPs region, increase the MMCT state weight beyond the 60% and treat rigorously the dynamical correlation with a subsequent RASPT2 step. Another possibility open for research is to change the zeroth-order Hamiltonian used in the CASPT2 (or RASPT2) approach, which is based on a one-electron Fock-type operator, for the more rigorous zeroth-order Hamiltonian used in NEVPT2 [205–207], which has two-electron terms for the active orbitals and might give a better description of the large correlation effects.

UNIVERSITAT ROVIRA I VIRGILI
THEORETICAL DESCRIPTION OF ELECTRONIC EXCITATIONS IN EXTENDED SYSTEMS:
BEYOND THE STATIC MATERIAL MODEL
Alex Domingo Toro
DL:T. 1705-2011

CHAPTER 6

Environmental effects on organic biradicals: the exchange constant of TTTA

6.1 Introduction

The organic radical crystals have experienced an increasing scientific interest as possible building blocks of molecular materials with bistable electric and magnetic properties. Significant success was achieved with systems based on thiazyl radicals [208]. One example of this kind of neutral organic radicals is the 1,3,5-trithia-2,4,6-triazapentalenyl (TTTA), which has bistable magnetic properties and presents wide hysteresis loops in the magnetic susceptibility versus temperature curves [209, 210]. These heteroatom radicals grow three-dimensional crystalline structures formed by one-dimensional stacks of molecular dimers. The hysteresis phenomenon on TTTA involves a phase transition that consists on a slippage process on the dimers (Figure 6.1), from the diamagnetic (strong antiferromagnetic) phase at the low temperature (LT) regime to the antiferromagnetic phase at the high temperature (HT) regime. The main characteristic of the electronic structure of these materials is the delocalization of an unpaired electron over the whole radical. These unpaired electrons are antiferromagnetically coupled to neighbouring radicals in the ground state. The modifications of the stacking of the radicals upon the phase transition strongly weakens the exchange interaction. These properties confer to TTTA and similar organic biradicals the possibility to be multifunctional materials acting as both conductors and magnetically active materials.

The existence of multifunctionality on organic radical crystals requires a balance between conductivity and magnetism. However, these two properties are guided by opposite requirements of the electronic structure parameters, making in general impossible the combination of both. To achieve conductivity the system should have a certain degree of electron delocalization, whereas the magnetism is associated with localized electrons. The conductivity along the one-dimensional chains of dimers is determined by the resonance integral ($|t|$) between the biradicals, which should be large to have delocalized electrons along the chain, and the on-site Coulomb repulsion (U), which should be low to not enter into an insulating state. Typically, these two parameters are related in conducting systems through the bandwidth (W) of the conduction band as $W \approx 4|t| \approx U$.

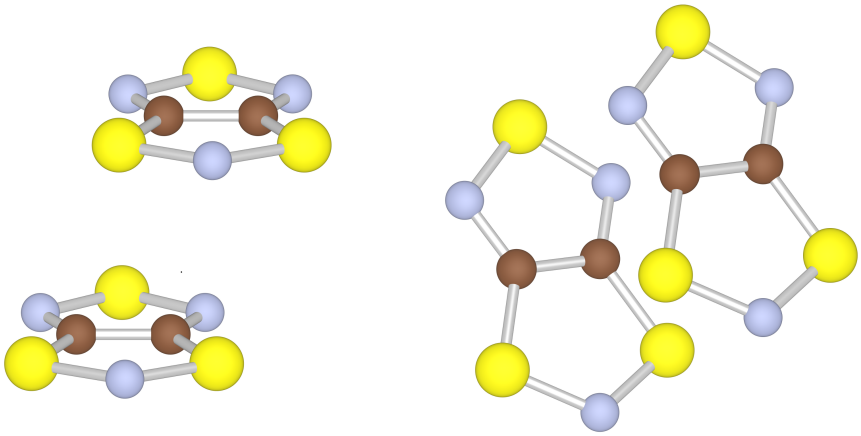

Figure 6.1: Structure of the TTTA dimer in the HT crystalline phase. C atoms are represented in brown, N atoms in grey and S atoms in yellow. Left: Front view showing the slipped packing of radicals (1.32 Å). Right: Side view from the top, the distance between the two radicals is 3.46 Å.

On the other hand, the magnetism of the these organic radical crystals depends on the singlet–triplet splitting of the dimers, which is determined by the exchange coupling constant (J). Using the standard definition of the Heisenberg Hamiltonian ($H = -JS_1S_2$), the J value of the organic biradicals is usually negative with $-4t^2/U$ as the main contribution. To obtain an effective magnetic behaviour, J should compete with room-temperature resulting in an approximate value $4t^2/U \approx k_BT \approx 200$ cm^{-1}. The combination of the two former qualitative derivations leads to a simple rule for multifunctional materials of $|t| \approx 200$ cm^{-1} and $U \approx 800$ cm^{-1}. Therefore, the research of this kind of materials can be reduced to finding an organic biradical that fulfils the previous requirements for $|t|$ and U. [211]

The experimental exchange coupling J of TTTA is measured on the HT regime to be -222 cm^{-1} [209]. This value reflects the magnetization of the material upon the LT–HT transition. However, theoretical calculations of the $|t|$ and U parameters of TTTA resulted in too large values that, based on the derived rule

by Vérot *et al.* [211], discarded this compound as a feasible building block for multifunctional materials. Therefore, the present work focuses on the magnetic properties of this organic biradical. We apply state-of-the-art electronic calculations by means of the Complete Active Space Self-Consistent Field Second-Order Perturbation theory (CASPT2) [32, 34] method and the Difference Dedicated CI (DDCI) [212] method to theoretically describe the electronic structure of a TTTA dimer and estimate the singlet–triplet splitting (J). Additionally, we explore the possible effects of the crystalline environment to the electronic structure of the dimer. The changes in the electronic structure upon the singlet–triplet excitation are of course small and it is not expected that this will induce largely different dipoles in the surrounding. However, the quantity we are aiming for is also very small, and the effect of polarization in J has never been quantified so far. We incorporate responsive effects on the dimer surroundings by means of the Direct Reaction Field (DRF) [166–168] method.

6.2 Computational Scheme

The DDCI method offers a variational treatment of the dynamical correlation by expanding a model space defined to describe the states of interest. Typically, the model space is the complete active space of a previous Complete Active Space Self-Consistent Field (CASSCF) [32] calculation and the expansion is defined by all single and double excitation with respect to this model space. A large saving of computational time is obtained by eliminating the double excitations from inactive to virtual orbitals, which are the most numerous but give up to second order perturbation theory identical energy contributions to all states in the model space. In this regard, we performed a CASSCF calculation for the lowest singlet and the lowest triplet states of a TTTA dimer in vacuum. The active space contains the two unpaired electrons in the two molecular orbitals (MO), the so-called magnetic molecular orbitals. Each magnetic MO has π character and is localised on one of the radical molecules of the dimer. The basis sets employed are of the atomic natural orbital type including scalar relativistic effects (ANO-RCC). The S atoms have a contracted set formed by (5s,4p,2d)

basis functions and the C and N atoms have a contracted set with (3s,2p,1d) basis functions [45]. Hence, a subsequent DDCI step is applied on top of the resulting set of CASSCF MOs. Additionally, we performed a CASPT2 calculation using as reference the resulting CASSCF wave function. We offer the estimates of J resulted from the DDCI and CASPT2 calculations. The electronic structure calculations were carried out with the MOLCAS 7 [48, 49] package and the CASDI [213] code.

Furthermore, we performed a second set of calculations extending the material model with 320 induced dipoles centred on the lattice positions surrounding the biradical explicitly considered. The singlet–triplet transition produces a change on the total spin of the system that can induce a response phenomenon on the immediate environment of the dimer. The DRF is incorporated self-consistently with the DDCI calculations. The basic scheme of application is similar to that of the CASSCF calculations employed for Nickel Oxide (chapter 4) and $LaMnO_3$ (chapter 5) systems. The first step consists in the DDCI calculation of the electronic state without any induced polarization; the resulting set of natural orbitals is used to calculate the electric field on the embedding region; the DRF method is applied to compute the induced dipoles on the environment; and the DDCI calculation is repeated but including the induced polarization. The whole process is iteratively performed until the energy value of the involved electronic state remains constant. The induced dipoles by the singlet and triplet state can be calculated for each state separately due to the difference in spin multiplicity between them. Thus, avoiding many of the complications found for charge transfer excited states.

A draw-back of the proposed scheme is that the environmental effect cannot be separated from the improvement of the optimization of the orbitals caused by the inclusion of dynamical correlation effects. The subsequent DDCI calculations and construction of natural orbitals to calculate the induced dipoles in the environment also leads to an optimal set of orbitals of dynamical correlation on the biradical, the so-called iterative DDCI scheme introduced by García *et al.* [214]. Therefore, we also performed the CASPT2 calculations with the DRF

embedding to be able to analyse the contribution coming exclusively from the environmental effects.

The DRF method requires to define the atomic polarizability of each atom in the system. We used atomic static polarizabilities for the neutral atoms of TTTA, setting $\alpha_C = 1.630$ Å^3 for the C atoms [215], $\alpha_N = 1.098$ Å^3 for the N atoms [45] and $\alpha_S = 2.904$ Å^3 for the S atoms [215]. The DRF calculations were performed with the DRF90 software [177].

6.3 Results

The DDCI J splitting value of TTTA in vacuum is estimated to be -125 cm^{-1}. This result is crearly understimated compared to the experimental measures of -222 cm^{-1} given by Fujita *et al.* [209]. On the other hand, the J splitting value including the environmental response to the spin change is -189 cm^{-1} at the DDCI level, which represents a large improvement over the calculation in vacuum. Thus, the adaptation of the surroundings of the dimer to the singlet–triplet transition and the orbital optimization under the effect of dynamical electron correlation turns out to have a significant role in the electronic structure of these organic radical crystals. The largest induced dipoles in the crystalline surroundings by the singlet–triplet transition are approximately 4 mD, a much lower value than the polarization observed for charge transfer processes in ionic crystals, which is expected given the small differences in electronic structure between the singlet and triplet states.

The J splitting value resulted from the CASPT2 calculation of TTTA in vacuum is -160 cm^{-1} and the inclusion of the induced polarization improves this value to -167 cm^{-1}. The environmental effects derived from the CASPT2 calculation show a much lower impact on the exchange coupling J than compared with the iterative DDCI calculations with DRF, which demonstrates that the major improvement of the iterative DDCI calculation is gained from the orbital optimization under the effect of dynamical electron correlation. Nevertheless, the low environmental effects exist and we predict a effect of the order of ~ 10 cm^{-1} for the TTTA biradical.

6.4 Conclusions

We have combined self-consistently the DDCI electronic structure calculations with the DRF method to incorporate the environmental effects on the system model. We have applied the presented procedure to the calculation of the exchange coupling constant J of an organic biradical that presents bistable magnetic phenomena, the TTTA. The resulting J value with a DRF embedding (-189 cm^{-1}) is in better agreement with the experimental value than the result obtained from the calculation in vacuum (-125 cm^{-1}). This large improvement is mainly ascribed to the orbital optimization under the effect of dynamical electron correlation produced in the iterative DDCI procedure. The application of DRF to the CASPT2 calculations of TTTA resulted in a much lower change of J (7 cm^{-1}). Confirming the low effect that environmental polarization will have on the singlet–triplet splitting, which was expected due the small change in the electronic structure between those states.

UNIVERSITAT ROVIRA I VIRGILI
THEORETICAL DESCRIPTION OF ELECTRONIC EXCITATIONS IN EXTENDED SYSTEMS:
BEYOND THE STATIC MATERIAL MODEL
Alex Domingo Toro
DL:T. 1705-2011

CHAPTER 7

Ab initio study of the absorption spectrum of the spin crossover compound $Fe^{II}(bpy)_3$ including thermal motion effects

7.1 Introduction

Bistable systems with fast switching between long-lived states are a focus of research. A material capable to undergo a rapid and stable magnetic or electric change at room temperature has multiple technological applications, like nano-switches, nano-sensors or as memory devices. The two accessible states of bistable systems are the fundamental state and a metastable excited state. These states have distinct electronic properties that in many cases involve a spin rearrangement between a low spin configuration (LS) and a high spin configuration (HS). These electronic alterations due to the LS–HS switch induce in certain cases important distortions on the structure of the compound and can change its magnetic or electric properties. The direct transition from the LS to the HS state can be triggered by a variation in temperature or pressure if the relative energy between those states is of the order of k_BT. Otherwise, a more powerful approach is to produce the switch by light radiation. Some examples of photo-induced phenomena on bistable systems are the magnetization of Prussian blue analogues [1, 2, 5, 216–220], cyanomolibdates [1, 2, 203, 221–223] and Fe^{2+} complexes [3, 4, 224].

The Spin Crossover phenomenon (SCO) on quasi-octahedral d^6 Fe^{2+} complexes produces a transition from a singlet LS diamagnetic state (^1A) to a quintet paramagnetic HS state (^5T). Hence, the electronic configuration of the Fe metal changes from (t^6e^0) to (t^4e^2) with a total spin increase of 2 and magnetizing the compound. The LS→HS process can be triggered by illumination with light in the so-called Light Induced Excited State Spin Trapping (LIESST) process [4]. The decay of the excited singlet state to the metastable HS state is a fast process that can take place in less than 1 ps ($\sim$ 200 fs in $[Fe(bpy)_3]^{2+}$). The relaxation time from the HS state back to the initial LS state varies from nanoseconds to several days, depending on the energy difference between HS and LS and the environmental effects. In crystalline compounds with large collective effects the relaxation is much more slower than for complexes in solution. The metastable HS system can also be switched back to the LS state by light radiation, through the reverse-LIESST mechanism. However, the ultrafast LIESST is a complex

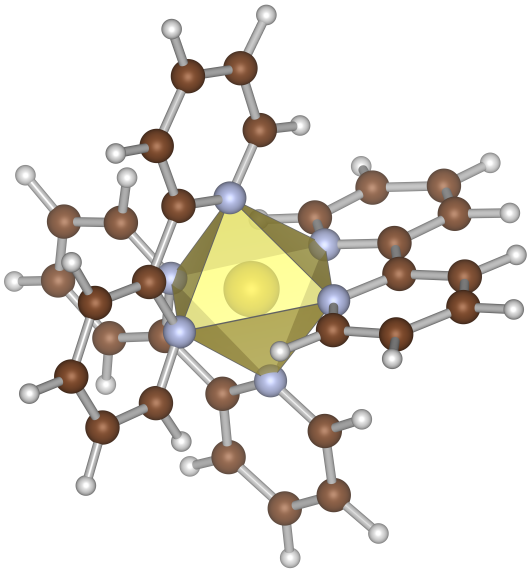

Figure 7.1: Equilibrium LS structure of $[Fe(bpy)_3]^{2+}$ complex. The Fe^{2+} metal atom is hexa-coordinated to three bipyridine ligand molecules in a pseudo-octahedral environment.

process that involves several excited states and the elongation of the Fe–ligand bond. Understanding the underlying steps of this mechanism is paramount to be able to comprehend the bistable properties of Fe^{2+} complexes and design future technological compounds.

There has been significant advances on the research about the LIESST process on the $[Fe(bpy)_3]^{2+}$ (bpy=bipyridine) SCO complex (Figure 7.1) [225–227] and related compounds [228–232]. The spectroscopic measurements using UV transient absorption experiments [225] and femtosecond XANES [227] showed the primordial role of metal-to-ligand charge transfer (MLCT) states. Upon light absorption, a spin allowed transition occurs from the LS $^1A_1$ state to a ^{1}MLCT state, exciting an electron from a Fe(t_{2g}) orbital to a ligand(π^*) orbital. The inter system crossing (ISC) between the ^{1}MLCT and ^{3}MLCT states on the surroundings of the Frank-Condon region is extremely fast, occurring in a 15–20 fs

time scale [225, 227]. The global transition from the LS $^1A_1$ state to the HS $^5T_2$ state in the case of $[Fe(bpy)_3]^{2+}$ takes less than 1 ps with a quantum efficiency of nearly 100% [225]. Nevertheless, the possible decay paths from the ^{3}MLCT to the $^5T_2$ state are diverse. It has been proposed a multiple step decay through the ligand-field manifold of states in the HS region [225]; a direct transition from the ^{3}MLCT to the $^5T_2$ state in the timescale of a Fe–N stretching ($\sim$ 150 fs) [227, 231, 233]; or by means of a ^{5}MLCT intermediate state, based on the ultrafast cascade decay theory [234, 235].

The electronic structure calculations of Fe^{2+} compounds are a helpful tool to disclose the details of a complex process like LIESST. However, the theoretical method must deal with some difficulties inherent to these phenomena. The first one is the size of the system. The Fe^{2+} SCO complexes have relatively large aromatic ligands, which make the molecule total more than 50 atoms typically. Therefore, the first theoretical calculations of the electronic structure of Fe^{2+} complexes were based on the Density Functional Theory (DFT). The thermodynamic properties and vibrational modes were calculated and analysed [12, 14, 236, 237]. The energy difference between LS $^1A_1$ and HS $^5T_2$ was estimated by many different functionals, detecting some dependencies of the results on the functional employed [15, 18–20, 23]. Subsequent DFT calculations also dealt with excited states [238, 239].

The excited states in the LIESST process often appear mixed and with significant multi-configurational character. Thus, the theoretical description of these states and the transitions between them is not simple to achieve. *Ab initio* wave function based methods offer a powerful tool to perform such studies without any *a priori* assumptions. The application of these methods on various Fe^{2+} complexes proved to correctly reproduce the energetics between the ligand-field states and their variation along the Fe–N bond distortion [26, 30]. The ligand-field triplet states were suggested as possible mediators in the transition, because they cover the gap between the LS and HS regions and cross the LS $^1A_1$ and HS $^5T_2$ states [31]. Subsequent theoretical research on the LIESST mehanism confirmed the key role of the MLCT states, as exposed by the experimental measurements. The fact that the ^{1}MLCT and ^{3}MLCT have the same

electronic configuration ($t_{2g}^5 e_g^0 \pi^{*1}$) and, hence, similar energies and optimal geometries, leads to a large coupling between these CT states favouring the ultrafast ISC [240, 241]. Therefore, the known steps of the LIESST mechanism are $^1A_1 \rightarrow {}^1$MLCT $\rightarrow {}^3$MLCT $\rightarrow {}^5T_2$, but the details of the last ^{3}MLCT $\rightarrow {}^5T_2$ transition step are still not clear. A part from the role of quintet MLCT states, there are other additional determining factors. The effect of vibrational modes on the LIESST has been studied [233] and found to be a necessary ingredient in the description of some ligand-field states crossing [7]. Furthermore, the environmental effects cannot be completetly discarded, despite of the large size of these coordination complexes [231, 232, 242, 243]. The effect of the surroundings of the metal atom were also investigated, like the effect of the σ-donation of different ligand molecules [244]; and the charge reorganization on crystalline environments that leads to hysteresis [245].

The aim of the present work is to continue developing the *ab initio* approach to provide a more complete description of the LIESST process on the $[Fe(bpy)_3]^{2+}$ complex. By combining *ab initio* molecular dynamics (MD) simulations with highly correlated electronic structure wave function calculations, we include the vibrational degrees of freedom on solvent into the electronic structure calculations. We use the Car-Parrinello molecular dynamics (Car-Parrinello MD) [102] to explore the LS ground state potential energy surface of $[Fe(bpy)_3]^{2+}$ in water. Subsequently, we calculate the electronic structure of a representative sample of the simulation with the Complete Active Space Self-Consistent Field Second-Order Perturbation theory (CASPT2) [32, 34], which has proven very efficient in treating both the static and dynamic electron correlation on Fe^{2+} complexes [7, 26, 30, 31, 240, 241, 244]. Thus, we obtain a richer description of the electronic structure of the $[Fe(bpy)_3]^{2+}$ compound that is not limited to the one-dimensional Fe–N bond distortion and also includes the conformational space of the molecule in water.

7.2 Computational Scheme

Molecular Dynamics

We performed a Car-Parrinello MD simulation of the $[Fe(bpy)_3](Cl)_2$ complex in water. The system cell has 21.00 Å of side length, containing 298 water molecules, one $[Fe(bpy)_3]^{2+}$ molecule and two Cl^- counter-ions. We based our Car-Parrinello MD simulations on the previous work by Lawson Daku *et al* [243]. The core electrons are described by Troullier-Martins normconserving pseudopotentials [104]. The electronic potential was calculated by means of the BLYP density functional [105, 106] using a plane waves basis set with a cut-off of 80 Ry. The system was first equilibrated at 300 K and then maintained at a steady temperature with a Nosé-Hoover chain thermostat [107, 108]. All hydrogen atoms are deuterium isotopes to avoid the higher frequency hydrogen stretchings and be able to use a relatively large fictitious electron mass of $\mu = 700$ a.u., which combined with a time step of 0.097 fs ensures the proximity to the Bohr-Oppenheimer potential surface during the simulation [109]. We extracted four conformational structures from a trajectory of 1.5 ps. The MD simulations were carried out with the CPMD software version 3.15.

Figure 7.2 shows the thermal distribution of the six Fe–N bond distances along the Car-Parrinello MD simulation. The average Fe–N bond length during the molecular dynamics is 1.977 Å, which is in very good agreement with the crystallographic measurement of 1.967 Å at 293 K [246]. The variation of the Fe–N bond lengths spans from 1.90 Å to 2.05 Å, completely covering the minimum of the LS state and a large part of its surroundings. This range of distortion appears to be sufficient to extract a representative sample of conformations from the MD trajectory and explore the classically accessible LS state at 300 K.

Figure 7.3 shows the thermal distribution of the twelve N–Fe–N' angles along the Car-Parrinello MD simulation. Two main types of N–Fe–N' angles can be observed on the thermal distribution, the bipyridine bite angle and the inter ligand

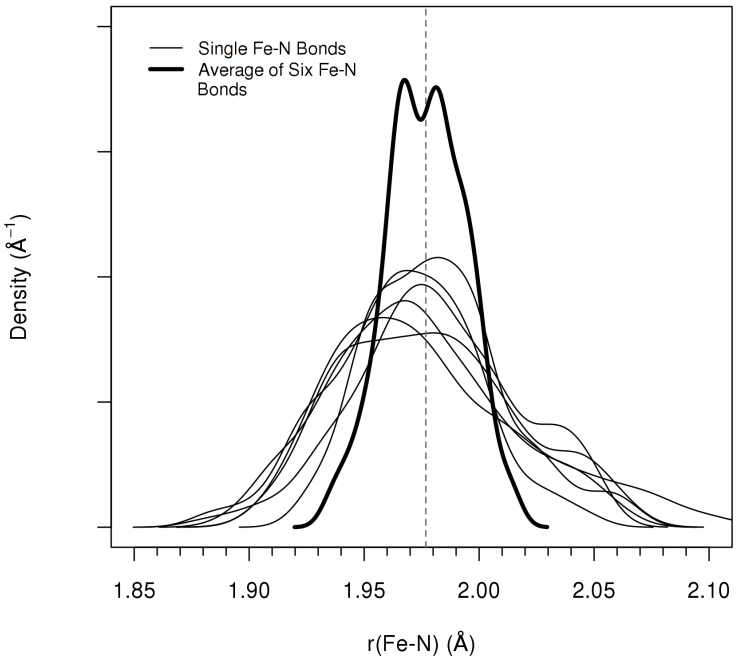

Figure 7.2: Thermal distribution of the six Fe–N bond lengths of $[Fe(bpy)_3]^{2+}$ complex resulting from the molecular dynamics simulation. Each bond is represented by a thin line and the average of the six bonds by a thick line. The mean value of the average Fe–N bond along the simulation is 1.977 Å (dashed line).

angles. The differences between the metal–ligand bond angles of the $[Fe(bpy)_3]^{2+}$ compound demonstrates the distortion of the Fe metal atom coordination sphere in a non-octadrehal environment. The performed molecular dynamics is capable to reproduce this trait of the $[Fe(bpy)_3]^{2+}$ complex and, additionally, achieving a very good agreement with the experimental crystallographic measures. The average value of the bite angle along the MD trajectory is 81.4°, whereas the measured bite angle is 81.3° [246]. The inter ligand angles show a wider range of values, but two main regions can be distinguished at $88 - 89°$ and $\sim 95°$, which correspond to the two different inter ligand angles of the ideal structure. Furthermore, the mean value of the three N–Fe–N' angles between opposed Fe–N bonds is 173.2°.

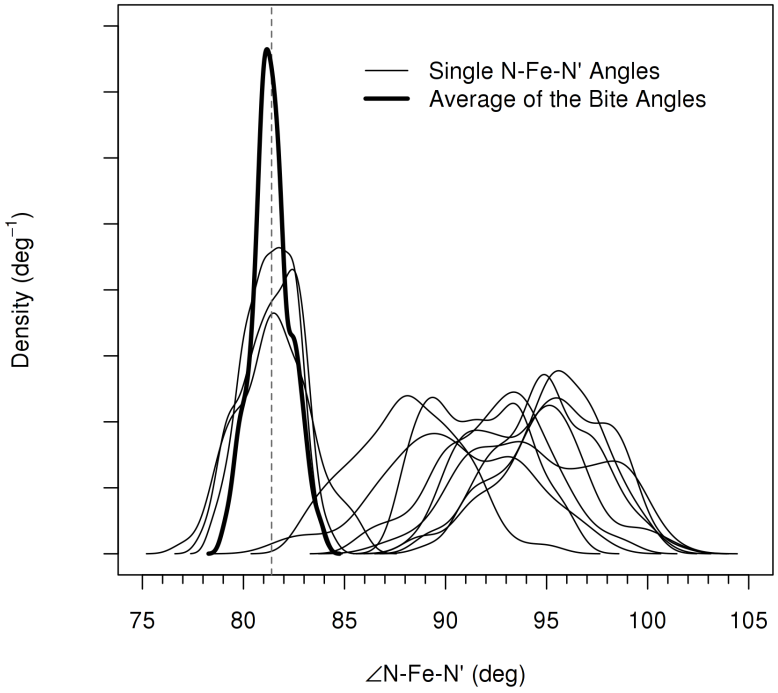

Figure 7.3: Thermal distribution of the twelve N–Fe–N' angles of $[Fe(bpy)_3]^{2+}$ complex resulting from the molecular dynamics simulation. Each angle is represented by a thin line. The average of the three bite angles of the bpy ligand is represented by a thick line. The mean value of the average three N–Fe–N' bite angles along the simulation is 81.4° (dashed line).

Electronic Structure

We calculate the electronic structure of the four $[Fe(bpy)_3]^{2+}$ conformers extracted from the Car-Parrinello MD simulation by means of the CASPT2 method. These calculations consist in the structure of the $[Fe(bpy)_3]^{2+}$ molecule in vacuum. As a first approach, we study the effects of the solvent on the conformational space of the system through the molecular dynamics, but not on its electronic structure. The solvent effects will be incorporated into the electronic structure on a future work. Therefore, we will be able to compare which is the

main influence of the solvent in the system, by being a constraint of the conformational space or by having a direct effect on the electronic structure through solute-solvent interactions.

The purpose of the CASPT2 calculations is to obtain an accurate description of both ligand-field and MLCT states of $[Fe(bpy)_3]^{2+}$. Thus, the active space of the system incorporates both metal and ligand molecular orbitals (MO). These are five Fe(3d) orbitals and five Fe(4d–like) orbitals that are more diffuse and necessary to treat the radial correlation. Two σ orbitals mainly localized on the N atoms and pointing to the Fe–N bond direction, which will introduce the σ-donation, and three π^* orbitals delocalized on the bipyridine ligands, which are necessary to include MLCT states in the electronic structure and account for the π-back donation. In total this builds up as a CAS(10,15) with ten electrons distributed in fifteen orbitals.

Moreover, due to the conformational distortions of the system we cannot impose any symmetry restriction on the electronic structure. We computed the 12 lowest singlet excited states of the system, which on a ideal scenario will result in three T ligand-field states plus three ^{1}MLCT states, one for each π^* orbital. The CASPT2 calculations were performed with an imaginary level shift of 0.2 a.u. to eliminate possible intruder states [113]. The interaction between the N-electron electron states by spin-orbit coupling was computed by State Interaction calculations between the ground state and all the excited states at the CASPT2 level, inserting the transition dipole operator in the Hamiltonian [114].

We use atomic natural orbital basis sets including scalar relativistic effects (ANO-RCC) to expand the one-electron molecular orbitals. We applied a contracted basis set (6s,5p,4d,2f) for the Fe atom [46], a (4s,3p,1d) for the N atoms, a (3s,2p) for the C atoms and a (2s) for the H atoms [45]. The Cholesky decomposition of the two-electron integrals was employed to reduce the computational cost [44, 204]. The electronic structure calculations were carried out with the MOLCAS 7.2 package [48, 49].

7.3 Results

Table 7.1 shows the results obtained for the four conformers extracted from the Car-Parrinello MD simulation. The calculated singlet excitations range from the 2.0 eV to the 3.1 eV in energy, which is a common characteristic of all the conformers. These four $[Fe(bpy)_3]^{2+}$ molecules have an increasing degree of distortion covering as much range as possible of the LS potential energy surface. Even though this set of structures is very small, it turns out to be large enough to reveal a clear trend on the electronic structure of $[Fe(bpy)_3]^{2+}$; the character of the lower singlet states largely depends on the structural distortions of the molecule. The conformers with a more contracted metal environment have a significant diminution of the low-lying ligand-field states in favour of the ^{1}MLCT. Therefore, as the Fe environment expands, the ligand-field states relax pushing the charge transfer states to higher energies. On the extreme case, the lowest ^{1}MLCT is the sixth excited state at 0.50 eV higher energy than the lowest charge transfer of the most compact molecule. These alterations in the electronic structure of the $[Fe(bpy)_3]^{2+}$ are rather a large change for such a small structural distortion, which consists on a variation of 0.05 Å of the average Fe–N bond length.

Moreover, the electronic structure of the $[Fe(bpy)_3]^{2+}$ complex appears as a very dense manifold of states. We have calculated 12 singlet states in a range of energy of 1.0 eV and, consequently, the energy difference between these states is typically of the order of 0.1 eV. This circumstance is one of the factors that contributes to the ultrafast LS→HS transition of $[Fe(bpy)_3]^{2+}$.

7.4 Conclusions

We have performed a complex Car-Parrinello MD simulation of the $[Fe(bpy)_3]^{2+}$ complex in a box with 298 water molecules. From this MD trajectory we extracted four conformational structures of the $[Fe(bpy)_3]^{2+}$ molecule that represent most of the LS ground state potential energy surface. The electronic structure of these four conformers has been calculated by means of the CASPT2

Table 7.1: CASPT2 energies of the lowest 12 singlet states of four $[Fe(bpy)_3]^{2+}$ conformers. The ligand-field states have a grey background and the ^{1}MLCT states have a white background. The average Fe–N bond length of the four conformers is indicated for reference.

	Conformers			
	Mean Fe–N bond length (Å)			
	1.956	1.972	1.980	1.993
State	Singlet Transition Energy (eV)			
GS	0.00	0.00	0.00	0.00
1	2.08	2.16	2.08	2.04
2	2.36	2.12	2.07	2.12
3	2.50	2.30	2.27	2.15
4	2.26	2.25	2.37	2.65
5	2.38	2.41	2.44	2.65
6	2.48	2.52	2.50	2.53
7	2.56	2.56	2.53	2.75
8	2.50	2.58	2.64	2.70
9	2.58	2.63	2.70	2.73
10	2.57	2.62	3.06	2.69
11	2.62	2.66	3.13	2.91
12	2.82	2.92	3.07	2.98

method. The results of the 12 lowest singlet states reveal a strong dependency of the ligand-field states and the ^{1}MLCT with the size of the Fe environment (Table 7.1). The molecules with a lower Fe–N average bond length favour the stabilization of the ^{1}MLCT states, whereas the conformers with a bigger Fe environment experience a drastic relaxation of the ligand-field states, pushing the lowest charge transfer states up in energy. The gain in energy of the lowest ^{1}MLCT state is 0.5 eV, a relatively large value for a small change of 0.05 Å of the average Fe–N bond length, from the conformer with the most compact Fe environment to the largest.

The future work of this project will focus on treating a wider region of the LS region and expanding the presented theoretical procedure to the HS states of

$[Fe(bpy)_3]^{2+}$. The Car-Parrinello MD simulation of the $[Fe(bpy)_3]^{2+}$ molecule in the LS state will be extended to explore the lowest frequency vibrational effects on the conformational space. Moreover, the number of conformations will be increased to get statistically representative data about the LS potential energy surface. The triplet and quintet excited states of those conformers will be studied applying and analogous approach to the singlet states calculations. Another subject of the future research will be the solvent effects on the electronic structure, which will be incorporated into the CASPT2 calculations by means of different solvent models. To obtain the complete picture of the LIESST process it will be necessary to perform the described dynamical study of the LS region to the HS region, including the thermal motion and solvent effects.

CHAPTER 8

Conclusions

We developed a procedure to combine the benefits of the molecular dynamics techniques with the accuracy of the *ab initio* wave function based methods including the environmental effects. The results obtained on various chemical systems of different nature show a clear improvement on the theoretical description obtained. The next points summarize the most relevant conclusions of the present project:

- The inclusion of vibro-rotational degrees of freedom into the electronic structure, by means of combining molecular dynamics with *ab initio* wave function calculations, greatly improves the description of many spectroscopical properties of molecular compounds and crystalline materials, like the broadening of bands in the optical absorption spectrum and density of states.

- Working with the conformations of a system at a given temperature, instead of the ideal geometry of the compound or material, allows to calculate the absorption intensity of electronic transitions that, otherwise, are forbidden by the selection rules.

- The distorted geometries of the different conformations produce electronic states of mixed character that are difficult to directly relate to the states of the ideal structure. Furthermore, the solvent effects can also play a role on the mixed character of some states.

- The addition of some explicit solvent molecules to the quantum description of some molecular compound significantly improves the solute-solvent interactions, making possible to accurately describe the H-bond interactions, for example.

- The response phenomena of the crystalline bulk to localized charge transfer processes on a particular lattice site have a determinant role on the stabilization of the formed excitons. LMCT transitions in NiO are stabilized by ~ 2 eV upon inclusion of the polarization of the surroundings.

- The description of electronic states that largely benefit from dynamical correlation effects, like the MMCT, is deficient for state average CASSCF

calculations. It is possible to improve the description of such excited states by applying restrictions to the active space to reduce the number of states in the electronic structure and, therefore, improve the orbital description of the MMCT state.

- Spatial symmetry does not exist, it is an archetypical concept that can only simplify some specific problems in very particular occasions.

Additionally, we created various software tools to ease the calculations with the different computational methods combined in the present work. The major code developed automatically looks for a reference system model in the molecular dynamics and extracts a number of conformers, transforming the model description and adapting it to the electronic structure calculation requirements. Moreover, we also developed a script and some helping tools to incorporate self-consistently the DRF in the CASPT2 or DDCI calculations.

We achieved a significant degree of advance in the theoretical description of each chemical system studied. The research on the ligand σ-donation for SCO complexes showed the large multiconfigurational character of the electronic states of Fe^{2+} complexes and how it varies depending on the particular ligand. The computed absorption spectra of four cytosine tautomers, exploring their conformational space by means of MD simulations, revealed the undefined nature of the electronic transitions once the planar geometry is lost and the $n\pi^*$ and $\pi\pi^*$ excitations start to become strongly mixed. The calculations of NiO proved the localized nature of its electronic structure and the underlying phenomena that drives the broadening of the LMCT band, including lattice distortions and bulk polarization effects. The MMCT estimations on $LaMnO_3$ did not result in the expected values of ~ 2 eV, but served to make large improvements on the theoretical description of these states by the CASSCF/CASPT2 method. The inclusion of environmental effects on a neutral crystal like TTTA showed to have a small role for the singlet–triplet splitting (J). The electronic structure of a few conformations of the $Fe(bpy)_3$ SCO complexes resulted in a very compact manifold of states that are very dependent on the molecular distortions, which helps to explain the ultrafast ^{1}MLCT$\rightarrow^3$MLCT ISC.

UNIVERSITAT ROVIRA I VIRGILI
THEORETICAL DESCRIPTION OF ELECTRONIC EXCITATIONS IN EXTENDED SYSTEMS:
BEYOND THE STATIC MATERIAL MODEL
Alex Domingo Toro
DL:T. 1705-2011

UNIVERSITAT ROVIRA I VIRGILI
THEORETICAL DESCRIPTION OF ELECTRONIC EXCITATIONS IN EXTENDED SYSTEMS:
BEYOND THE STATIC MATERIAL MODEL
Alex Domingo Toro
DL:T. 1705-2011

APPENDIX A

Electric potential energy shift upon polarization of the embedding

The large shifts obtained for the cationic and anionic state energies of NiO using a DRF embedding (see chapter 4) can be explained by application of the Coulomb's law to a simplified model of the system. We will use a bidimensional system formed by a hole/particle (Q) surrounded by 4 point charges (q) at a distance r (Figures A.1, A.2 and A.3). The following discussion will be first focused on the electric potential instead of the electric potential energy for the sake of simplicity.

Independently of the considered process, the electric potential produced at Q by the embedding point charges is

$$V_Q(q) = \sum_i^{N_q} V_Q(q_i)$$

where the potential from each surrounding charge (q_i) can be written as

$$V_Q(q_i) = k\frac{q_i}{r}$$

In the case of adding an electron to the cluster (Figure A.1), the electric potential at Q caused by the induced dipoles on the four point charges can be written as

$$V_Q(p) = \sum_i^{N_q} V_Q(p_i) = \sum_i^{N_q} k\frac{\delta_{q+}}{r - p_{\frac{1}{2}}} + k\frac{\delta_{q-}}{r + p_{\frac{1}{2}}} > 0$$

where $p_{\frac{1}{2}} = \mid \vec{p} \mid /2$. Therefore, all $V_Q(p_i)$ are positive for isotropic polarizations ($\mid \delta_{q+} \mid = \mid \delta_{q-} \mid$) and the total electric potential upon electron addition will be

$$V_Q^{\ominus} = V_Q(q) + V_Q(p)$$

Analogously, the electric potential at Q caused by the induced isotropic polarization from the ionization (electron removal) of the site (Figure A.2) is always negative and, hence, the total potential will be

$$V_Q^{\oplus} = V_Q(q) - V_Q(p)$$

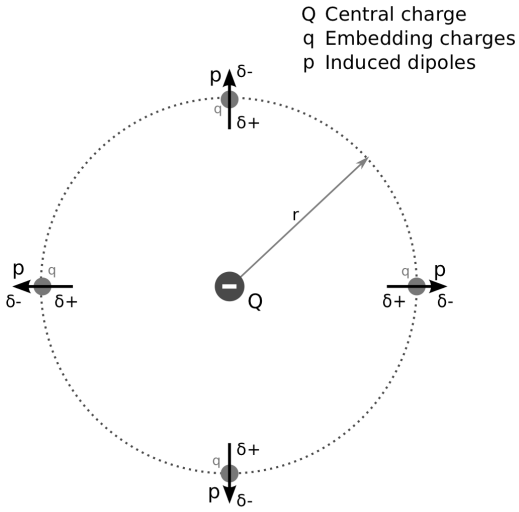

Figure A.1: Schematic representation of the induced polarization caused by a created particle (anionic state).

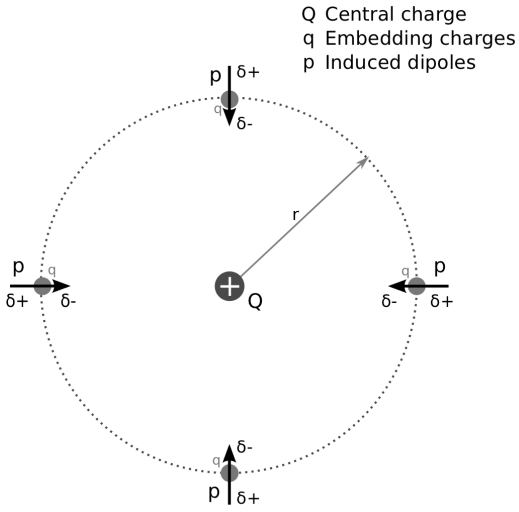

Figure A.2: Schematic representation of the induced polarization caused by a created hole (cationic state).

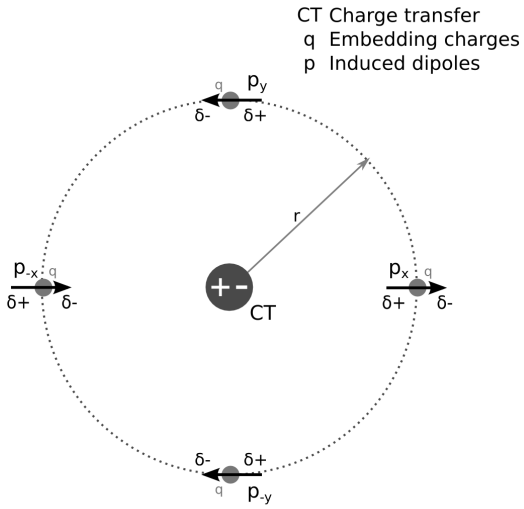

Figure A.3: Schematic representation of the induced polarization caused by a charge transfer process.

There is no such a change in potential for the LMCT process (Figure A.3). The highly localized charge transfer process in NiO generates both a hole and a particle in the cluster, producing a closed electric field around the absorption site that does not affect the electric potential of the system. The induced dipoles parallel ($V_{Q\parallel}(p)$) and perpendicular ($V_{Q\perp}(p)$) to the LMCT direction become mutually opposed and cancel each other

$$\begin{aligned} V_{Q\parallel}(p) &= V_Q(p_x) + V_Q(p_{-x}) = \\ &= \left(k\frac{\delta_{q+}}{r - p_{\frac{1}{2}}} + k\frac{\delta_{q-}}{r - p_{\frac{1}{2}}}\right) + \left(k\frac{\delta_{q+}}{r + p_{\frac{1}{2}}} + k\frac{\delta_{q-}}{r + p_{\frac{1}{2}}}\right) = 0 \end{aligned}$$

$$\begin{aligned} V_{Q\perp}(p) &= V_Q(p_y) + V_Q(p_{-y}) = \\ &= \left(k\frac{\delta_{q+}(p_y)}{r_\perp} + k\frac{\delta_{q-}(p_{-y})}{r_\perp}\right) + \left(k\frac{\delta_{q-}(p_y)}{r_\perp} + k\frac{\delta_{q+}(p_{-y})}{r_\perp}\right) = 0 \end{aligned}$$

where $r_\perp = \sqrt{r^2 + |\,\vec{p}\,|^2}$. Thus, there is no change of the total electric potential caused by the LMCT.

This situation prevents the computation of the DOS including extra-cluster polarization effects by means of the standard clusters used so far. Due to the aforementioned electric potential shifts, the electron affinity and ionization potential energies obtained including a polarizable embedding will be larger, in absolute terms, than the non-polarized counterpart. However, it is actually possible to calculate the U and Δ gaps including the polarization response of the embedding. Applying the definition of these parameters done by Zaanen *et al.* [147] the contributions to the potential from the particle and the hole mutually counterbalance

$$V_Q^{gap} = V_Q^- + V_Q^+ = V_Q(q)$$

The calculation of the electron affinity and ionization potential requires a description of the cationic, anionic and neutral states on the same potential energy background. Since the polarization caused by these three states is completely different, the only option to not drag the electric potential shift to the electronic structure calculation is to work with a neutral cluster as reference system. The electric potential energy of the central charge in the former simplified bidimensional model is defined as

$$E_Q = Q\ (V_Q(q) + V_Q(p))$$

Table A.1: Nuclear-external field potential energy for various cluster models in a polarized embedding. The polarization corresponds to a cationic state.

Cluster	Charge	Potential Energy (eV)
NiO_{14}	56+	−99.10
NiO_{38}	10+	−16.13
NiO_{38}	0	1.14

Therefore, a embedded cluster model with a total cluster charge $Q = 0$ will be capable to describe the different ionic and neutral states of the system in the same potential energy background, regardless of the polarization of the embedding. We built various cluster models to explore and test this possibility. Table A.1 shows the nuclear-external field potential energy of three different cluster models with varying global charge. For all cases we used the polarization produced by a cationic state. The cluster charge is changed by including additional model-potentials or point charges in the quantum region to compensate its charge. The results show how the interaction between the embedding dipoles and the cluster lowers to practically zero energy upon neutralizing the cluster. The lack of a complete suppression of this interaction is due to slight asymmetries in the model used; and the fact that the cluster has a determined volume. This approach opens new possible applications of DRF in future studies of ionic states in crystalline systems.

APPENDIX B

Developed Software

B.1 Molecular Dynamics to MOLCAS Interface

Name `md2cas`

Language FORTRAN95

Size 103 kB

Input Molecular dynamics trajectory. Reference structure.

Output Conformers of the reference structure and input files for the electronic structure calculations.

The `md2cas` code offers various capabilities to automate the transition from the MD step to the electronic structure calculations performed with the MOLCAS package. The user must provide a production MD trajectory and the description of the reference structure to be used in the subsequent calculation. The structure to be extracted from the MD simulation should be based on the undistorted geometry of the molecule or crystal. `md2cas` reads the reference structure and finds any distorted conformational structure on the simulation that corresponds to it.

The trajectory file must be in XYZ format. Upon reading the simulation, `md2cas` will prompt the user to define the MD time interval to be considered, the cell parameters and the number of replicas of the unit cell to be processed, making possible to extract a system model bigger than the MD cell.

The description of the system to extract from the MD simulation is read from a MOLCAS–SEWARD input file. This file contains the geometry and basis sets to be used in the electronic structure calculation. The `md2cas` program reads from this file the reference geometry of the system and generates an equivalent SEWARD input file with the structure of the conformers found in the MD simulation instead. The code is prepared to deal with systems formed by multiple molecules or an embedded cluster. However, to properly handle those different cases it

is required to add some specific keywords in the initial SEWARD file that are not part of the standard MOLCAS definition. The search algorithm is based on finding molecules, but since the concept of molecule and bond involve much human intuition, the user must group the atoms in molecules (at least one). The following snipped of code is an example of a `md2cas` input taken from the calculations on cytosine (chapter 3) and the reference system described is formed by a cytosine molecule, on its planar conformation, plus three surrounding water molecules.

```
1  &SEWARD &END
2  Title
3   Cytosine in Water Solvent (PCM + 3xH2O)
4
5  MD2CAS Start
6  MD2CAS Total 4
7  MD2CAS XField F
8
9  MD2CAS Molecule 4 0 0 0.1
10 Basis Set
11 O.ano-rcc...4s3p2d1f.
12  O1   2.1976202    1.0319263    0.0000000  Angstrom
13 End of Basis
14 Basis Set
15 C.ano-rcc...4s3p2d1f.
16  C1  -1.1509642    0.2745639    0.0000000  Angstrom
17  C2  -1.1342966   -1.1586788    0.0000000  Angstrom
18  C3   1.1536533    0.4374445    0.0000000  Angstrom
19  C4   0.0778680   -1.7309238    0.0000000  Angstrom
20 End of Basis
21 Basis Set
22 N.ano-rcc...4s3p2d1f.
23  N1  -2.3357197    0.9082575    0.0000000  Angstrom
24  N2  -0.0781323    1.0092131    0.0000000  Angstrom
25  N3   1.1850145   -0.9701827    0.0000000  Angstrom
26 End of Basis
27 Basis Set
28 H.ano-rcc...2s1p.
29  H1  -2.3365263    1.9056602    0.0000000  Angstrom
30  H2  -3.1986801    0.4142089    0.0000000  Angstrom
31  H3   2.0976378   -1.3782957    0.0000000  Angstrom
32  H4  -2.0341991   -1.7401838    0.0000000  Angstrom
33  H5   0.2215891   -2.7959081    0.0000000  Angstrom
34 End of Basis
35
36 MD2CAS Molecule 2 1 6 5.0
37 Basis Set
38 O.ano-rcc...3s2p1d.
39  O2  -2.3381460    3.9086600    0.0000000  Angstrom
40 End of Basis
41 Basis Set
```

```
42  H.ano-rcc...2s1p.
43   H6  -1.3944410    4.0758470    0.0000000  Angstrom
44   H7  -2.6545830    4.3238660   -0.8037420  Angstrom
45  End of Basis
46
47  MD2CAS Molecule 2 1 7 5.0
48  Basis Set
49  O.ano-rcc...3s2p1d.
50   O3   0.5082830    3.9659700    0.0000000  Angstrom
51  End of Basis
52  Basis Set
53  H.ano-rcc...2s1p.
54   H8   0.3299260    3.0243120    0.0000000  Angstrom
55   H9   1.4096660    4.0386470    0.3174230  Angstrom
56  End of Basis
57
58  MD2CAS Molecule 2 1 1 5.0
59  Basis Set
60  O.ano-rcc...3s2p1d.
61   O4   4.0683970   -0.7785400    0.0000000  Angstrom
62  End of Basis
63  Basis Set
64  H.ano-rcc...2s1p.
65   H10  4.0269860    0.1789650    0.0000000  Angstrom
66   H11  4.5423380   -0.9974200    0.8037420  Angstrom
67  End of Basis
68
69  RF-input
70  PCM-model
71  Solvent
72   Water
73  End of RF-input
74
75  End of Input
```

The keywords belonging to `md2cas` are clearly idetified by a preceding `MD2CAS` string. There is a main block of `md2cas` settings just after the title and before the basis sets definition. Here, the basic characteristics of the system are described, for example, the total number of molecules in the quantum region (line 6) and the presence of an embedding of point charges (line 7). Subsequently, the atoms defined in the basis set description must be grouped in molecules using the `MD2CAS Molecule` keyword (lines 9, 36, 47 and 58). This keyword accepts various parameters that determine the number of atoms in that molecule, the preferred spatial localization and the tolerance to distortions of the target structures. Following the former example, the first molecule is defined on line 9; it corresponds to the cytosine molecule, which is formed by a group of four basis sets that should be placed on the center of coordinates. The low distortion tolerance of 0.1 will

make the `md2cas` to look for the group of atoms of the MD cell that better resemble the reference structure, regardless of their location. In the case of a solvent molecule the desired behaviour is rather different. The solvent molecule defined on line 36 is a water molecule. The first three parameters set that this molecule is formed by two basis sets that should be looked for near the sixth atom of molecule one, the cytosine molecule. The large tolerance to distortion of 5.0 gives more freedom to the algorithm to chose the closest water molecule of the MD cell to the defined region, in this case a N atom of cytosine, and not the group of two H atoms and one O atom that have the most similar structure to the reference water molecule.

The procedure of finding a molecule in a box plenty of atoms starts with a guess of the first atom that forms the molecule. This first step is basically a trial and error, because it is not possible to know *a priori* which atoms belong to the molecule, unless the molecule contains some atomic elements not found in the rest of the MD cell. Once a candidate is identified, the process continues by adding successive atoms to the molecule. These atoms are selected based on their relative position to the already selected atoms in the molecule, looking for the best resemblance to the reference structure. However, the main difficulty of this search process is to properly handle false positives, which are atoms that have been already selected as part of the molecule, because their relative position is in agreement to the previous selected atoms, but their inclusion in the molecule leads to a fail to find a suitable structure based on the reference. This situation is caused by the arbitrariness of the firsts steps of the process and the algorithm needs to deal with it efficiently.

The problem of false positives is clearly shown on the hypothetical case that we were looking for one 1-bromo-3-chloropropane ($BrCH_2$–CH_3–CH_2Cl) molecule in a box with solvent. If the first guess was already selected as the central C atom and the subsequent atom in the reference structure was the C atom of the bromo-metil group, the algorithm would have a 50% chance to select the C atom of the cloro-metil or the C atom of the bromo-metil. At that step the only known information is the position of the first atom in the reference structure, the central C atom, and both remaining C atoms are at similar distances to the

central one. Therefore, the decision between those two C atoms will be mainly determined by the particular conformational distortions of the molecule. In the case where the selected atom is the C of the cloro-metil group, the search will fail some steps afterwards trying to find a Br atom bonded to the C atom of the cloro-metil group.

Figure B.1 shows a flow chart with the main steps of the search algorithm. The implemented mechanism to deal with false positives has two key points. One is checking that the local environment (radius= 5 Å) of the atom added to the conformer molecule is analogous to its counterpart of the reference structure. Limiting the distance to the surroundings of the selected atom not only ensures that the new atom corresponds to its respective atom of the reference structure, but also gives the necessary flexibility to find highly distorted conformers. However, the check of the local environment can only be performed with the already selected atoms, not exploring all the atoms present inside the local range. This limitation can still lead to a false positive. Therefore, there is a second measure to handle the situation where there are no more atoms that fit in the conformer molecule. In that case, the partial list of atoms is registered and a reverse process starts to discard the false positives. The last added atom is removed and other possible candidates are tried on that position, but never repeating two times the same atom with a partial conformer structure that already lead to a fail on some position of the reference. Each time that this process reaches a dead end the algorithm goes back one step. If the process ends discarding every single possible atom except the first guess, `md2cas` will replace the first guess and restart the search algorithm.

The structures extracted from the MD trajectory, formed by one or more molecules, are translated and rotated to the original position and orientation of the reference geometry. The aim of this step is to obtain an optimal overlap between the conformer and the reference molecule. Therefore, the electronic calculation of all extracted conformers can be performed using the same starting set of MOs, which can be the resulting MOs of a previous calculation on the undistorted structure. Being able to use a previously converged set of MOs can largely improve the computational cost of the subsequent calculations. To keep

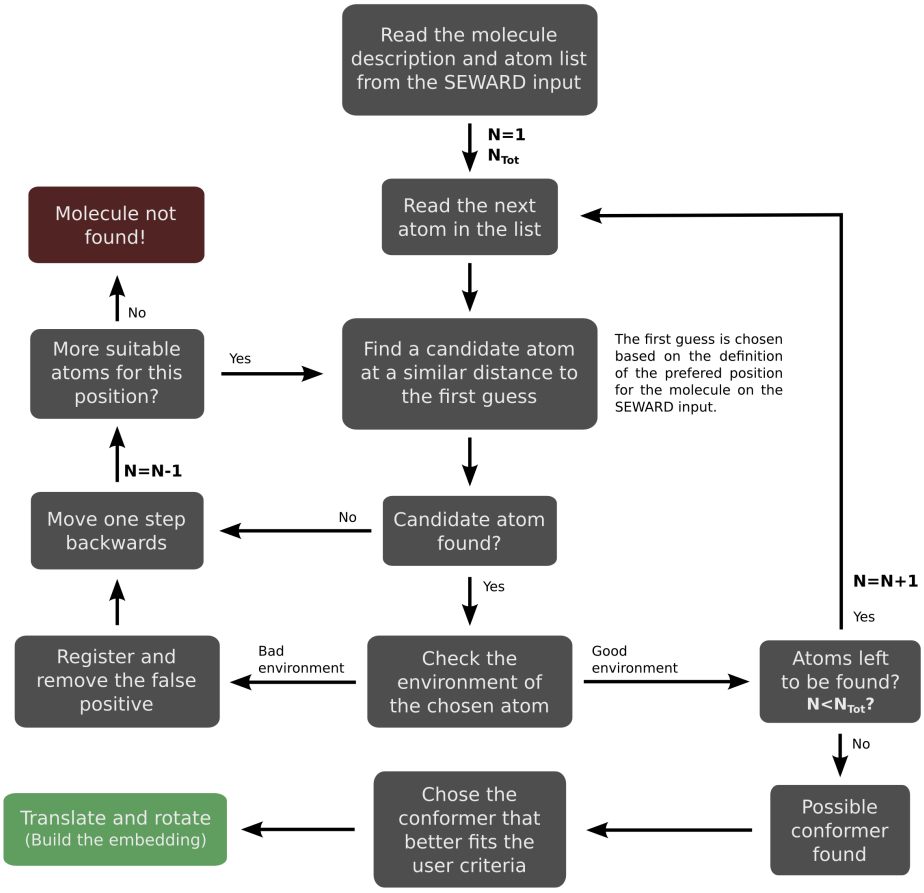

Figure B.1: Flow chart of the search algorithm implemented in `md2cas`. The N symbol represents the current atom of the reference structure that is being search. The N_{Tot} represents the total number of atoms to be found.

the relative orientation between the molecules as they are found in the MD simulation, the movement is done on the first molecule of the system (the solute molecule) and, subsequently, the rest of molecules (the solvent molecules) follow the same displacement of the first one.

The calculation of the rotation to apply to the conformer is calculated on each plane. We define the distance between two atoms, one of the ideal molecule that is fixed (r) and its analogue in the conformer that is able to rotate (p), as a function of the angle between r and p (θ):

$$|\overrightarrow{rp}| = \sqrt{(r_x - p_x cos(\theta) + p_y sin(\theta))^2 + (r_y - p_x sin(\theta) - p_y cos(\theta))^2}$$

By solving the first derivative of the former expression:

$$\frac{\eth |\overrightarrow{rp}|}{\eth \theta} = \frac{r_x(p_x sin(\theta) + p_y cos(\theta)) + r_y(-p_x cos(\theta) + p_y sin(\theta))}{\sqrt{(r_x - p_x cos(\theta) + p_y sin(\theta))^2 + (r_y - p_x sin(\theta) - p_y cos(\theta))^2}}$$

We obtain two possible θ values through:

$$tan(\theta) = \frac{-r_x p_y + r_y p_x}{r_x p_x + r_y p_y}$$

This method offers a very simple and straightforward solution to find the rotation that minimizes the distance between the atoms of the conformer and the ideal molecule without having to apply any expensive minimizing algorithm.

Furthermore, the `md2cas` program can build a distribution of point charges out of the MD cell structure following the Evjen scheme [170]. The following snipped of code shows an input file that defines the embedding in addition to the cluster of the system. This example is an actual input file used in the work of NiO (chapter 4). The user can define in the SEWARD input some additional parameters setting the presence of a distribution of charges (line 8), the length of the cubic embedding (line 9) and the formal charge of the ions in the point charge distribution (lines 10 and 11). We defined a NiO_6 cluster with six Ni–AIMPs to be preferably found in the center of coordinates with a large tolerance to distortion (line 14). Thus, the clusters extracted along the MD trajectory will

correspond to the same lattice site of the crystal, obtaining a representative set of conformations of the thermal motion effects. Otherwise, `md2cas` could extract the clusters with a better resemblance to the reference structure, which is an ideal NiO_6 cluster with O_h symmetry, nullifying any phononic distortions of the simulation. Once the cluster structure is found in the MD cell, the embedding is generated following the user settings and the formal charges are applied to each point charge. The cluster is treated as a molecule by `md2cas`. Subsequently, both the cluster and embedding are translated and rotated to coincide with the reference structure. The movement of the embedded cluster model is performed in the same manner as for a (group of) molecule(s).

```
 &SEWARD &END
Title
 NiO

MD2CAS Start
MD2CAS Total 1

MD2CAS XField T
MD2CAS EmbeBox 12.5 1.0 2 T
MD2CAS Element O Ni
MD2CAS FormChg -2.0 2.0
MD2CAS DRF T

MD2CAS Molecule 3 0 0 5.0
Basis Set
Ni.ano-rcc...5s4p2d1f.
 Ni 0.00 0.00 0.00
End of Basis

Basis Set
O.ano-rcc...3s2p1d.
 O1  3.9343  0.0000  0.0000
 O2  0.0000  3.9343  0.0000
 O3  0.0000  0.0000  3.9343
 O4 -3.9343  0.0000  0.0000
 O5  0.0000 -3.9343  0.0000
 O6  0.0000  0.0000 -3.9343
End of Basis

Basis Set
Charge
2.0000
Ni.ECP.Seijo.14s11p.1s1p.0e-AIMP-NiO
 Ni1  7.8686  0.0000  0.0000
 Ni2  0.0000  7.8686  0.0000
 Ni3  0.0000  0.0000  7.8686
 Ni4 -7.8686  0.0000  0.0000
```

```
38    Ni5  0.0000 -7.8686  0.0000
39    Ni6  0.0000  0.0000 -7.8686
40   End of Basis
41
42   End of Input
```

The extracted structures from the MD simulation are written to individual files in SEWARD format. `md2cas` also copies all other required input files to perform the electronic structure calculation on each conformer and offers the possibility to include specific input files for a self-consistent DRF step, which is controlled through an specific keyword (line 12).

B.2 Self-Consistent DRF on MOLCAS Scripts

We have developed a procedure to calculate localized electronic transitions taking into account the polarization of the transition environment. A basic scheme of the computational steps to perform is presented on Figure B.2. The main block of the process is the `SC-CASDRF`, which self-consistently integrates the electronic calculations of the quantum region with the calculations of the polarization in the embedding. A piece of `SC-CASDRF` is the `cas2drf` code, which gathers the results from the electronic structure part and generates the inputs to compute the corresponding polarization. The last step of the procedure involves the `drfembtext` program, which performs the necessary corrections to the calculated polarizations.

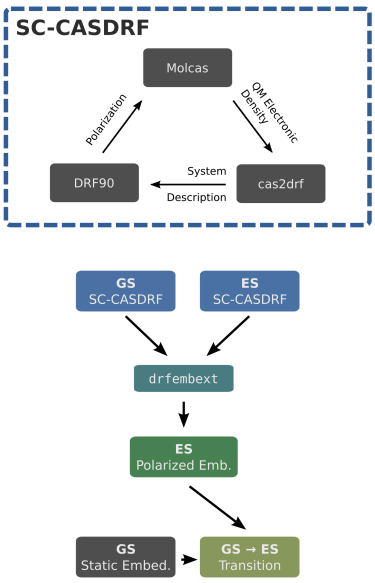

Figure B.2: Flow chart of the self-consistent implementation of DRF in MOLCAS through the DRF90 software and other tools developed for this purpose.

Name `SC-CASDRF`

Language Shell Script

Size 9 kB

Input Electronic structure calculation inputs. Atomic polarizability data.

Output Embedding or solvent with induced dipoles by an electronic transition of the quantum region. Electronic structure including the induced dipoles.

We developed a script to include the effect of the polarization on the system surroundings caused by electronic transitions localized in the quantum region. This is done in a procedure in which the induced dipoles on the environment and the electronic structure of the quantum region are brought to self-consistency. The induced dipoles are computed by means of the DRF90 code and the DRF method. The electronic structure calculations are performed with the MOLCAS packages and the CASSCF method. The script iteratively performs three steps: a state average CASSCF calculation; the calculation of the electric field produced in the embedding; and the computation of the induced dipoles in the embedding. Subsequently, the first step is repeated including the new polarized embedding. The self-consistency is achieved once the difference in energy of the excited state of interest is below certain threshold defined by the user.

Name `cas2drf`

Language FORTRAN95

Size 27 kB

Input Embedding and quantum region structure. Electric field on the environment. Atomic polarizability.

Output Input file to perform the DRF calculation by means of the DRF90 code.

The `cas2drf` tool automatically generates the input file for the DRF90 program at each step of the self-consistent integration between the CASSCF and DRF methods. This code is a necessary part of the `SC-CASDRF` script. `cas2drf` reads various input files compiling the required information to calculate the induced dipoles through DRF, including the cluster and embedding geometries; the electric field on the environment produced by the quantum region electronic density; and the polarizability values of the embedding ions or solvent molecules.

Name `drfembext`

Language FORTRAN95

Size 14 kB

Input Induced dipoles by the electronic ground state. Induced dipoles by the excited state of interest.

Output Induced dipoles by the excited state of interest after removing cluster model artefacts and state average limitations.

The generation of the final DRF embedding is performed using the `drfembext` program. This code reads the induced dipoles by two electronic states of the system, the ground state which should no produce any dipoles in the embedding and some excited state which is the responsible for the induced polarization. Taking these two polarized embeddings, `drfembext` removes the cluster model artefact polarization, using the ground state data, and generates, through a linear extrapolation, the dipoles induced solely by the excited state of interest. The newly produced DRF embedding is used in a last electronic calculation to obtain the whole relaxation of the excited state.

Bibliography

[1] O. Sato, *Photoinduced magnetization in molecular compounds,* J. Photoch. Photobio. C **5**, 203 (2004).

[2] A. Bleuzen, V. Marvaud, C. Mathoniere, B. Sieklucka, and M. Verdaguer, *Photomagnetism in Clusters and Extended Molecule-Based Magnets,* Inorg. Chem. **48**, 3453 (2009).

[3] P. Gütlich and H. A. Goodwin, *Spin Crossover—An Overall Perspective,* in *Spin Crossover in Transition Metal Compounds I*, Vol. 233, edited by P. Gütlich and H. A. Goodwin (Springer Berlin / Heidelberg, 2004) Chap. Topics in Current Chemistry, pp. 1–47.

[4] A. Hauser, *Light-Induced Spin Crossover and the High-Spin→Low-Spin Relaxation,* in *Spin Crossover in Transition Metal Compounds II*, Vol. 234, edited by P. Gütlich and H. A. Goodwin (Springer Berlin / Heidelberg, 2004) Chap. Topics in Current Chemistry, pp. 155–198.

[5] H. Tokoro, S.-i. Ohkoshi, T. Matsuda, and K. Hashimoto, *A Large Thermal Hysteresis Loop Produced by a Charge-Transfer Phase Transition in a Rubidium Manganese Hexacyanoferrate,* Inorg. Chem. **43**, 5231 (2004).

[6] P. Gütlich, H. A. Goodwin, J.-P. Tuchagues, A. Bousseksou, G. Molnár, J. McGarvey, and F. Varret, *The Role of Molecular Vibrations in the Spin Crossover Phenomenon,* in *Spin Crossover in Transition Metal Compounds III*, Vol. 235 (Springer Berlin / Heidelberg, 2004) Chap. Topics in Current Chemistry, pp. 85–103.

[7] B. Ordejón, C. de Graaf, and C. Sousa, *Light-Induced Excited-State Spin Trapping in Tetrazole-Based Spin Crossover Systems,* J. Am. Chem. Soc. **130**, 13961 (2008).

[8] O. Sato, A. Cui, R. Matsuda, J. Tao, and S. Hayami, *Photo-induced Valence Tautomerism in Co Complexes,* Accounts Chem. Res. **40**, 361 (2007).

[9] P. Gütlich, P. J. van Koningsbruggen, and F. Renz, *Recent advances of Spin Crossover research,* in *Optical Spectra and Chemical Bonding in Transition Metal Complexes*, Vol. 107, edited by T. Schönherr (Springer-Verlag, 2004) Chap. Structure and Bonding, pp. 27–75.

[10] A. Hauser, *Ligand field theoretical considerations,* in *Spin crossover in Transition Metal Compounds I*, Vol. 233, edited by P. Gütlich and H. A. Goodwin (Springer Berlin / Heidelberg, 2004) Chap. Top. Curr. Chem., pp. 49–58.

[11] S. Cobo, D. Ostrovskii, S. Bonhommeau, L. Vendier, G. Molnár, L. Salmon, K. Tanaka, and A. Bousseksou, *Single-Laser-Shot-Induced Complete Bidirectional Spin Transition at Room Temperature in Single Crystals of* $(Fe^{II}(pyrazine)(Pt(CN)_4))$, J. Am. Chem. Soc. **130**, 9019 (2008).

[12] H. Paulsen, L. Duelund, H. Winkler, H. Toftlund, and A. X. Trautwein, *Free Energy of Spin-Crossover Complexes Calculated with Density Functional Methods,* Inorg. Chem. **40**, 2201 (2001).

[13] H. Paulsen, R. Benda, C. Herta, V. Schünemann, A. I. Chumakov, L. Duelund, H. Winkler, H. Toftlund, and A. X. Trautwein, *Anisotropic Nuclear Inelastic Scattering of an Iron(II) Molecular Crystal,* Phys. Rev. Lett. **86**, 1351 (2001).

[14] P. Gütlich, H. A. Goodwin, H. Paulsen, and A. Trautwein, *Density Functional Theory Calculations for Spin Crossover Complexes,* in *Spin Crossover in Transition Metal Compounds III*, Vol. 235 (Springer Berlin / Heidelberg, 2004) Chap. Topics in Current Chemistry, pp. 197–219.

[15] M. Reiher, O. Salomon, and B. Artur Hess, *Reparameterization of hybrid functionals based on energy differences of states of different multiplicity,* Theor. Chem. Acc. **107**, 48 (2001).

[16] O. Salomon, M. Reiher, and B. A. Hess, *Assertion and validation of the performance of the B3LYP* functional for the first transition metal row and the G2 test set,* J. Chem. Phys. **117**, 4729 (2002).

[17] J. N. Harvey, *DFT computation of relative spin-state energetics of transition metal compounds,* in *Principles and applications of density functional theory in inorganic chemistry I*, Vol. 112, edited by N. Kaltsoyannis and J. E. McGrady (Springer-Verlag, 2004) Chap. Structure and Bonding.

[18] A. Fouqueau, S. Mer, M. E. Casida, L. M. Lawson Daku, A. Hauser, T. Mineva, and F. Neese, *Comparison of density functionals for energy and structural differences between the high-* $[^5T_{2g}:(t_{2g})^4(e_g)^2]$ *and low-* $[^1A_{1g} : (t_{2g})^6(e_g)^0]$ *spin states of the hexaquoferrous cation* $[Fe(H_2O)_6]^{2+}$, J. Chem. Phys. **120**, 9473 (2004).

[19] A. Fouqueau, M. E. Casida, L. M. Lawson Daku, A. Hauser, and F. Neese, *Comparison of density functionals for energy and structural differences between the high-* $[^5T_{2g} : (t_{2g})^4(e_g)^2]$ *and low-* $[^1A_{1g} : (t_{2g})^6(e_g)^0]$ *spin states of iron(II) coordination compounds. II. More functionals and the hexaminoferrous cation,* $[Fe(NH_3)_6]^{2+}$, J. Chem. Phys. **122**, 044110 (2005).

[20] L. M. Lawson Daku, A. Vargas, A. Hauser, A. Fouqueau, and M. E. Casida, *Assessment of Density Functionals for the High-Spin/Low-Spin Energy Difference in the Low-Spin Iron(II) Tris(2,2'-bipyridine) Complex,* ChemPhysChem **6**, 1393 (2005).

[21] G. Brewer, M. J. Olida, A. M. Schmiedekamp, C. Viragh, and P. Y. Zavalij, *A DFT computational study of spin crossover in iron(III) and iron(II) tripodal imidazole complexes. A comparison of experiment with calculations,* Dalton Trans. , 5617 (2006).

[22] A. M. Schmiedekamp, A. Ginnetti, B. Piccione, K. Cannon, and M. D. Ryan, *Six-coordinate Co^{2+} with imidazole, NH_3, and H_2O ligands: Approaching spin crossover,* Int. J. Quantum Chem. **107**, 1415 (2007).

[23] S. Zein, S. A. Borshch, P. Fleurat-Lessard, M. E. Casida, and H. Chermette, *Assessment of the exchange-correlation functionals for the physical description of spin transition phenomena by density functional theory methods: All the same?* J. Chem. Phys. **126**, 014105 (2007).

[24] S. Lebègue, S. Pillet, and J. G. Ángyán, *Modeling spin-crossover compounds by periodic DFT+U approach,* Phys. Rev. B **78**, 024433 (2008).

[25] F. Remacle, F. Grandjean, and G. J. Long, *A Density Functional Theory Calculation of the Electronic Properties of Several High-Spin and Low-Spin Iron(II) Pyrazolylborate Complexes,* Inorg. Chem. **47**, 4005 (2008).

[26] H. Bolvin, *$d \rightarrow d$ Spectrum and High-Spin/Low-Spin Competition in d^6 Octahedral Coordination Compounds: ab Initio Study of Potential Energy Curves,* J. Phys. Chem. A **102**, 7525 (1998).

[27] K. Pierloot and S. Vancoillie, *Relative energy of the high-($^5T_{2g}$) and low-($^1A_{1g}$) spin states of $[Fe(H_2O)_6]^{2+}$, $[Fe(NH_3)_6]^{2+}$, and $[Fe(bpy)_3]^{2+}$: CASPT2 versus density functional theory,* J. Chem. Phys. **125**, 124303 (2006).

[28] A. Sadoc, C. de Graaf, and R. Broer, *Quantum chemical study of the nature of the ground state and the pressure-induced spin transition in $CaFeO_3$,* Phys. Rev. B **75**, 165116 (2007).

[29] K. Pierloot and S. Vancoillie, *Relative energy of the high-($^5T_{2g}$) and low-($^1A_{1g}$) spin states of the ferrous complexes [Fe(L)(NHS$_4$)]: CASPT2 versus density functional theory,* J. Chem. Phys. **128**, 034104 (2008).

[30] M. Kepenekian, V. Robert, B. Le Guennic, and C. De Graaf, *Energetics of $[Fe(NCH)_6]^{2+}$ via CASPT2 calculations: A spin-crossover perspective,* J. Comput. Chem. **30**, 2327 (2009).

[31] N. Suaud, M.-L. Bonnet, C. Boilleau, P. Labèguerie, and N. Guihéry, *Light-Induced Excited Spin State Trapping: Ab Initio Study of the Physics at the Molecular Level,* J. Am. Chem. Soc. **131**, 715 (2009).

[32] B. O. Roos, P. R. Taylor, and P. E. M. Siegbahn, *A complete active space SCF method (CASSCF) using a density matrix formulated super-CI approach,* Chem. Phys. **48**, 157 (1980).

[33] K. Andersson, P.-Å. Malmqvist, B. O. Roos, A. J. Sadlej, and K. Wolinski, *Second-order perturbation theory with a CASSCF reference function,* J. Phys. Chem. **94**, 5483 (1990).

[34] K. Andersson, P.-Å. Malmqvist, and B. O. Roos, *Second-order perturbation theory with a complete active space self-consistent field reference function,* J. Chem. Phys. **96**, 1218 (1992).

[35] J. S. Griffith, *The theory of transition-metal ions* (Cambridge University Press, Cambridge, 1971).

[36] Y. Tanabe and S. Sugano, *On the absorption spectra of complex ions I,* J. Phys. Soc. Jpn. **9**, 753 (1954).

[37] R. Newman and R. M. Chrenko, *Optical Properties of Nickel Oxide,* Phys. Rev. **114**, 1507 (1959).

[38] B. H. Botch, T. H. Dunning, and J. F. Harrison, *Valence correlation in the s^2d^n, sd^{n+1}, and d^{n+2} states of the first-row transition metal atoms,* J. Chem. Phys. **75**, 3466 (1981).

[39] K. Andersson and B. O. Roos, *Excitation energies in the nickel atom studied with the complete active space SCF method and second-order perturbation theory,* Chem. Phys. Lett. **191**, 507 (1992).

[40] K. Pierloot, E. Tsokos, and B. O. Roos, *3p—3d intershell correlation effects in transition metal ions,* Chem. Phys. Lett. **214**, 583 (1993).

[41] M. Geleijns, C. de Graaf, R. Broer, and W. C. Nieuwpoort, *Theoretical study of local electronic transitions in the NiO(100) surface,* Surf. Sci. **421**, 106 (1999).

[42] B. O. Roos, *Theoretical Studies of Electronically Excited States of Molecular Systems Using Multiconfigurational Perturbation Theory,* Accounts Chem. Res. **32**, 137 (1999).

[43] K. Pierloot, *The CASPT2 method in inorganic electronic spectroscopy: from ionic transition metal to covalent actinide complexes*,* Mol. Phys. **101**, 2083 (2003).

[44] F. Aquilante, P.-Å. Malmqvist, T. B. Pedersen, A. Ghosh, and B. O. Roos, *Cholesky Decomposition-Based Multiconfiguration Second-Order Perturbation Theory (CD-CASPT2): Application to the Spin-State Energetics of* Co^{III}*(diiminato)(NPh),* J. Chem. Theory Comput. **4**, 694 (2008).

[45] B. O. Roos, R. Lindh, P.-Å. Malmqvist, V. Veryazov, and P.-O. Widmark, *Main Group Atoms and Dimers Studied with a New Relativistic ANO Basis Set,* J. Phys. Chem. A **108**, 2851 (2004).

[46] B. O. Roos, R. Lindh, P.-Å. Malmqvist, V. Veryazov, and P.-O. Widmark, *New Relativistic ANO Basis Sets for Transition Metal Atoms,* J. Phys. Chem. A **109**, 6575 (2005).

[47] J. D. Watts, J. Gauss, and R. J. Bartlett, *Coupled-cluster methods with noniterative triple excitations for restricted open-shell Hartree-Fock and other general single determinant reference functions. Energies and analytical gradients,* J. Chem. Phys. **98**, 8718 (1993).

[48] G. Karlström, R. Lindh, P.-Å. Malmqvist, B. O. Roos, U. Ryde, V. Veryazov, P.-O. Widmark, M. Cossi, B. Schimmelpfennig, P. Neogrady, and L. Seijo, *MOLCAS: a program package for computational chemistry,* Comp. Mater. Sci. **28**, 222 (2003).

[49] F. Aquilante, L. De Vico, N. Ferré, G. Ghigo, P.-Å. Malmqvist, P. Neogrády, T. B. Pedersen, M. Pitoňák, M. Reiher, B. O. Roos, L. Serrano-Andrés, M. Urban, V. Veryazov, and R. Lindh, *MOLCAS 7: The Next Generation,* J. Comput. Chem. **31**, 224 (2010).

[50] A. Sadoc, R. Broer, and C. de Graaf, *Role of charge transfer configurations in* $LaMnO_3$*,* $CaMnO_3$*, and* $CaFeO_3$*,* Journal of Chemical Physics **126**, 134709 (2007).

[51] C. T. Middleton, K. de La Harpe, C. Su, Y. K. Law, C. E. Crespo-Hernández, and B. Kohler, *DNA Excited-State Dynamics: From Single Bases to the Double Helix,* Annu. Rev. Phys. Chem. **60**, 217 (2009).

[52] C. E. Crespo-Hernández, B. Cohen, P. M. Hare, and B. Kohler, *Ultrafast Excited-State Dynamics in Nucleic Acids,* Chem. Rev. **104**, 1977 (2004).

[53] M. Merchán and L. Serrano-Andrés, *Ultrafast Internal Conversion of Excited Cytosine via the Lowest ππ* Electronic Singlet State,* J. Am. Chem. Soc. **125**, 8108 (2003).

[54] L. Serrano-Andrés and M. Merchán, *Quantum chemistry of the excited state: 2005 overview,* J. Mol. Struct. (THEOCHEM) **729**, 99 (2005).

[55] M. Merchán, R. González-Luque, T. Climent, L. Serrano-Andrés, E. Rodríguez, M. Reguero, and D. Peláez, *Unified Model for the Ultrafast Decay of Pyrimidine Nucleobases,* J. Phys. Chem. B **110**, 26471 (2006).

[56] J. González-Vázquez and L. González, *A time-dependent picture of the ultrafast deactivation of keto-cytosine including three-state conical intersections.* ChemPhysChem **11**, 3617 (2010).

[57] M. Barbatti, A. J. A. Aquino, J. J. Szymczak, D. Nachtigallova, and H. Lischka, *Photodynamical simulations of cytosine: characterization of the ultrafast bi-exponential UV deactivation,* Phys. Chem. Chem. Phys. **13**, 6145 (2011).

[58] M. Merchán, L. Serrano-Andrés, M. A. Robb, and L. Blancafort, *Triplet-State Formation along the Ultrafast Decay of Excited Singlet Cytosine,* J. Am. Chem. Soc. **127**, 1820 (2005).

[59] L. Blancafort, *Energetics of Cytosine Singlet Excited-State Decay Paths—A Difficult Case for CASSCF and CASPT2,* Photochem. Photobiol. **83**, 603 (2007).

[60] K. Kosma, C. Schröter, E. Samoylova, I. V. Hertel, and T. Schultz, *Excited-State Dynamics of Cytosine Tautomers,* J. Am. Chem. Soc. **131**, 16939 (2009).

[61] P. R. Callis and W. Simpson, *Polarization of electronic transitions in cytosine,* J. Am. Chem. Soc. **92**, 3593 (1970).

[62] F. Zaloudek, J. S. Novros, and L. B. Clark, *The electronic spectrum of cytosine,* J. Am. Chem. Soc. **107**, 7344 (1985).

[63] J. M. O. Matos and B. O. Roos, *Ab initio quantum chemical study of the π-electron spectrum of the cytosine molecule,* J. Am. Chem. Soc. **110**, 7664 (1988).

[64] J. D. Petke, G. M. Maggiora, and R. E. Christoffersen, *Ab initio configuration interaction and random phase approximation calculations of the excited singlet and triplet states of uracil and cytosine,* J. Phys. Chem. **96**, 6992 (1992).

[65] L. B. Clark and I. Tinoco, *Correlations in the Ultraviolet Spectra of the Purine and Pyrimidine Bases,* J. Am. Chem. Soc. **87**, 11 (1965).

[66] L. B. Clark, G. G. Peschel, and I. Tinoco, *Vapor Spectra and Heats of Vaporization of Some Purine and Pyrimidine Bases,* J. Phys. Chem. **69**, 3615 (1965).

[67] W. Voelter, R. Records, E. Bunnenberg, and C. Djerassi, *Magnetic circular dichroism studies. VI. Investigation of some purines, pyrimidines, and nucleosides,* J. Am. Chem. Soc. **90**, 6163 (1968).

[68] T. P. Lewis and W. A. Eaton, *Polarized single-crystal absorption spectrum of cytosine monohydrate,* J. Am. Chem. Soc. **93**, 2054 (1971).

[69] A. O. Alyoubi and R. H. Hilal, *A theoretical and experimental investigation of the electronic spectra and tautomerization of nucleobases,* Biophys. Chem. **55**, 231 (1995).

[70] W. Hug and I. Tinoco, *Electronic spectra of nucleic acid bases. I. Interpretation of the in-plane spectra with the aid of all valence electron MO-CIA [configuration interaction] calculations,* J. Am. Chem. Soc. **95**, 2803 (1973).

[71] W. Hug and I. Tinoco, *Electronic spectra of nucleic acid bases. II. Out-of-plane transitions and the structure of the nonbonding orbitals,* J. Am. Chem. Soc. **96**, 665 (1974).

[72] M. P. Fülscher and B. O. Roos, *Theoretical Study of the Electronic Spectrum of Cytosine,* J. Am. Chem. Soc. **117**, 2089 (1995).

[73] B. E. Billinghurst, S. A. Oladepo, and G. R. Loppnow, *pH-Dependent UV Resonance Raman Spectra of Cytosine and Uracil,* J. Phys. Chem. B **113**, 7392 (2009).

[74] K. Tomić, J. Tatchen, and C. M. Marian, *Quantum Chemical Investigation of the Electronic Spectra of the Keto, Enol, and Keto−Imine Tautomers of Cytosine,* J. Phys. Chem. A **109**, 8410 (2005).

[75] M. Dreyfus, O. Bensaude, G. Dodin, and J. E. Dubois, *Tautomerism in cytosine and 3-methylcytosine. A thermodynamic and kinetic study,* J. Am. Chem. Soc. **98**, 6338 (1976).

[76] M. Szczesniak, K. Szczepaniak, J. S. Kwiatkowski, K. KuBulat, and W. B. Person, *Matrix isolation infrared studies of nucleic acid constituents. 5. Experimental matrix-isolation and theoretical ab initio SCF molecular orbital studies of the infrared spectra of cytosine monomers,* J. Am. Chem. Soc. **110**, 8319 (1988).

[77] R. D. Brown, P. D. Godfrey, D. McNaughton, and A. P. Pierlot, *Tautomers of cytosine by microwave spectroscopy,* J. Am. Chem. Soc. **111**, 2308 (1989).

[78] V. Feyer, O. Plekan, R. Richter, M. Coreno, M. de Simone, K. C. Prince, A. B. Trofimov, I. L. Zaytseva, and J. Schirmer, *Tautomerism in Cytosine and Uracil: A Theoretical and Experimental X-ray Absorption and Resonant Auger Study,* J. Phys. Chem. A **114**, 10270 (2010).

[79] G. Bazso, G. Tarczay, G. Fogarasi, and P. G. Szalay, *Tautomers of cytosine and their excited electronic states: a matrix isolation spectroscopic and quantum chemical study,* Phys. Chem. Chem. Phys. **13**, 6799 (2011).

[80] A. Pedone, M. Biczysko, and V. Barone, *Environmental Effects in Computational Spectroscopy: Accuracy and Interpretation,* ChemPhysChem **11**, 1812 (2010).

[81] J. Tomasi and M. Persico, *Molecular Interactions in Solution: An Overview of Methods Based on Continuous Distributions of the Solvent,* Chem. Rev. **94**, 2027 (1994).

[82] C. Colominas, F. J. Luque, and M. Orozco, *Tautomerism and Protonation of Guanine and Cytosine. Implications in the Formation of Hydrogen-Bonded Complexes,* J. Am. Chem. Soc. **118**, 6811 (1996).

[83] J. R. Sambrano, A. R. de Souza, J. J. Queralt, and J. Andrés, *A theoretical study on cytosine tautomers in aqueous media by using continuum models,* Chem. Phys. Lett. **317**, 437 (2000).

[84] Y. Mercier, F. Santoro, M. Reguero, and R. Improta, *The Decay from the Dark $n\pi^*$ Excited State in Uracil: An Integrated CASPT2/CASSCF and PCM/TD-DFT Study in the Gas Phase and in Water,* J. Phys. Chem. B **112**, 10769 (2008).

[85] R. Improta and V. Barone, *PCM/TD-DFT study of the two lowest excited states of uracil derivatives in solution: The effect of the functional and of the cavity model,* J. Mol. Struct. (THEOCHEM) **914**, 87 (2009).

[86] M. K. Shukla and J. Leszczynski, *Interaction of Water Molecules with Cytosine Tautomers: An Excited-State Quantum Chemical Investigation,* J. Phys. Chem. A **106**, 11338 (2002).

[87] A. Broo and A. Holmén, *Calculations and Characterization of the Electronic Spectra of DNA Bases Based on ab Initio MP2 Geometries of Different Tautomeric Forms,* J. Phys. Chem. A **101**, 3589 (1997).

[88] K. Kowalski and M. Valiev, *Application of High-Level Iterative Coupled-Cluster Methods to the Cytosine Molecule,* J. Phys. Chem. A **112**, 5538 (2008).

[89] G. Brancato, N. Rega, and V. Barone, *Microsolvation of uracil anion radical in aqueous solution: a QM/MM study,* Chem. Phys. Lett. **500**, 104 (2010).

[90] J. D. Watson and F. H. C. Crick, *Molecular Structure of Nucleic Acids: A Structure for Deoxyribose Nucleic Acid,* Nature **171**, 737 (1953).

[91] G. Olaso-González, D. Roca-Sanjuán, L. Serrano-Andrés, and M. Merchán, *Toward the understanding of DNA fluorescence: The singlet excimer of cytosine,* J. Chem. Phys. **125**, 231102 (2006).

[92] O. Kostko, K. Bravaya, A. Krylov, and M. Ahmed, *Ionization of cytosine monomer and dimer studied by VUV photoionization and electronic structure calculations,* Phys. Chem. Chem. Phys. **12**, 2860 (2010).

[93] M. Barbatti, *The role of tautomers in the UV absorption of urocanic acid,* Phys. Chem. Chem. Phys. **13**, 4686 (2011).

[94] O. Isayev, A. Furmanchuk, O. V. Shishkin, L. Gorb, and J. Leszczynski, *Are Isolated Nucleic Acid Bases Really Planar?: A Car−Parrinello Molecular Dynamics Study,* J. Phys. Chem. B **111**, 3476 (2007).

[95] P. Schyman, A. Laaksonen, and H. W. Hugosson, *Phosphodiester bond rupture in 5' and 3' cytosine monophosphate in aqueous environment and the effect of low-energy electron attachment: A Car-Parrinello QM/MM molecular dynamics study,* Chem. Phys. Lett. **462**, 289 (2008).

[96] L. M. Lawson Daku, J. Linares, and M.-L. Boillot, *Ab initio static and molecular dynamics study of the absorption spectra of the 4-styrylpyridine photoswitch in its cis and trans forms,* Phys. Chem. Chem. Phys. **12**, 6107 (2010).

[97] V. Manzoni, M. L. Lyra, R. M. Gester, K. Coutinho, and S. Canuto, *Study of the optical and magnetic properties of pyrimidine in water combining PCM and QM/MM methodologies,* Phys. Chem. Chem. Phys. **12**, 14023 (2010).

[98] V. Barone, J. Bloino, S. Monti, A. Pedone, and G. Prampolini, *Theoretical multilevel approach for studying the photophysical properties of organic dyes in solution,* Phys. Chem. Chem. Phys. **12**, 10550 (2010).

[99] V. Barone, J. Bloino, S. Monti, A. Pedone, and G. Prampolini, *Fluorescence spectra of organic dyes in solution: a time dependent multilevel approach,* Phys. Chem. Chem. Phys. **13**, 2160 (2011).

[100] M. Valiev and K. Kowalski, *Hybrid coupled cluster and molecular dynamics approach: Application to the excitation spectrum of cytosine in the native DNA environment,* J. Chem. Phys. **125**, 211101 (2006).

[101] M. Barbatti, A. J. A. Aquino, and H. Lischka, *The UV absorption of nucleobases: semi-classical ab initio spectra simulations,* Phys. Chem. Chem. Phys. **12**, 4959 (2010).

[102] R. Car and M. Parrinello, *Unified Approach for Molecular Dynamics and Density-Functional Theory,* Phys. Rev. Lett. **55**, 2471 (1985).

[103] M. Cossi, N. Rega, G. Scalmani, and V. Barone, *Polarizable dielectric model of solvation with inclusion of charge penetration effects,* J. Chem. Phys. **114**, 5691 (2001).

[104] N. Troullier and J. L. Martins, *Efficient pseudopotentials for plane-wave calculations,* Phys. Rev. B **43**, 1993 (1991).

[105] A. D. Becke, *Density-functional exchange-energy approximation with correct asymptotic behavior,* Phys. Rev. A **38**, 3098 (1988).

[106] C. Lee, W. Yang, and R. G. Parr, *Development of the Colle-Salvetti correlation-energy formula into a functional of the electron density,* Phys. Rev. B **37**, 785 (1988).

[107] W. G. Hoover, *Canonical dynamics: Equilibrium phase-space distributions,* Phys. Rev. A **31**, 1695 (1985).

[108] S. Nosé, *A unified formulation of the constant temperature molecular dynamics methods,* J. Chem. Phys. **81**, 511 (1984).

[109] J. C. Grossman, E. Schwegler, E. W. Draeger, F. Gygi, and G. Galli, *Towards an assessment of the accuracy of density functional theory for first principles simulations of water,* J. Chem. Phys. **120**, 300 (2004).

[110] D. Cremer and J. A. Pople, *General definition of ring puckering coordinates,* J. Am. Chem. Soc. **97**, 1354 (1975).

[111] J. C. A. Boeyens, *The conformation of six-membered rings,* J. Chem. Crystallogr. **8**, 317 (1978).

[112] A. L. Spek, *Structure validation in chemical crystallography,* Acta Crystallogr. D **65**, 148 (2009).

[113] N. Forsberg and P.-Å. Malmqvist, *Multiconfiguration perturbation theory with imaginary level shift,* Chem. Phys. Lett. **274**, 196 (1997).

[114] P.-Å. Malmqvist and B. O. Roos, *The CASSCF state interaction method,* Chem. Phys. Lett. **155**, 189 (1989).

[115] R. D. C. Team, *R: A Language and Environment for Statistical Computing*, Vienna, Austria (2009).

[116] H. Kessler, *Detection of Hindered Rotation and Inversion by NMR Spectroscopy,* Angew. Chem.-Int. Edit. **9**, 219 (1970).

[117] L. Gagliardi, R. Lindh, and G. Karlström, *Local properties of quantum chemical systems: The LoProp approach,* J. Chem. Phys. **121**, 4494 (2004).

[118] W. L. Roth, *Magnetic Structures of MnO, FeO, CoO, and NiO,* Phys. Rev. **110**, 1333 (1958).

[119] S. Massidda, M. Posternak, A. Baldereschi, and R. Resta, *Noncubic Behavior of Antiferromagnetic Transition-Metal Monoxides with the Rocksalt Structure,* Phys. Rev. Lett. **82**, 430 (1999).

[120] F. J. Morin, *Electrical Properties of NiO,* Phys. Rev. **93**, 1199 (1954).

[121] D. R. Stephens and H. G. Drickamer, *Effect of Pressure on the Spectra of Five Nickel Complexes,* J. Chem. Phys. **34**, 937 (1961).

[122] T. Eto, S. Endo, M. Imai, Y. Katayama, and T. Kikegawa, *Crystal structure of NiO under high pressure,* Phys. Rev. B **61**, 14984 (2000).

[123] A. Shukla, J.-P. Rueff, J. Badro, G. Vanko, A. Mattila, F. M. F. de Groot, and F. Sette, *Charge transfer at very high pressure in NiO,* Phys. Rev. B **67**, 081101 (2003).

[124] R. J. Powell and W. E. Spicer, *Optical Properties of NiO and CoO,* Phys. Rev. B **2**, 2182 (1970).

[125] W. Low, *Paramagnetic and Optical Spectra of Divalent Nickel in Cubic Crystalline Fields,* Phys. Rev. **109**, 247 (1958).

[126] D. Adler and J. Feinleib, *Electrical and Optical Properties of Narrow-Band Materials,* Phys. Rev. B **2**, 3112 (1970).

[127] R. Merlin, T. P. Martin, A. Polian, M. Cardona, B. Andlauer, and D. Tannhauser, *Two magnon resonant Raman scattering in transition metal oxides,* J. Magn. Magn. Mater. **9**, 83 (1978).

[128] R. Merlin, *Electronic Structure of NiO,* Phys. Rev. Lett. **54**, 2727 (1985).

[129] G. A. Sawatzky and J. W. Allen, *Magnitude and Origin of the Band Gap in NiO,* Phys. Rev. Lett. **53**, 2339 (1984).

[130] S. Hüfner and G. K. Wertheim, *X-Ray Photoelectron Band Structure of Some Transition-Metal Compounds,* Phys. Rev. B **8**, 4857 (1973).

[131] M. R. Thuler, R. L. Benbow, and Z. Hurych, *Photoemission intensities at the 3p threshold resonance of NiO and Ni,* Phys. Rev. B **27**, 2082 (1983).

[132] S. J. Oh, J. W. Allen, I. Lindau, and J. C. Mikkelsen, *Resonant valence-band satellites and polar fluctuations in nickel and its compounds,* Phys. Rev. B **26**, 4845 (1982).

[133] Z. X. Shen, C. K. Shih, O. Jepsen, W. E. Spicer, I. Lindau, and J. W. Allen, *Aspects of the correlation effects, antiferromagnetic order, and translational symmetry of the electronic structure of NiO and CoO,* Phys. Rev. Lett. **64**, 2442 (1990).

[134] Z. X. Shen, R. S. List, D. S. Dessau, B. O. Wells, O. Jepsen, A. J. Arko, R. Barttlet, C. K. Shih, F. Parmigiani, J. C. Huang, and P. A. P. Lindberg, *Electronic structure of NiO: Correlation and band effects,* Phys. Rev. B **44**, 3604 (1991).

[135] S. Hüfner, P. Steiner, I. Sander, F. Reinert, and H. Schmitt, *The optical gap of NiO,* Z. Phys. B. Con. Mat. **86**, 207 (1992).

[136] J. C. Woicik, E. J. Nelson, D. Heskett, J. Warner, L. E. Berman, B. A. Karlin, I. A. Vartanyants, M. Z. Hasan, T. Kendelewicz, Z. X. Shen, and P. Pianetta, *X-ray standing-wave investigations of valence electronic structure,* Phys. Rev. B **64**, 125115 (2001).

[137] T. M. Schuler, D. L. Ederer, S. Itza-Ortiz, G. T. Woods, T. A. Callcott, and J. C. Woicik, *Character of the insulating state in NiO: A mixture of charge-transfer and Mott-Hubbard character,* Phys. Rev. B **71**, 115113 (2005).

[138] P. S. Bagus, H. J. Freund, T. Minerva, G. Pacchioni, and F. Parmigiani, *Charge transfer effects and photoemission in transition metal oxides,* Chem. Phys. Lett. **251**, 90 (1996).

[139] P. S. Bagus, R. Broer, C. de Graaf, and W. C. Nieuwpoort, *The electronic structure of NiO for Ni 3s-hole states including full orbital relaxation and localization,* J. Electron. Spectrosc. **98-99**, 303 (1999).

[140] C. Gougoussis, M. Calandra, A. Seitsonen, C. Brouder, A. Shukla, and F. Mauri, *Intrinsic charge transfer gap in NiO from Ni K–edge x-ray absorption spectroscopy,* Phys. Rev. B **79**, 045118 (2009).

[141] N. F. Mott, *The Basis of the Electron Theory of Metals, with Special Reference to the Transition Metals,* P. Phys. Soc. Lond. A **62**, 416 (1949).

[142] J. Hubbard, *Electron Correlations in Narrow Energy Bands. II. The Degenerate Band Case,* Proc. R. Soc. Lond. A **277**, 237 (1964).

[143] J. Hubbard, *Electron Correlations in Narrow Energy Bands. III. An Improved Solution,* Proc. R. Soc. Lond. A **281**, 401 (1964).

[144] N. F. Mott, *Metal-Insulator Transition,* Rev. Mod. Phys. **40**, 677 (1968).

[145] L. F. Mattheiss, *Electronic Structure of the* 3*d Transition-Metal Monoxides. I. Energy-Band Results,* Phys. Rev. B **5**, 290 (1972).

[146] L. F. Mattheiss, *Electronic Structure of the* 3*d Transition-Metal Monoxides. II. Interpretation,* Phys. Rev. B **5**, 306 (1972).

[147] J. Zaanen, G. A. Sawatzky, and J. W. Allen, *Band gaps and electronic structure of transition-metal compounds,* Phys. Rev. Lett. **55**, 418 (1985).

[148] K. Terakura, T. Oguchi, A. R. Williams, and J. Kübler, *Band theory of insulating transition-metal monoxides: Band-structure calculations,* Phys. Rev. B **30**, 4734 (1984).

[149] A. Svane and O. Gunnarsson, *Transition-metal oxides in the self-interaction-corrected density-functional formalism,* Phys. Rev. Lett. **65**, 1148 (1990).

[150] S. Y. Savrasov and G. Kotliar, *Linear Response Calculations of Lattice Dynamics in Strongly Correlated Systems,* Phys. Rev. Lett. **90**, 056401 (2003).

[151] J. Kuneš, V. I. Anisimov, S. L. Skornyakov, A. V. Lukoyanov, and D. Vollhardt, *NiO: Correlated Band Structure of a Charge-Transfer Insulator,* Phys. Rev. Lett. **99**, 156404 (2007).

[152] I. de P. R. Moreira, F. Illas, and R. L. Martin, *Effect of Fock exchange on the electronic structure and magnetic coupling in NiO,* Phys. Rev. B **65**, 155102 (2002).

[153] S. L. Dudarev, G. A. Botton, S. Y. Savrasov, C. J. Humphreys, and A. P. Sutton, *Electron-energy-loss spectra and the structural stability of nickel oxide: An LSDA+U study,* Phys. Rev. B **57**, 1505 (1998).

[154] O. Bengone, M. Alouani, P. Blöchl, and J. Hugel, *Implementation of the projector augmented-wave LDA+U method: Application to the electronic structure of NiO,* Phys. Rev. B **62**, 16392 (2000).

[155] V. I. Anisimov, P. Kuiper, and J. Nordgren, *First-principles calculation of NiO valence spectra in the impurity-Anderson-model approximation,* Phys. Rev. B **50**, 8257 (1994).

[156] F. Aryasetiawan and O. Gunnarsson, *Electronic Structure of NiO in the GW Approximation,* Phys. Rev. Lett. **74**, 3221 (1995).

[157] H. Jiang, R. I. Gomez-Abal, P. Rinke, and M. Scheffler, *First-principles modeling of localized d states with the GW@LDA + U approach,* Phys. Rev. B **82**, 045108 (2010).

[158] M. S. Hybertsen, M. Schlüter, and N. E. Christensen, *Calculation of Coulomb-interaction parameters for La_2CuO_4 using a constrained-density-functional approach,* Phys. Rev. B **39**, 9028 (1989).

[159] Z. Barandiarán and L. Seijo, *The ab initio model potential representation of the crystalline environment. Theoretical study of the local distortion on NaCl:Cu^+,* J. Chem. Phys. **89**, 5739 (1988).

[160] M. W. Haverkort, A. Tanaka, L. H. Tjeng, and G. A. Sawatzky, *Nonresonant Inelastic X-Ray Scattering Involving Excitonic Excitations: The Examples of NiO and CoO,* Phys. Rev. Lett. **99**, 257401 (2007).

[161] S. Huotari, T. Pylkkänen, G. Vankó, R. Verbeni, P. Glatzel, and G. Monaco, *Crystal-field excitations in NiO studied with hard x-ray resonant inelastic x-ray scattering at the Ni K edge,* Phys. Rev. B **78**, 041102 (2008).

[162] A. Fujimori and F. Minami, *Valence-band photoemission and optical absorption in nickel compounds,* Phys. Rev. B **30**, 957 (1984).

[163] G. J. M. Janssen and W. C. Nieuwpoort, *Band gap in NiO: A cluster study,* Phys. Rev. B **38**, 3449 (1988).

[164] K. Pierloot, E. Van Praet, L. G. Vanquickenborne, and B. O. Roos, *Systematic ab initio study of the ligand field spectra of hexacyanometalate complexes,* J. Phys. Chem. **97**, 12220 (1993).

[165] C. de Graaf, R. Broer, and W. C. Nieuwpoort, *Electron correlation effects on the d-d excitations in NiO,* Chem. Phys. **208**, 35 (1996).

[166] B. T. Thole and P. T. van Duijnen, *On the quantum mechanical treatment of solvent effects,* Theor. Chem. Acc. **55**, 307 (1980).

[167] A. H. de Vries, P. T. van Duijnen, A. H. Juffer, J. A. C. Rullmann, J. P. Dijkman, H. Merenga, and B. T. Thole, *Implementation of reaction field methods in quantum chemistry computer codes,* J. Comput. Chem. **16**, 37 (1995).

[168] P. T. van Duijnen, M. Swart, and L. Jensen, *The Discrete Reaction Field approach for calculating solvent effects,* in *Solvation Effects on Molecules and Biomolecules*, Vol. 6, edited by S. Canuto (Springer Netherlands, 2008) Chap. Challenges and Advances in Computational Chemistry and Physics, pp. 39–102.

[169] R. W. G. Wyckoff, *Crystal Structures*, 2nd ed., edited by R. W. G. Wyckoff (John Wiley & Sons, New York, 1969).

[170] H. M. Evjen, *On the Stability of Certain Heteropolar Crystals,* Phys. Rev. **39**, 675 (1932).

[171] K. Satitkovitchai, Y. Pavlyukh, and W. Hübner, *Ab initio study of spin-orbit coupling effects on the low-lying excited states of NiO,* Phys. Rev. B **72**, 045116 (2005).

[172] V. Staemmler and K. Fink, *An ab initio cluster study of the magnetic properties of the CoO(0 0 1) surface,* Chem. Phys. **278**, 79 (2002).

[173] C. J. Calzado and J.-P. Malrieu, *Proposal of an extended $t - J$ Hamiltonian for high-T_c cuprates from ab initio calculations on embedded clusters,* Phys. Rev. B **63**, 214520 (2001).

[174] C. de Graaf, C. Sousa, and R. Broer, *Ionization and excitation energies in CuCl and NiO within different embedding schemes,* J. Mol. Struct. (THEOCHEM) **458**, 53 (1998).

[175] J. L. Pascual, L. Seijo, and Z. Barandiarán, *Ab initio model-potential embedded-cluster study of Jahn-Teller parameters and electronic transition energies of Cr^{2+} in oxide and fluoride octahedral coordination,* Phys. Rev. B **53**, 1138 (1996).

[176] R. D. Shannon and R. X. Fischer, *Empirical electronic polarizabilities in oxides, hydroxides, oxyfluorides, and oxychlorides,* Phys. Rev. B **73**, 235111 (2006).

[177] M. Swart and P. T. van Duijnen, *DRF90: a polarizable force field,* Mol. Simulat. **32**, 471 (2006).

[178] G. J. M. Janssen, *Localized 3d-Like States In Transition Metal Compounds*, Ph.D. thesis, Rijksuniversiteit te Groningen, Groningen, The Netherlands (1986).

[179] R. von Helmolt, J. Wecker, B. Holzapfel, L. Schultz, and K. Samwer, *Giant negative magnetoresistance in perovskitelike $La_{2/3}Ba_{1/3}MnO_x$ ferromagnetic films,* Phys. Rev. Lett. **71**, 2331 (1993).

[180] M. B. Salamon and M. Jaime, *The physics of manganites: Structure and transport,* Rev. Mod. Phys. **73**, 583 (2001).

[181] J. Rodríguez-Carvajal, M. Hennion, F. Moussa, A. H. Moudden, L. Pinsard, and A. Revcolevschi, *Neutron-diffraction study of the Jahn-Teller transition in stoichiometric $LaMnO_3$,* Phys. Rev. B **57**, (1998).

[182] Y. Murakami, J. P. Hill, D. Gibbs, M. Blume, I. Koyama, M. Tanaka, H. Kawata, T. Arima, Y. Tokura, K. Hirota, and Y. Endoh, *Resonant X-ray scattering from orbital ordering in $LaMnO_3$,* Phys. Rev. Lett. **81**, 582 (1998).

[183] E. O. Wollan and W. C. Koehler, *Neutron Diffraction Study of the Magnetic Properties of the Series of Perovskite-Type Compounds [(1 − x)La, xCa]MnO_3,* Phys. Rev. **100**, 545 (1955).

[184] C. de Graaf, C. Sousa, and R. Broer, *Ab initio study of the charge order and Zener polaron formation in half-doped manganites,* Phys. Rev. B **70**, 235104 (2004).

[185] E. Pavarini, E. Koch, and A. I. Lichtenstein, *Mechanism for Orbital Ordering in $KCuF_3$,* Phys. Rev. Lett. **101**, 266405 (2008).

[186] E. Pavarini and E. Koch, *Origin of Jahn-Teller Distortion and Orbital Order in $LaMnO_3$,* Phys. Rev. Lett. **104**, 086402 (2010).

[187] T. Arima, Y. Tokura, and J. B. Torrance, *Variation of optical gaps in perovskite-type 3d transition-metal oxides,* Phys. Rev. B **48**, 17006 (1993).

[188] J. H. Jung, K. H. Kim, D. J. Eom, T. W. Noh, E. J. Choi, J. Yu, Y. S. Kwon, and Y. Chung, *Determination of electronic band structures of $CaMnO_3$ and $LaMnO_3$ using optical-conductivity analyses,* Phys. Rev. B **55**, 15489 (1997).

[189] K. H. Ahn and A. J. Millis, *Effects of magnetic ordering on the anisotropy and temperature dependence of the optical conductivity in $LaMnO_3$: A tight-binding approach,* Phys. Rev. B **61**, 13545 (2000).

[190] K. Tobe, T. Kimura, Y. Okimoto, and Y. Tokura, *Anisotropic optical spectra in a detwinned $LaMnO_3$ crystal,* Phys. Rev. B **64**, 184421 (2001).

[191] L. Hozoi, A. H. de Vries, and R. Broer, *X-ray spectroscopy at the Mn K edge in $LaMnO_3$: An ab initio study,* Phys. Rev. B **64**, 165104 (2001).

[192] A. Stoyanova, *Delocalized and Correlated Wave Functions for Excited States in Extended Systems*, Ph.D. thesis, Rijksuniversiteit te Groningen, Groningen, The Netherlands (2006).

[193] M. W. Kim, P. Murugavel, S. Parashar, J. S. Lee, and T. W. Noh, *Origin of the 2 eV peak in optical absorption spectra of LaMnO 3 : an explanation based on the orbitally degenerate Hubbard model,* New J. Phys. **6**, 156 (2004).

[194] N. N. Kovaleva, A. V. Boris, C. Bernhard, A. Kulakov, A. Pimenov, A. M. Balbashov, G. Khaliullin, and B. Keimer, *Spin-Controlled Mott-Hubbard Bands in $LaMnO_3$ Probed by Optical Ellipsometry,* Phys. Rev. Lett. **93**, 147204 (2004).

[195] A. S. Moskvin, *One-center charge transfer transitions in manganites,* Phys. Rev. B **65**, 205113 (2002).

[196] A. S. Moskvin, A. A. Makhnev, L. V. Nomerovannaya, N. N. Loshkareva, and A. M. Balbashov, *Interplay of $p-d$ and $d-d$ charge transfer transitions in rare-earth perovskite manganites,* Phys. Rev. B **82**, 035106 (2010).

[197] P.-Å. Malmqvist, A. Rendell, and B. O. Roos, *The restricted active space self-consistent-field method, implemented with a split graph unitary group approach,* J. Phys. Chem. **94**, 5477 (1990).

[198] C. de Graaf, W. A. de Jong, R. Broer, and W. C. Nieuwpoort, *Theoretical study of the crystal field excitations in CoO,* Chem. Phys. **237**, 59 (1998).

[199] C. de Graaf and R. Broer, *Midinfrared spectrum of undoped cuprates: d-d transitions studied by ab initio methods,* Phys. Rev. B **62**, 702 (2000).

[200] S. E. Derenzo, M. K. Klintenberg, and M. J. Weber, *Determining point charge arrays that produce accurate ionic crystal fields for atomic cluster calculations,* J. Chem. Phys. **112**, 2074 (2000).

[201] A. Stoyanova, C. Sousa, C. de Graaf, and R. Broer, *Hopping matrix elements from first-principles studies of overlapping fragments: Double exchange parameters in manganites,* Int. J. Quantum Chem. **106**, 2444 (2006).

[202] D. D. Sarma, N. Shanthi, S. R. Barman, N. Hamada, H. Sawada, and K. Terakura, *Band Theory for Ground-State Properties and Excitation Spectra of Perovskite $LaMO_3$ (M = Mn, Fe, Co, Ni),* Phys. Rev. Lett. **75**, 1126 (1995).

[203] M.-A. Carvajal, M. Reguero, and C. de Graaf, *On the mechanism of the photoinduced magnetism in copper octacyanomolybdates,* Chem. Commun. **46**, 5737 (2010).

[204] F. Aquilante, T. B. Pedersen, and R. Lindh, *Low-cost evaluation of the exchange Fock matrix from Cholesky and density fitting representations of the electron repulsion integrals,* J. Chem. Phys. **126**, 194106 (2007).

[205] C. Angeli, R. Cimiraglia, and J.-P. Malrieu, *N-electron valence state perturbation theory: a fast implementation of the strongly contracted variant,* Chem. Phys. Lett. **350**, 297 (2001).

[206] C. Angeli, S. Borini, M. Cestari, and R. Cimiraglia, *A quasidegenerate formulation of the second order n-electron valence state perturbation theory approach,* J. Chem. Phys. **121**, 4043 (2004).

[207] C. Angeli, M. Pastore, and R. Cimiraglia, *New perspectives in multireference perturbation theory: the n–electron valence state approach,* Theor. Chem. Acc. **117**, 743 (2007).

[208] J. M. Rawson, A. Alberola, and A. Whalley, *Thiazyl radicals: old materials for new molecular devices,* J. Mat. Chem. **16**, 2560 (2006).

[209] W. Fujita and K. Awaga, *Room-Temperature Magnetic Bistability in Organic Radical Crystals,* Science **286**, 261 (1999).

[210] W. Fujita, K. Awaga, H. Matsuzaki, and H. Okamoto, *Room-temperature magnetic bistability in organic radical crystals: Paramagnetic-diamagnetic phase transition in 1,3,5-trithia-2,4,6-triazapentalenyl,* Phys. Rev. B **65**, 064434 (2002).

[211] M. Verot, J.-B. Rota, M. Kepenekian, B. L. Guennic, and V. Robert, *Magnetic and conduction properties in 1D organic radical materials: an ab initio inspection for a challenging quest,* Phys. Chem. Chem. Phys. **13**, 6657 (2011).

[212] J. Miralles, O. Castell, R. Caballol, and J.-P. Malrieu, *Specific CI calculation of energy differences: Transition energies and bond energies,* Chem. Phys. **172**, 33 (1993).

[213] N. Ben Amor and D. Maynau, *Size-consistent self-consistent configuration interaction from a complete active space,* Chem. Phys. Lett. **286**, 211 (1998).

[214] V. M. García, O. Castell, R. Caballol, and J. P. Malrieu, *An iterative difference-dedicated configuration interaction. Proposal and test studies,* Chem. Phys. Lett. **238**, 222 (1995).

[215] K. Andersson and A. J. Sadlej, *Electric dipole polarizabilities of atomic valence states,* Phys. Rev. A **46**, 2356 (1992).

[216] O. Sato, T. Iyoda, A. Fujishima, and K. Hashimoto, *Photoinduced magnetization of a cobalt-iron cyanide,* Science **272**, 704 (1996).

[217] O. Sato, Y. Einaga, A. Fujishima, and K. Hashimoto, *Photoinduced Long-Range Magnetic Ordering of a Cobalt–Iron Cyanide,* Inorg. Chem. **38**, 4405 (1999).

[218] A. Bleuzen, C. Lomenech, V. Escax, F. Villain, F. Varret, C. Cartier dit Moulin, and M. Verdaguer, *Photoinduced Ferrimagnetic Systems in Prussian Blue Analogues $C^I_x Co_4[Fe(CN)_6]_y$ (C^I = Alkali Cation). 1. Conditions to Observe the Phenomenon,* J. Am. Chem. Soc. **122**, 6648 (2000).

[219] P. Gütlich, Y. Garcia, and T. Woike, *Photoswitchable coordination compounds,* Coordin. Chem. Rev. **219-221**, 839 (2001).

[220] B. Le Guennic, S. Borshch, and V. Robert, *Prussian Blue Analogue $CsFe[Cr(CN)_6]$ as a Matrix for the Fe(II) Spin-Crossover,* Inorg. Chem. **46**, 11106 (2007).

[221] J. Larionova, M. Gross, M. Pilkington, H. Andres, H. Stoeckli-Evans, H. U. Güdel, and S. Decurtins, *High-Spin Molecules: A Novel Cyano-Bridged Mn Molecular Cluster with a S=51/2 Ground State and Ferromagnetic Intercluster Ordering at Low Temperatures,* Angewandte Chemie International Edition **39**, 1605 (2000).

[222] J. M. Herrera, V. Marvaud, M. Verdaguer, J. Marrot, M. Kalisz, and C. Mathonière, *Reversible Photoinduced Magnetic Properties in the Heptanuclear Complex $[Mo^{IV}(CN)_2(CN–CuL)_6]^{8+}$: A Photomagnetic High-Spin Molecule,* Angewandte Chemie International Edition **43**, 5468 (2004).

[223] M.-A. Arrio, J. Long, C. C. dit Moulin, A. Bachschmidt, V. Marvaud, A. Rogalev, C. Mathonière, F. Wilhelm, and P. Sainctavit, *Photoinduced Magnetization on Mo Ion in Copper Octacyanomolybdate: An X-ray Magnetic Circular Dichroism Investigation,* Journal of Physical Chemistry C **114**, 593 (2010).

[224] S. Decurtins, P. Gutlich, C. Kohler, H. Spiering, and A. Hauser, *Light-Induced Excited Spin State Trapping In A Transition-Metal Complex - The Hexa-1-Propyltetrazole-Iron (II) Tetrafluoroborate Spin-Crossover System,* Chem. Phys. Lett. **105**, 1 (1984).

[225] W. Gawelda, A. Cannizzo, V.-T. Pham, F. van Mourik, C. Bressler, and M. Chergui, *Ultrafast Nonadiabatic Dynamics of $[Fe^{II}(bpy)_3]^{2+}$ in Solution,* J. Am. Chem. Soc. **129**, 8199 (2007).

[226] W. Gawelda, V.-T. Pham, M. Benfatto, Y. Zaushitsyn, M. Kaiser, D. Grolimund, S. L. Johnson, R. Abela, A. Hauser, C. Bressler, and M. Chergui, *Structural Determination of a Short-Lived Excited Iron(II) Complex by Picosecond X-Ray Absorption Spectroscopy,* Phys. Rev. Lett. **98**, 057401 (2007).

[227] C. Bressler, C. Milne, V. T. Pham, A. ElNahhas, R. M. van der Veen, W. Gawelda, S. Johnson, P. Beaud, D. Grolimund, M. Kaiser, C. N. Borca, G. Ingold, R. Abela, and M. Chergui, *Femtosecond XANES Study of the Light-Induced Spin Crossover Dynamics in an Iron(II) Complex,* Science **323**, 489 (2009).

[228] A. L. Smeigh, M. Creelman, R. A. Mathies, and J. K. McCusker, *Femtosecond Time-Resolved Optical and Raman Spectroscopy of Photoinduced Spin Crossover: Temporal Resolution of Low-to-High Spin Optical Switching,* J. Am. Chem. Soc. **130**, 14105 (2008).

[229] N. Huse, T. K. Kim, L. Jamula, J. K. McCusker, F. M. F. de Groot, and R. W. Schoenlein, *Photo-Induced Spin-State Conversion in Solvated Transition Metal Complexes Probed via Time-Resolved Soft X-ray Spectroscopy,* J. Am. Chem. Soc. **132**, 6809 (2010).

[230] Z. S. Yoon, Y.-T. Chan, S. Li, G. R. Newkome, and T. Goodson, *Ultrafast Time-Resolved Spectroscopy of Self-Assembled Cyclic Fe(II)−Bisterpyridine Complexes,* J. Phys. Chem. B **114**, 11731 (2010).

[231] J. Tribollet, G. Galle, G. Jonusauskas, D. Deldicque, M. Tondusson, J. F. Letard, and E. Freysz, *Transient absorption spectroscopy of the iron(II) $[Fe(phen)_3]^{2+}$ complex: Study of the non-radiative relaxation of an isolated iron(II) complex,* Chem. Phys. Lett. **513**, 42 (2011).

[232] N. Huse, H. Cho, K. Hong, L. Jamula, F. M. F. de Groot, T. K. Kim, J. K. McCusker, and R. W. Schoenlein, *Femtosecond Soft X-ray Spectroscopy of Solvated Transition-Metal Complexes: Deciphering the Interplay of Electronic and Structural Dynamics,* J. Phys. Chem. Lett. **2**, 880 (2011).

[233] C. Consani, M. Prémont-Schwarz, A. ElNahhas, C. Bressler, F. van Mourik, A. Cannizzo, and M. Chergui, *Vibrational Coherences and Relaxation in the High-Spin State of Aqueous $[Fe^{II}(bpy)_3]^{2+}$,* Angewandte Chemie International Edition **48**, 7184 (2009).

[234] M. van Veenendaal, J. Chang, and A. J. Fedro, *Model of Ultrafast Intersystem Crossing in Photoexcited Transition-Metal Organic Compounds,* Phys. Rev. Lett. **104**, 067401 (2010).

[235] J. Chang, A. J. Fedro, and M. van Veenendaal, *Ultrafast cascading theory of intersystem crossings in transition-metal complexes,* Phys. Rev. B **82**, 075124 (2010).

[236] L. H. Böttger, A. I. Chumakov, C. M. Grunert, P. Gütlich, J. Kusz, H. Paulsen, U. Ponkratz, V. Rusanov, A. X. Trautwein, and J. A. Wolny, *Spin- and phase transition in the spin crossover complex $[Fe(ptz)_6](BF_4)_2$ studied by nuclear inelastic scattering of synchrotron radiation and by DFT calculations,* Chem. Phys. Lett. **429**, 189 (2006).

[237] J. A. Wolny, H. Paulsen, A. X. Trautwein, and V. Schünemann, *Density functional theory calculations and vibrational spectroscopy on iron spin-crossover compounds,* Coordin. Chem. Rev. **253**, 2423 (2009).

[238] A. Vargas, M. Zerara, E. Krausz, A. Hauser, and L. M. Lawson Daku, *Density-Functional Theory Investigation of the Geometric, Energetic, and Optical Properties of the Cobalt(II)tris(2,2'-bipyridine) Complex in the High-Spin and the Jahn−Teller Active Low-Spin States,* J. Chem. Theory Comput. **2**, 1342 (2006).

[239] Y. Shiota, D. Sato, G. Juhász, and K. Yoshizawa, *Theoretical Study of Thermal Spin Transition between the Singlet State and the Quintet State in the $[Fe(2\text{-}picolylamine)_3]^{2+}$ Spin Crossover System,* J. Phys. Chem. A **114**, 5862 (2010).

[240] C. de Graaf and C. Sousa, *Study of the Light-Induced Spin Crossover Process of the $[Fe^{II}(bpy)_3]^{2+}$ Complex,* Chem. Eur. J. **16**, 4550 (2010).

[241] C. de Graaf and C. Sousa, *On the role of the metal-to-ligand charge transfer states in the light-induced spin crossover in $Fe^{II}(bpy)_3$,* Int. J. Quantum Chem. **111**, 3385 (2011).

[242] A. Vargas, A. Hauser, and L. M. Lawson Daku, *Influence of Guest–Host Interactions on the Structural, Energetic, and Mössbauer Spectroscopy Properties of Iron(II)tris(2,2'-bipyridine) in the Low-Spin and High-Spin States: A Density-Functional Theory Study of the Zeolite-Y Embedded Complex,* J. Chem. Theory Comput. **5**, 97 (2009).

[243] L. M. Lawson Daku and A. Hauser, *Ab Initio Molecular Dynamics Study of an Aqueous Solution of $[Fe(bpy)_3](Cl)_2$ in the Low-Spin and in the High-Spin States,* J. Phys. Chem. Lett. **1**, 1830 (2010).

[244] A. Domingo, M. Àngels Carvajal, and C. de Graaf, *Spin crossover in Fe(II) complexes: An ab initio study of ligand σ-donation,* Int. J. Quantum Chem. **110**, 331 (2010).

[245] M. Kepenekian, B. L. Guennic, and V. Robert, *Primary Role of the Electrostatic Contributions in a Rational Growth of Hysteresis Loop in Spin-Crossover Fe(II) Complexes,* J. Am. Chem. Soc. **131**, 11498 (2009).

[246] S. Dick, *Crystal structure of tris(2,2'-bipyridine)iron(II) bis(hexafluorophosphate), $(C_{10}H_8N_2)_3Fe(PF_6)_2$,* Z. Krist.-New Cryst. St. **213**, 356 (1998).

UNIVERSITAT ROVIRA I VIRGILI
THEORETICAL DESCRIPTION OF ELECTRONIC EXCITATIONS IN EXTENDED SYSTEMS:
BEYOND THE STATIC MATERIAL MODEL
Alex Domingo Toro
DL:T. 1705-2011

"Let me tell you the secret that has led me to my goal. My strength lies solely in my tenacity."

— Louis Pasteur

UNIVERSITAT ROVIRA I VIRGILI
THEORETICAL DESCRIPTION OF ELECTRONIC EXCITATIONS IN EXTENDED SYSTEMS:
BEYOND THE STATIC MATERIAL MODEL
Alex Domingo Toro
DL:T. 1705-2011

UNIVERSITAT ROVIRA I VIRGILI